Triggering and W-Polarisation Studies with CMS at the LHC

Jad Marrouche

High Energy Physics
Blackett Laboratory
Imperial College London

A thesis submitted to Imperial College London
for the degree of Doctor of Philosophy
and the Diploma of Imperial College.

Autumn 2010

Abstract

Results from studies on the commissioning of the Global Calorimeter Trigger (GCT) of the CMS experiment are presented. Event-by-event comparisons of the hardware with a bit-level software emulation are used to achieve 100% agreement for all trigger quantities. In addition, a missing energy trigger based on jets is motivated using a simulation study, and consequently implemented and commissioned in the GCT.

Furthermore, a templated-fit method for measuring the polarisation of W bosons at the LHC in the "Helicity Frame" is developed, and validated in simulation. An analysis of the first 3.2 pb^{-1} of $\sqrt{s} = 7$ TeV LHC data in the muon channel yields values of $(f_L - f_R)^+ = 0.347 \pm 0.070$, $f_0^+ = 0.240 \pm 0.176$, and $(f_L - f_R)^- = 0.097 \pm 0.088$, $f_0^- = 0.262 \pm 0.196$ for positive and negative charges respectively. The errors quoted are statistical. A preliminary systematic study is also presented.

Declaration

The work presented in this thesis was carried out between October 2007 and 2010, and is my own work, building on collaborations with members of both the Imperial College and CERN CMS groups. The work of others is explicitly referenced.

Jad Marrouche
October 2010

"Everybody has a plan, until they get punched in the face."

Michael Gerard Tyson

Acknowledgements

The programme of work which occupied my life over the past three years brought many challenges. There were good times, and there were bad times, but I can safely say that it was harder than I had imagined. I got the chance to work on some extremely cool stuff, in an extremely cool place, and so there are a lot of people whom I must thank for getting me through it all. First and foremost my supervisor Costas, for getting me interested in High Energy Physics, and for just being Costas. Greg Iles, for being a friend rather than a colleague, and letting me share his office all this time. Matt Noy and John Jones, for being top rate, helping me when I got stuck, and knowing way too much about way too much! To Anne-Marie, for being a great hostess, Markus Stoye, for coming up with so many good ideas and whom I learnt a great deal from, Alex Tapper, for helping me find my feet on the trigger, and Magnus Hansen for introducing so many bugs that I could write a thesis chapter about fixing them. Many thanks also to Paris Sphicas (who was on the original W discovery paper!), Oliver Buchmueller and Georgia Karapostoli.

I must also thank the Imperial CMS group, in particular Geoff and Jordan, for letting me study here, and the STFC. Thanks also to my fellow students, especially Nikos Rompotis and Alex Sparrow, for being good company all this time, but in particular I must pay gratitude to my family and good friends for all their support these past years.

Thank you and good luck to all!

Contents

List of Figures

List of Tables

Chapter 1

Introduction

1.1 The State of Play

The field of High Energy Physics deals with the search for the answer to two questions. At the most fundamental level,

1. What is everything made of?
2. How does it all interact with each other?

The quest for the answer to (1) is shown historically in Figure 1.1, where a pattern of uncovering a more fundamental basis can be seen. Our current best understanding of the questions posed above is encompassed in a theory called the Standard Model (SM), which is discussed in Section 1.1.1.

1.1.1 The Standard Model

The SM describes two of the three known fundamental forces, namely the electroweak (EWK) and strong interactions. It is a renormalisable quantum field theory based on the $SU(3)_{\text{colour}} \times SU(2)_{\text{isospin}} \times U(1)_{\text{hypercharge}}$ gauge group, that utilises the correspondence between local gauge symmetries of the Lagrangian, $\mathcal{L}_{\text{SM}}$, and

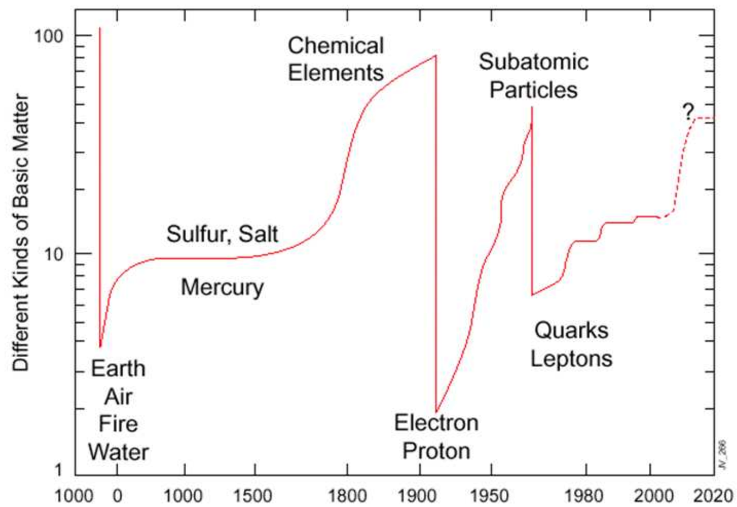

Figure 1.1: A historical overview of our fundamental knowledge of the basic constituents of matter.

conserved charges, to describe natural phenomena. The strong interaction (QCD) part is described by the $SU(3)_{\text{colour}}$ gauge group, and the EWK part is described by the $SU(2)_{\text{isospin}} \times U(1)_{\text{hypercharge}}$ gauge group.

One of the greatest successes of the SM has been the unification of the electromagnetic (EM) and weak-nuclear forces into the current EWK theory, a contribution which led to Salam, Glashow and Weinberg being awarded the Nobel Prize for physics in 1979. Predictions of this theory include the existence of weak neutral currents, discovered in 1973 via neutrino interactions detected with the Gargamelle bubble chamber at CERN [8], and the existence and masses of the weak gauge bosons, found at the Super Proton Synchrotron (SPS) collider in 1983, also at CERN [9, 10].

Whilst the symmetry group describing the strong force is thought to be exact, the EWK symmetry is said to be broken. This is to allow for the theory to describe a massless EM gauge boson and massive weak gauge bosons, without violating local gauge invariance. Such invariance is necessary to allow the introduction of interactions into the theory and to ensure that it is renormalisable, and therefore has predictive power. This is possible through the introduction of local gauge theories with spontaneous symmetry breaking. The simplest mechanism for such symmetry

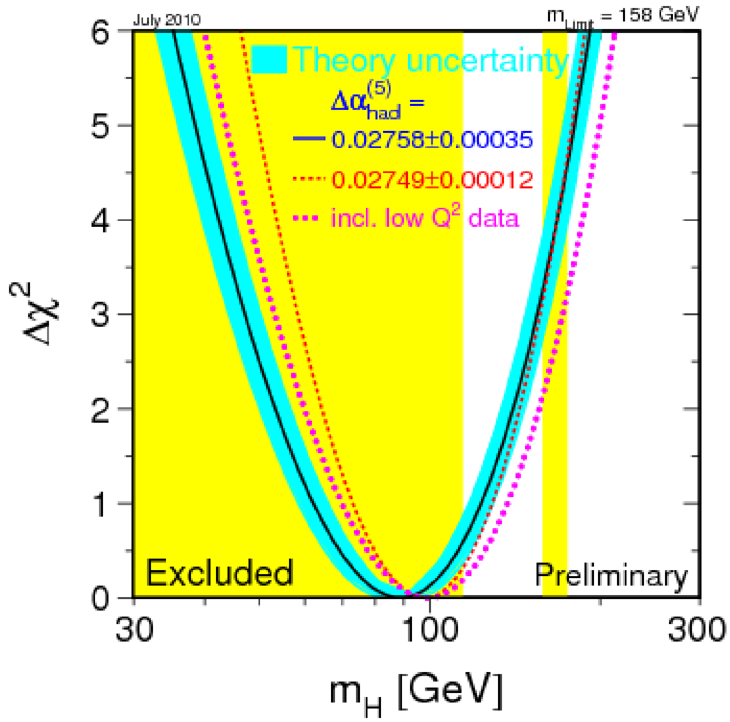

Figure 1.2: The $\Delta\chi^2 = \chi^2 - \chi^2_{\rm min}$ distribution for the Higgs Boson mass fit using all precision EWK data as of July 2010. The mass ranges corresponding to the yellow shaded areas have been excluded from experimental data to a 95% confidence limit.

breaking was developed by Higgs [11] and Guralnik, Hagen and Kibble [12] in 1964. This mechanism however, predicts the existence of a massive scalar particle called the Higgs boson, whose observation represents the final missing piece of the puzzle for the SM as a theory. As of July 2010, the experimental limits on the mass of the Higgs Boson from searches at both the LEP and Tevatron experiments, are shown on the $\Delta\chi^2 = \chi^2 - \chi^2_{\rm min}$ distribution of Figure 1.2 [13]. The distribution assumes that the SM is the correct theory of nature, and combines all precision EWK data to fit for the Higgs Boson mass, M_H. The mass ranges shaded in yellow ($M_H < 114.4$, $158 < M_H < 175$ [GeV]) have been experimentally excluded to a 95% confidence limit.

There are other success stories of the SM. The Glashow-Iliopoulos-Maiani (GIM) mechanism [14] was proposed to explain the suppression of particular kaon decays (flavour/strangeness changing neutral currents), and this hypothesised a fourth quark called the charm quark, which was discovered via the J/Ψ bound state at both SLAC and Brookhaven in 1974 [15, 16]. Kobayashi and Maskawa proposed that CP-violation could be accommodated in the SM if it were extended to three generations (six flavours) [17]. This was duly followed by the discovery of the tau-lepton at SLAC [18] and the bottom and top quarks at Fermilab [19, 20]. The existence of just three generations of matter was determined by the LEP experiments, from an analysis of the decay width of the Z-boson in 1993 [21]. The SM does not predict *per se* the number of generations, but does restrict the number of lepton generations to the number of quark generations, otherwise the Adler (or chiral) anomalies do not cancel out. Over the past 30 years, precision EWK tests of the SM have taken place on different experiments, most recently by the LEP, SLC and Tevatron experiments [22] with a remarkable agreement to theoretical expectations down to the 10^{-18}m scale.

Given the nature of the studies carried out in this thesis, the EWK part of the SM Lagrangian is now reviewed. It may be written as

$$\mathcal{L}_{SU(2)\times U(1)} = \mathcal{L}_{scalar} + \mathcal{L}_{gauge} + \mathcal{L}_{fermion} + \mathcal{L}_{Yukawa}. \tag{1.1}$$

The scalar part of this Lagrangian is given by

$$\mathcal{L}_{scalar} = \left(D^{\mu}\phi\right)\left(D_{\mu}\phi\right)^{\dagger} - V\left(\phi, \phi^{\dagger}\right) \tag{1.2}$$

in which the complex, two-dimensional scalar Higgs field, ϕ, is a doublet under $SU(2)$ and has a $U(1)$ hypercharge of 1. The covariant derivative, D_{μ}, which is required to ensure gauge invariance under local gauge transformations, is defined as

$$D_{\mu} = \partial_{\mu} + ig\frac{\sigma^{i}}{2}W_{\mu}^{i} + ig'\frac{Y}{2}B_{\mu} \tag{1.3}$$

where g and g', W_{μ}^{i} ($i = 1, 2, 3$) and B_{μ} are the $SU(2)$ and $U(1)$ gauge coupling constants and gauge fields respectively, and σ^{i} are the Pauli matrices, which are generators of the $SU(2)$ symmetry group. The potential, $V\left(\phi, \phi^{\dagger}\right)$, is defined as

$$V\left(\phi, \phi^{\dagger}\right) = \mu^{2}\left(\phi\phi^{\dagger}\right) + \lambda\left(\phi\phi^{\dagger}\right)^{2} \tag{1.4}$$

where the form of the equation is dictated by the local $SU(2) \times U(1)$ gauge invariance. In order that the potential remains bound, $\lambda > 0$ is required, but with $\mu^2 < 0$, spontaneous symmetry breaking occurs, leading to a non-zero vacuum potential, and a vacuum expectation value given by $|\phi_0| = \sqrt{\frac{-\mu^2}{2\lambda}}$. This spontaneous symmetry breaking has the result that the ground state does not share the same symmetry as the Lagrangian, and the original symmetry group is broken, $SU(2)_{\text{isospin}} \times U(1)_{\text{hypercharge}} \rightarrow U(1)_{\text{EM}}$, whereby $U(1)_{EM}$ must remain a symmetry of the vacuum to maintain electric charge conservation. The generator of the $U(1)_{\text{EM}}$ group is $Q_{\text{EM}} = I_3 + \frac{Y}{2}$, where Y, the hypercharge, is the generator of the $U(1)_{\text{hypercharge}}$ group, and I_3, the third component of isospin, is one of the $SU(2)$ generators. The value of Y is tuned to give the correct EM charge.

The kinetic terms for the gauge fields are given by

$$\mathcal{L}_{gauge} = -\frac{1}{4}F^i_{\mu\nu}F^{i\mu\nu} - \frac{1}{4}B_{\mu\nu}B^{\mu\nu} \tag{1.5}$$

in which the field strength tensors are defined as

$$B_{\mu\nu} = \partial_\mu B_\nu - \partial_\nu B_\mu \tag{1.6}$$

$$F_{\mu\nu} = \partial_\mu W^i_\nu - \partial_\nu W^i_\mu - g\epsilon_{ijk}W^j_\mu W^k_\nu \tag{1.7}$$

and ϵ_{ijk} is the totally antisymmetric tensor.

The fermion term is given by $\mathcal{L}_{fermion} = \mathcal{L}_{lepton} + \mathcal{L}_{quark}$, with $\mathcal{L}_{lepton}$ given by

$$\mathcal{L}_{lepton} = \sum_{p=1}^{3}\left(\left(\bar{l_p}\right)_L i\gamma^\mu D^\mu_L \left(l_p\right)_L + \left(\bar{e_p}\right)_R i\gamma^\mu D^\mu_R \left(e_p\right)_R\right) \tag{1.8}$$

and $\mathcal{L}_{quark}$ given by

$$\mathcal{L}_{quark} = \sum_{p=1}^{3}\left(\left(\bar{q_p}\right)_L i\gamma^\mu D^\mu_L \left(q_p\right)_L + \left(\bar{u_p}\right)_R i\gamma^\mu D^\mu_R \left(u_p\right)_R + \left(\bar{d_p}\right)_R i\gamma^\mu D^\mu_R \left(d_p\right)_R\right) \tag{1.9}$$

where the index p runs over the three generations, and L and R refer to the chiral projections $\psi_{L(R)} = \frac{1}{2}(1 \mp \gamma_5)\psi$. It is observed that left-handed electrons and neutrinos are mixed by the weak interaction, and therefore $(l_p)_L = \begin{pmatrix} (\nu_p)_L \\ (e_p)_L \end{pmatrix}$ transforms as an $SU(2)$ doublet, whilst $(e_p)_R$ is a right-handed singlet, since there is no evidence for the existence of right-handed neutrinos. Similarly, $(q_p)_L = \begin{pmatrix} (u_p)_L \\ (d_p)_L \end{pmatrix}$ transforms as an $SU(2)$ doublet, whilst $(u_p)_R$ and $(d_p)_R$ as singlets. The differing transformations of these L and R fields leads to the origins of parity violation in the EWK sector. Correspondingly, the covariant derivative for the right-handed singlets is defined as

$$D^R_\mu = \partial_\mu + ig'\frac{Y}{2}B_\mu \tag{1.10}$$

The three generations are in fact not independent, but interact via the CKM (Cabbibo, Kobayashi, Maskawa) mechanism for the quarks, and the PMNS (Pontecorvo, Maki, Nakagawa, Sakata) mechanism for the leptons.

The SM is a chiral gauge theory which means that left and right handed particles are treated differently. The coupling of the fermions to the Higgs field is therefore described by the Yukawa coupling terms, Γ. The Yukawa term for the leptons is given by

$$\mathcal{L}_{Yukawa} = -\Gamma_p \left[\left((\bar{l}_p)_L \phi \right) (e_p)_R + (\bar{e}_p)_R \left(\phi^\dagger (l_p)_L \right) \right] \tag{1.11}$$

with a somewhat similar term for the quarks.

Before any spontaneous symmetry breaking occurs, there are four unbroken generators associated with the fields W^i_μ and B_μ, and four corresponding massless gauge bosons. However, it is known in reality that the photon is massless, but the three weak gauge bosons are massive. The Higgs mechanism can provide mass to these bosons via spontaneous breaking of a local symmetry, without violating the local gauge invariance of the theory. Initially, there are 12 degrees of freedom; four from the complex, two-dimensional scalar Higgs field, ϕ, and two from each of the four massless gauge bosons. Following spontaneous breaking of the $SU(2) \times U(1)$ symmetry, there are three broken generators corresponding to three massless Goldstone bosons [23]. A redefinition of the fields replaces these degrees of freedom by the masses of the gauge bosons, which provides a total of nine degrees of freedom. The field associated with the one remaining unbroken generator (of the $U(1)_{\mathrm{EM}}$ symmetry group) has two degrees of freedom and corresponds to the massless gauge boson, the photon, which remains massless as the group $U(1)_{\mathrm{EM}}$ should remain a symmetry of the vacuum i.e. charge is conserved. This gives a total of 11 degrees of freedom and, since redefinition of the fields cannot change the total number of degrees of freedom, there is one remaining, which corresponds to the Higgs boson, a real scalar field that has not yet been observed experimentally.

1.1.2 Shortcomings of the Standard Model

Much has been made of the Higgs boson. Its discovery has been portrayed as the be-all-and-end-all of particle physics, and yet despite the issue of its existence, there are other, somewhat more serious shortcomings of the SM. For example,

- There is no description whatsoever of gravity in the SM, leading to the belief that the SM is effective up to some energy scale, Λ, past which 'new' physics appears. A natural choice for this scale might be the GUT scale uniting the EWK and strong interactions, $\Lambda \sim 10^{16}$GeV, or the Planck scale where quantum gravity effects become important, $\Lambda \sim 10^{18}$GeV. This leads to problems when calculating the radiative corrections to the SM Higgs boson mass. For example, the one-loop contribution to M_H from a fermion, f, shown in Figure 1.3(a), leads to a positive, quadratically divergent correction to the vacuum expectation value, v, such that $v^2 - v_0^2 \propto \Gamma^2\Lambda^2$, where v_0 is the tree-level value. Since $v \sim 250$GeV and $\Gamma \sim 1$, in order to preserve the scale of the vacuum expectation value after inclusion of these loop corrections, either the SM is only effective up to $\Lambda \sim 1$TeV, or huge cancellations are necessary, $\mathcal{O}(10^{-30})$, something that does not seem very natural. Other contributions to M_H arise from similar interactions with bosons, and self-interactions, such that the overall effect on M_H is given by

  $$M_H^2 = \left(M_H^2\right)_{\text{bare}} + O\left(\lambda, g^2, \Gamma^2\right)\Lambda^2 \tag{1.12}$$

  where $(M_H^2)_{\text{bare}}$ is the tree level Higgs boson mass, and g and Γ are the weak and Yukawa coupling constants respectively. The corrections to M_H are independent of the value of M_H. This issue is called the fine-tuning problem. A related question is the hierarchy problem, which asks why Λ is so much larger than the EWK scale.

- The SM is based on a direct product of three simple groups which all have different coupling constants and it is not a true unification of the strong and EWK forces in this respect. Precision measurements from the LEP, SLC and Tevatron experiments [22] show that the evolution of the coupling constants with energy scale is such that they all fail to meet at a common point, as shown in Figure 1.4 (left), the so-called unification problem.

- At the cosmological level, the notion of the presence of a non-baryonic, non-luminous dark matter - to account for the visible material deficit from expectations by using Newtonian dynamics and General Relativity to describe the observed motions of the galaxies and stars - has been around for some time [24]. Results from e.g. the WMAP Collaboration [25] measure that over 90% of the mass accounting for the observed motions cannot be attributed to such visible material. A particle that is stable, electrically neutral, fairly massive and only very weakly interacting is required. There is no such Dark Matter candidate in the SM.

- Results from the Super Kamiokande experiment [26] have confirmed that differences between the theoretical and observed atmospheric muon neutrino flux are caused by the neutrinos changing flavour, which requires that they have mass, a fact that is not accommodated by the SM *per se*. These results have since been verified by the MINOS experiment [27].

- There is no explanation for the mass spectrum of all observed fermions in the SM. The entire mass range observed spans ~ 14 orders of magnitude as shown in Figure 1.5.

1.1.3 Supersymmetry

A whole host of theories exist with possible solutions to the problems summarised in Section 1.1.2, of which Supersymmetry (SUSY) is a popular example. At its heart lies the introduction of a fermion $\Leftrightarrow$ boson symmetry which protects the Higgs boson mass from divergent corrections, in an attempt to address the fine-tuning problem.

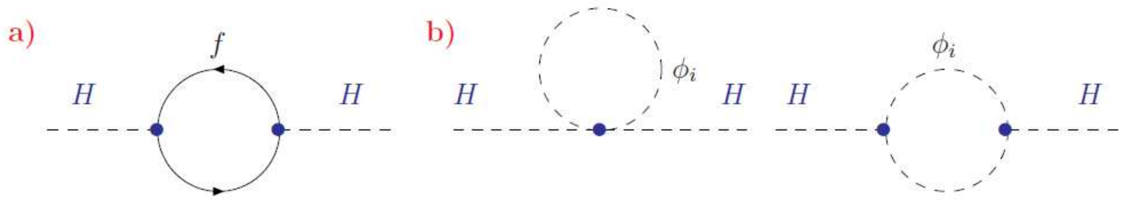

Figure 1.3: Feynman diagrams for the radiative corrections of the Higgs boson mass due to fermions (a) and scalars (b)

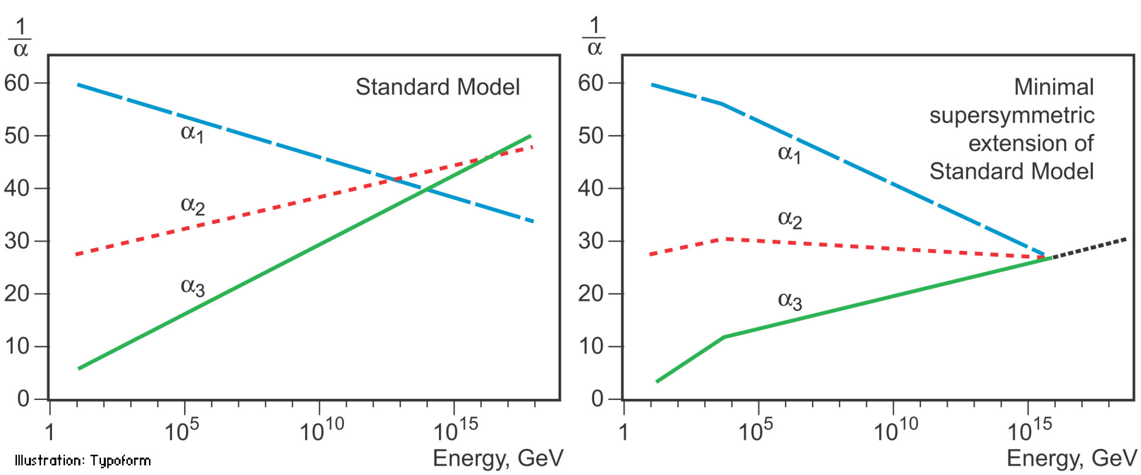

Figure 1.4: Running coupling constants for the EM, weak and strong forces; in the SM (left) the coupling constants do not unify, whereas with the introduction of a SUSY model (right) they do. [1]

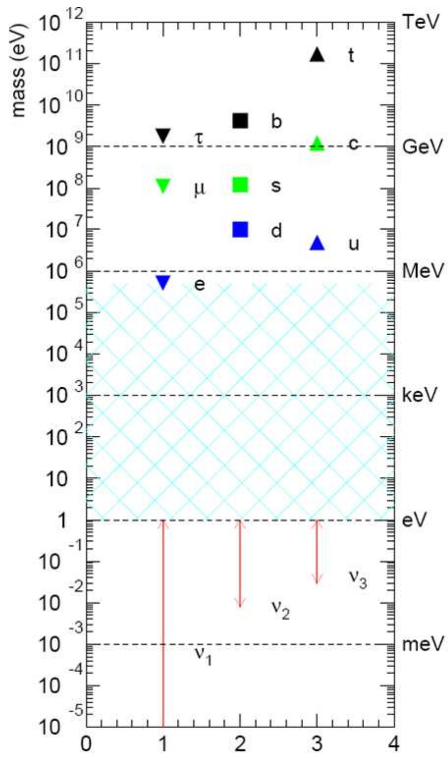

Figure 1.5: The experimentally determined masses of all the fermions in the SM, shown as a function of fermion type. The entire mass range scale spans $\sim$ 14 orders of magnitude.

The diagrams of Figure 1.3(b) show the radiative corrections from introducing a scalar particle, s. By introducing such scalar couplings to the Higgs boson, the effect on M_H is a cancellation of the quadratically divergent terms. The corrections disappear altogether if $m_f = m_s$, however if SUSY were an exact theory, then such SUSY particles should have already been discovered. The extent to which SUSY is 'broken' may be estimated from the radiative correction to M_H in this regime, $M_H^2 - (M_H^2)_{\text{bare}} \propto \left(m_f^2 - m_s^2\right) \log\left(\Lambda/m_s\right)$. In order to keep the correction to the same order as the tree-level value of M_H, the SUSY particles should be seen at around the TeV scale, otherwise the hierarchy and fine-tuning problem are reintroduced. It can be shown from the Coleman-Mandula theorem that the introduction of such a fermion $\Leftrightarrow$ boson symmetry is a unique extension of the Poincaré algebra, whilst preserving its invariance. The above arguments can be extended to the Higgs boson (self coupling) and vector bosons, via the introduction of fermionic partners. Supersymmetry also provides a solution to the unification problem, the coupling constants unifying at a single point, as seen in Figure 1.4(right).

Given this symmetry between fermions and bosons, in order to enforce lepton and baryon number conservation in a simple way, a discrete symmetry called R-parity is imposed. It is defined as $R_p = (-1)^{3B+L+2s}$, where B and L are the baryon and lepton numbers respectively, and s is the particle spin [28]. This quantity is $+1$ for SM particles, and -1 for their SUSY partners. If it is conserved, as it is in the simplest supersymmetric extension to the SM, SUSY particles are always produced in pairs, any decay of a SUSY particle will be into a SUSY particle and a SM particle, and the lightest SUSY particle (LSP) is stable. This LSP is a prime dark matter candidate [29]. Such decay cascades imply that a potential new physics signature will be one with both a large transverse and missing transverse energy component.

Chapter 2

W Bosons at the LHC

2.1 Introduction

The production of the W and Z Vector Bosons from collisions of hadrons probes the nature of QCD and the electroweak interaction. The former predominantly determines the momentum distribution of the boson, whilst the latter, the topological properties of the decay products. A detailed understanding of the properties of W and Z bosons is a prerequisite to numerous searches for physics beyond the Standard Model, e.g. for Supersymmetry, as the experimental signatures of such processes are very similar. This is all the more important since the production of W and Z bosons in proton-proton collisions (i.e. at the LHC) displays new characteristics that are not present in proton-antiproton collisions (i.e. at the SPS and Tevatron colliders). Namely, there is expected to be

1. an asymmetry in the production rate of positive versus negative W bosons,
2. a large transverse polarisation exhibited at high W boson transverse momenta, $P_T(W)$.

The motivation for these effects is discussed in Sections 2.3 and 2.4 respectively. Both of these characteristics can be utilised in distinguishing W and Z events from

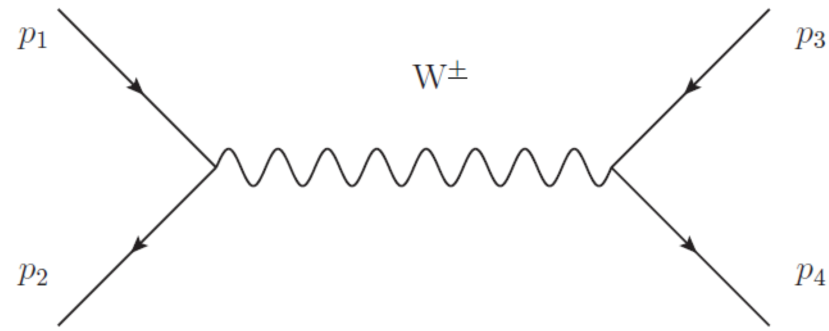

Figure 2.1: The Feynman diagram representing W boson production at tree-level (approximately zero $P_T(W)$), where p_1 and p_2 represent u-type and d-type sea/valence quarks.

other physics processes relevant to high-P_T signatures, e.g. $t\bar{t}$ and new physics. Two examples of this are demonstrated in Chapter 6. It is therefore important to establish these two effects and to measure them as accurately as possible, the latter being studied from Chapter 7 onwards.

2.2 W boson production

The simplest case of W boson production is the one where it is produced with no transverse momentum, apart from the primordial transverse momentum from the incident partons that can otherwise be ignored i.e. $P_T(W) \ll M(W)$. This quark-antiquark annihilation is a Drell-Yan process, and the dominant mechanism by which W bosons are produced at both the LHC and Tevatron experiments. The tree-level Feynman diagram is shown in Figure 2.1, where p_1 and p_2 represent u-type and d-type sea and valence quarks. In this thesis, the leptonic decay channel of the W boson is considered exclusively, i.e. p_3 and p_4 represent a charged lepton and its corresponding neutrino. Given that partons are asymptotically free, the cross-section of the Drell-Yan process may be written as the incoherent sum of the partonic subprocesses:

$$\sigma = \int_0^1 \mathrm{d}x_1 \int_0^1 \mathrm{d}x_2 \; f_1^{P1}(x_1, Q^2) f_2^{P2}(x_2, Q^2) \hat{\sigma}(\hat{s}) \tag{2.1}$$

where $\hat{\sigma}$ is the parton-level cross-section, x_1 and x_2 are the fractions of the proton momenta that are carried by the interacting partons P_1 and P_2 respectively, and Q is

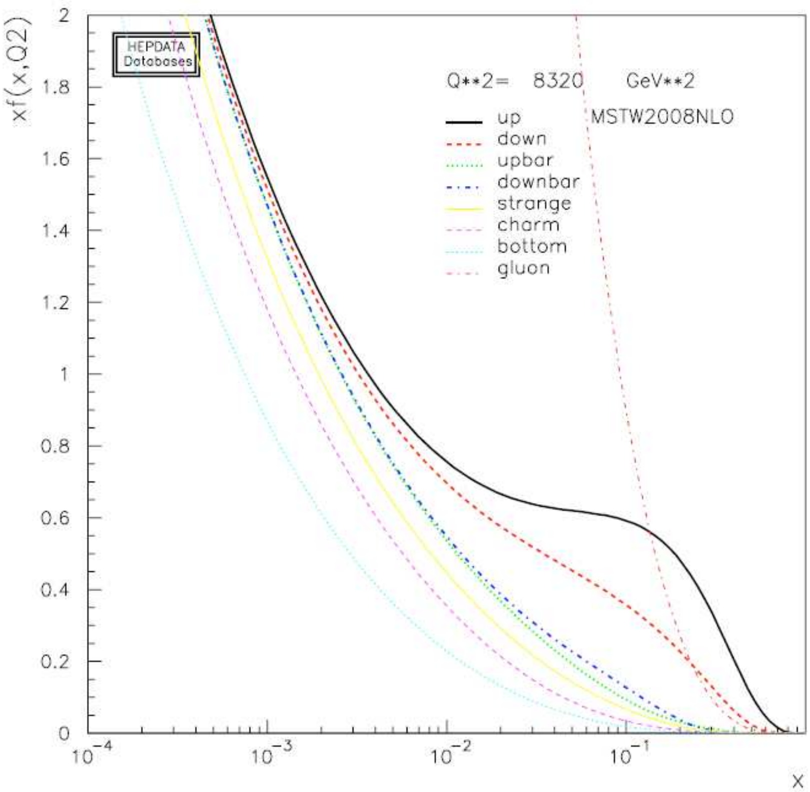

Figure 2.2: The PDFs derived from the MSTW2008NLO set with $Q^2 = M_Z^2$.

the characteristic momentum scale of the hard scattering process, e.g. for the Drell-Yan process $\sigma_{q\bar{q}\to\ell^+\ell^-}$, $\hat{s} = x_1 x_2 s$ and $Q = m_{\ell^+\ell^-}$. The parton-distribution-functions (PDFs), $f_i^{P_j}(x, Q^2)$, express the number density of partons of type i that have a momentum fraction between x and $x + \mathrm{d}x$ of the hadron. Such PDFs are calculated from global fits to data from many experiments, and evolved to the appropriate value of Q^2 via the DGLAP equations [30]. The PDFs from the MSTW2008 set [31] are shown in Figure 2.2 for $Q^2 = M_Z^2$. At this value of Q^2, the number of u and d valence quarks dominate over the $\bar{u}$ and $\bar{d}$ sea quarks over a large range of x, as do the gluons, and the sea quark content is not flavour symmetric.

2.3 Charge Asymmetry

Given the dominant production mechanism for W bosons shown in Figure 2.1, the flavour decomposition of the cross-section, as a function of centre-of-mass energy,

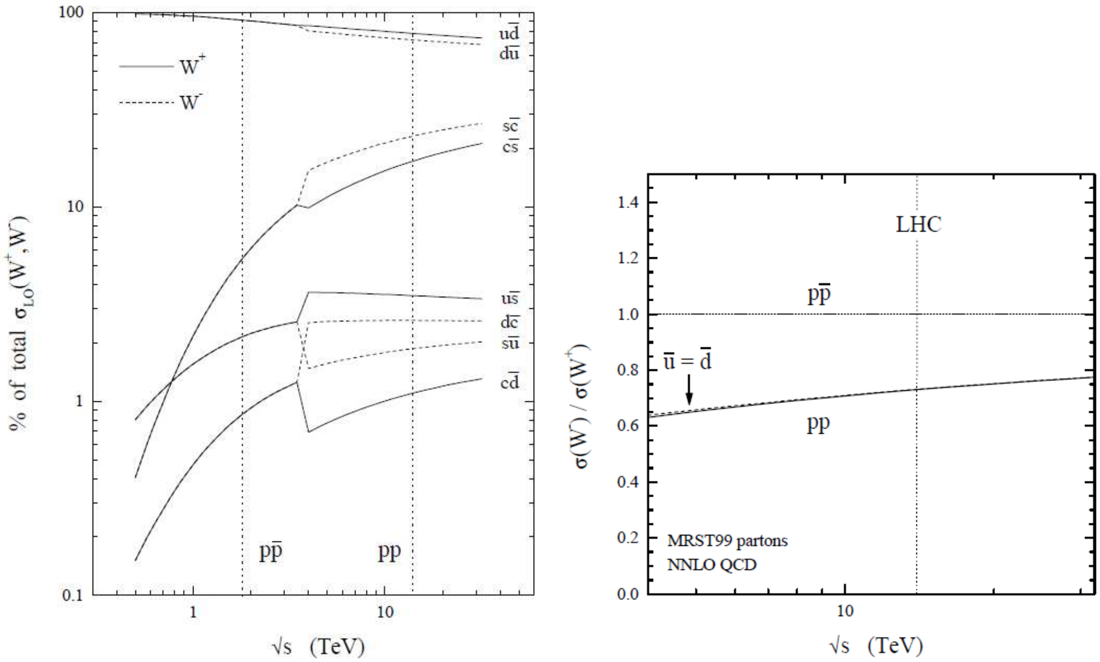

(a) Parton decomposition of the $W^{\pm}$ total cross sections in both $p\bar{p}$ and pp collisions. Individual contributions are shown as a percentage of the total cross section in each case, and the decomposition is the same for both W^+ and W^- bosons in $p\bar{p}$ collisions.

(b) Prediction for the ratio of W^- to W^+ total cross sections in proton-proton collisions, as a function of the collider energy, $\sqrt{s}$. For $p\bar{p}$ collisions the ratio is 1. Also shown (dashed line) is the prediction obtained by setting $\bar{u} = \bar{d}$ in the quark sea.

Figure 2.3: The $W^{\pm}$ parton decomposition (a) and W^+ vs. W^- production ratio (b) at leading order as a function of centre-of-mass energy.

is shown in Figure 2.3(a) [32] (at $\sqrt{s} = 4$ TeV, there is a transition from proton-antiproton to proton-proton collisions). The two dashed lines from left to right represent the centre-of-mass energy of the Tevatron and LHC experiments respectively. Due to the quark-antiquark symmetry of the $p\bar{p}$ environment, there is no difference between the W^+ and W^- fractional contributions. For pp collisions however, this is not the case.

Given Figure 2.3(a), to a good approximation i.e. ignoring the charm and strange quark contributions, the ratio of W^- to W^+ production is given by

$$R_{\mp} \approx \frac{d\bar{u}}{u\bar{d}} = \frac{d}{u} \cdot \frac{\bar{u}}{\bar{d}} \tag{2.2}$$

where the asymmetry stems directly from the valence quark content in the LHC environment. Based on such PDF arguments, approximately 40% more W^+ than

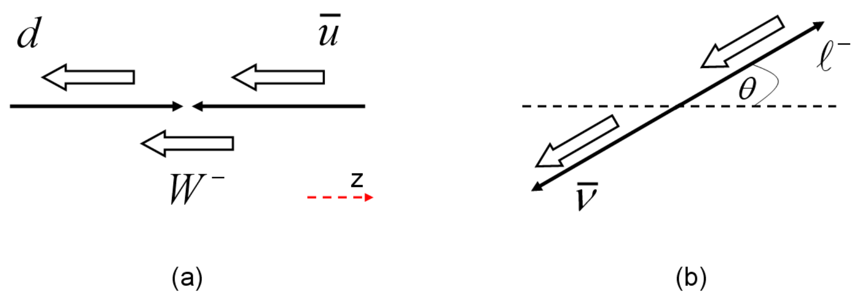

Figure 2.4: The helicity configurations for the initial state (a) and final state (b) of the process $u\bar{d} \to W^- \to \ell^- \bar{\nu}_\ell$. The block arrows represent the spin of the respective particles.

W^- are expected at $\sqrt{s} = 14$ TeV. The evolution of this ratio as a function of centre-of-mass energy is shown in Figure 2.3(b) [32]. This ratio also depends on the $P_T(W)$ range considered, and is discussed further in Chapter 6.

2.4 Polarisation

The spin-1 nature of the vector bosons lead to polarisation effects which predominantly dictate the angular distribution of the decay leptons. For the tree-level diagram in Figure 2.1, the W boson is produced at approximately zero $P_T(W)$ and, in the limit where the quark masses may be neglected such that chirality is equivalent to helicity, is 100% polarised along the beam axis. This is because of the $V - A$ nature of the weak interaction (discussed in more detail in Section 2.4.2), and the fact that the incident quarks are essentially collinear with the beam axis. For valence quark production e.g. in the $p\bar{p}$ environment of the SPS and Tevatron colliders, the angular distribution of the $W^\pm$ decay leptons follow the Drell-Yan distribution, $(1 \mp \cos\theta)^2$, where θ is the angle between the proton (antiproton) and the positively charged (negatively charged) decay lepton in the boson rest-frame, and was first measured by the UA1 experiment [33]. The helicity configurations are shown in Figure 2.4. Since the W boson only couples to left-handed fermions and right-handed anti-fermions, angular momentum conservation dictates that the lepton (anti-lepton) is produced preferentially in the direction of the quark (anti-quark). This leads to a dilution of the forward-backward asymmetry that arises

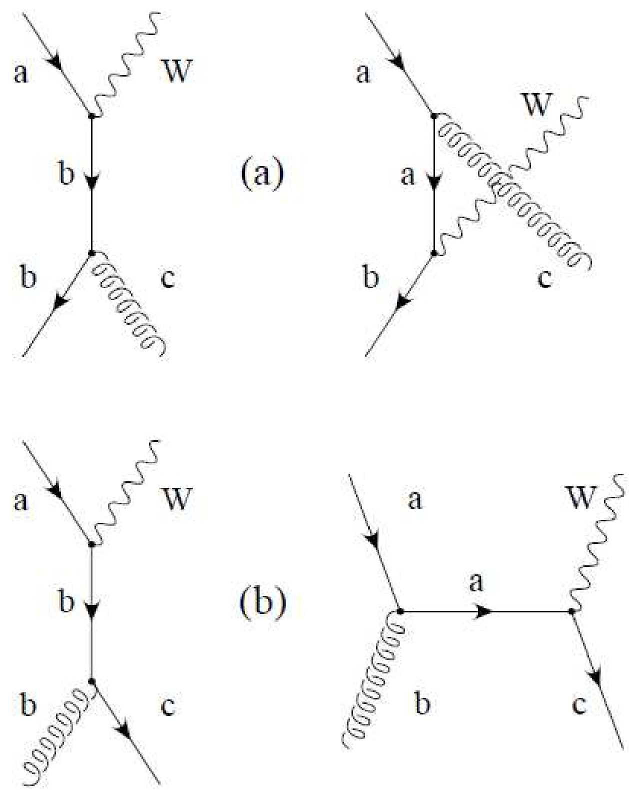

Figure 2.5: The tree-level Feynman diagrams for $W + 1$ jet production, where a and b represent u-type and d-type sea/valence quarks, and c represents an outgoing quark or gluon which produces a jet: (a) quark-antiquark annihilation, (b) quark-gluon Compton diagram

from the PDF arguments in Section 2.2, namely that the W^+ (W^-) is produced preferentially in the direction of the proton (anti-proton).

Whilst similar arguments hold at the LHC, other effects arise when $P_T(W) > 0$, e.g. when the W boson is produced in association with a jet of hadrons. In this case, the production mechanisms also involve quark-gluon interactions. These are relatively suppressed with $p\bar{p}$ collisions, but not with pp collisions, as seen from the PDF arguments of Section 2.2. The Feynman tree-level $W + 1$ jet diagrams for the quark-antiquark annihilation, and quark-gluon Compton processes are shown in Figures 2.5(a) and 2.5(b) respectively.

2.4.1 Theoretical expectations for high $P_T(W)$

Each of the different production mechanisms yield different helicity amplitudes for the W boson. To simplify the arguments that follow, representations of the three initial state processes (quark-gluon, quark-antiquark and gluon-antiquark) in the one jet case for the W^+ boson are shown in Figure 2.6. The diagrams (a), (b) and (c) differ from (d), (e) and (f) solely by the gluon helicity.

The dominant production mechanism at the LHC for W bosons with large $P_T(W)$, which is the phase-space that is most interesting for new physics searches, is the quark-gluon initial state. This can be deduced from the following arguments:

- Production of bosons with a large P_T involves valence quarks,
- There are no valence anti-quarks in the LHC environment,
- For values of $x_{\text{bjorken}} > 0.1$, the probability of finding a gluon in the proton is greater than that for an anti-quark (see Figure 2.2).

Given this production mechanism, the square of the amplitudes at tree level for cases (a) and (d) are proportional to [34]:

$$(a) : \frac{(d,\nu)^2}{(u,g)(g,d)(\nu,e^+)}$$

$$(d) : \frac{(u,e^+)^2}{(u,g)(g,d)(\nu,e^+)}$$

where (d,ν) represents the dot product between the four-vectors of the d quark and neutrino etc. For process (a), the d quark-neutrino direction defines the polarisation axis, and (d,ν) is maximal when the d quark and neutrino are back-to-back. Given that the W^+ boson is produced in the opposite direction to the d quark, this leads to an enhancement of the left-handed helicity, f_L, of the W^+ boson i.e. the (left-handed) neutrino carries away most of the momentum from the W^+ decay. Also, since the d quark is generally in the transverse plane, this leads to polarisation effects in the transverse plane.

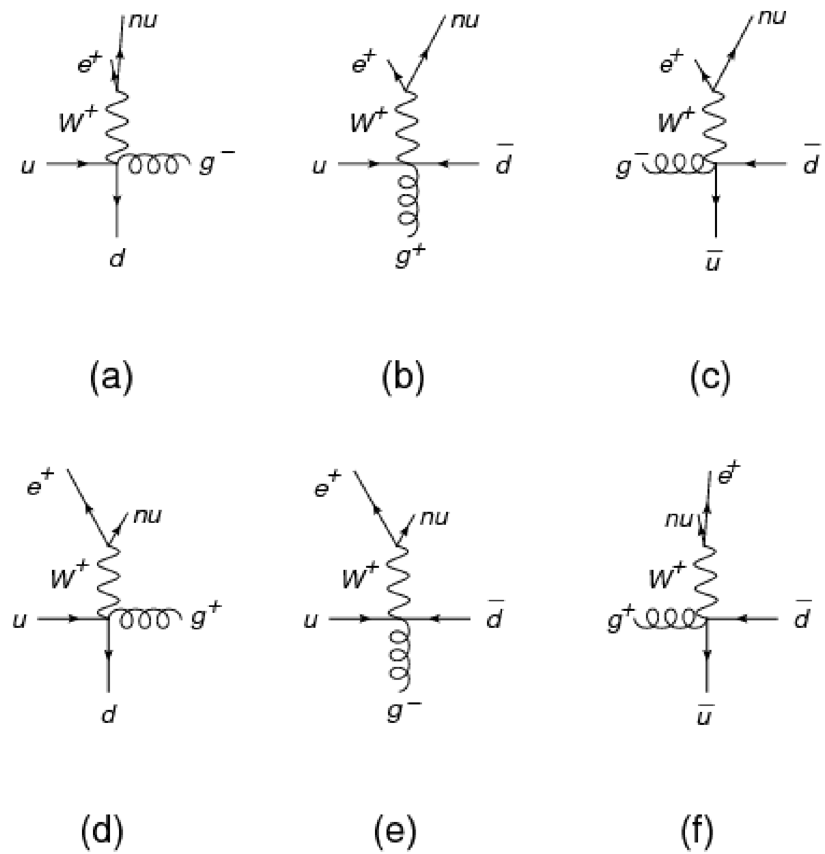

Figure 2.6: Representations of the different W+1 jet helicity amplitudes for the W^+ boson production mechanisms. The superscript on the gluon represents its helicity.

Table 2.1: Z boson couplings to the different fermions.

	c_L	c_R	$\left(\frac{c_L^2}{c_R^2}\right)$
ν	$\frac{1}{2}$	0	-
$\ell^{\pm}$	$\pm\frac{1}{2} \mp \sin^2(\theta_W)$	$\mp\sin^2(\theta_W)$	1.36
$q_1(+\frac{2}{3})$	$\frac{1}{2} - \frac{2}{3}\sin^2(\theta_W)$	$-\frac{2}{3}\sin^2(\theta_W)$	5.05
$q_2(-\frac{1}{3})$	$-\frac{1}{2} + \frac{1}{3}\sin^2(\theta_W)$	$\frac{1}{3}\sin^2(\theta_W)$	30.2

A similar analysis of amplitude (d) leads to a left-handed helicity of the W^+ boson along the incoming u quark direction, which is generally aligned with the beam z-axis. Since the boson flight direction and the beam axis are not aligned in general, this production process does not lead to a fixed helicity for the W^+ boson, unless large rapidities are considered. Nevertheless, both these amplitudes lead to non-trivial helicity effects in the transverse plane, which can be measured, and are expected to show a predominant left-handed behaviour.

The equivalent diagrams for the W^- boson require replacing the incoming left-handed u quark by a d quark and vice versa. Whilst this flips the charge, the helicity is unaffected and the arguments above remain valid. This is another key difference with respect to proton-antiproton collisions.

Whilst the W boson couples with equal strength to all leptons, but always only to left-handed fermions and right-handed anti-fermions, the Z boson couples to both left and right-handed fermions with different relative strengths. However, the arguments above generally also hold true for the Z boson, as the left-handed fermion coupling, c_L, is dominant over the right-handed fermion coupling, c_R. In fact, $c_R = -Q\sin^2(\theta_W)$ and $c_L = I_3 - Q\sin^2(\theta_W)$, where Q is measured in units of e, I_3 is the third component of isospin, and θ_W is the weak mixing angle. Table 2.1 summarises the Z boson couplings to the different fermions.

2.4.2 Quantifying polarisation

Measurements of the polarisation of vector bosons are generally performed in the boson rest frame, along a defined polarisation axis, by studying the distributions

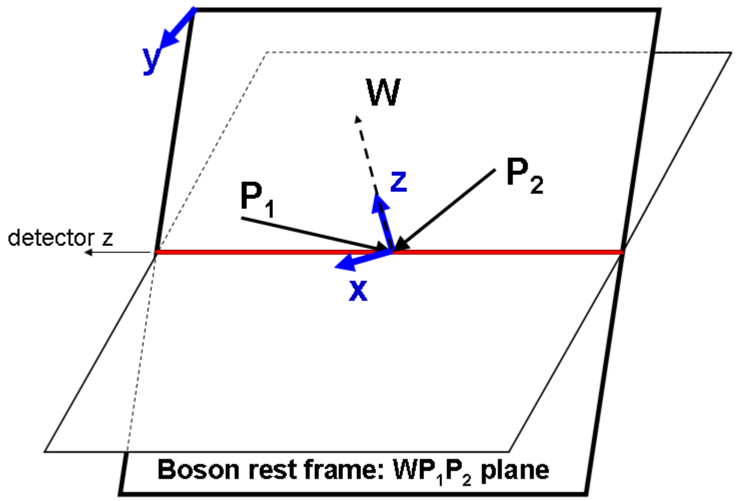

Figure 2.7: The helicity frame, where the polarisation axis is defined as the flight direction of the boson. The angle between this axis and the charged decay lepton direction in the boson rest frame is defined as θ^*.

of the decay leptons. There are two natural choices for such an axis, namely the boson flight direction in the laboratory frame, and the beam line. The boson flight direction is considered exclusively in this thesis, mainly as it aids in the desire to utilise polarisation effects in the transverse plane in New Physics searches. In this so called "helicity frame", the polarisation axis (i.e. z-axis) is defined along the direction of flight of the boson. The x-axis is chosen to lie in the plane spanned by the two protons in the boson rest frame. The resulting two-fold ambiguity over the x-axis direction is solved by asking that the angle between it and the closest proton is minimised. By definition, the y-axis is perpendicular to this plane. This is shown pictorially in Figure 2.7. The same plane spans the W boson in the laboratory frame, as can be seen from the 3×3 determinant of the three-vectors of the W flight direction, and the two protons in the W rest frame, which evaluates to zero.

The differential cross-section can therefore be written as a function of both the polar (θ^*) and azimuthal (ϕ^*) angles of the boson decay leptons in this coordinate system, where the $*$ signifies a measurement in the helicity frame. Physically, a measurement of $0 < |\phi^*| < \frac{\pi}{2}$ means that the lepton will have a larger rapidity than the boson in the laboratory frame (i.e. a smaller P_T), whilst a measurement of $\frac{\pi}{2} < |\phi^*| < \pi$ means that the lepton will have a smaller rapidity than the boson in the laboratory frame (i.e. a larger P_T). The shapes of the transverse momentum and rapidity

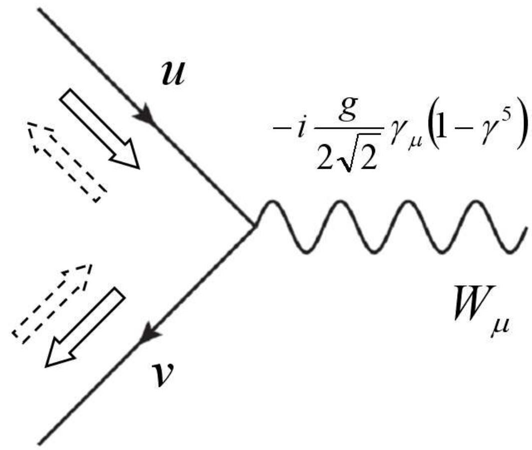

Figure 2.8: The vertex of an incoming fermion u, with a W boson, and an outgoing fermion v. The block arrows represent the spin of the respective particles.

distributions of the decay leptons are governed by the $V - A$ nature of the weak interaction and rotational covariance. By integrating over ϕ^*, the parameterisation of the differential cross section may be written as a function of just θ^*. This is derived in the following discussion, making no assumption about the production mechanism, but instead studying the W boson decay vertex.

In the massless i.e. relativistic limit, chirality is equivalent to helicity. The vertex of an incoming fermion u with a vector particle and an outgoing fermion v, may be written as $\bar{u}\gamma^\mu v$, where $\bar{u} = u^\dagger\gamma^0$ (see Figure 2.8). Writing:

$$u = u_L + u_R = \tfrac{1}{2}(1-\gamma^5)u + \tfrac{1}{2}(1+\gamma^5)u \tag{2.3}$$

and

$$\bar{u} = \bar{u}_L + \bar{u}_R = \tfrac{1}{2}\bar{u}(1+\gamma^5) + \tfrac{1}{2}\bar{u}(1-\gamma^5) \tag{2.4}$$

where γ^5 is the Hermitian chirality operator, this may be re-expressed as $\bar{u}_L\gamma^\mu v_L + \bar{u}_L\gamma^\mu v_R + \bar{u}_R\gamma^\mu v_L + \bar{u}_R\gamma^\mu v_R$. Using the anti-commutation relation $\{\gamma^5, \gamma^\mu\} = 0$ along with the fact that $(\gamma^5)^2 = 1$, the terms $\bar{u}_L\gamma^\mu v_R$ and $\bar{u}_R\gamma^\mu v_L$ evaluate to zero, and hence helicity is conserved at such a vertex i.e. it cannot "flip". This holds equally true at the axial-vector vertex $\bar{u}\gamma^5\gamma^\mu v$, and thus overall for the W boson. This means that writing the angular momentum states in the form $\mid J, M\rangle$:

$$\mid \tfrac{1}{2}, \pm\tfrac{1}{2}\rangle \oplus \mid \tfrac{1}{2}, \pm\tfrac{1}{2}\rangle = \mid 1, 1\rangle \text{ or } \mid 1, -1\rangle \text{ but not } \mid 1, 0\rangle \text{ or } \mid 0, 0\rangle \tag{2.5}$$

For the W boson, the $V - A$ nature of the weak interaction means that there is a one-to-one correspondence between charge and observed helicity state i.e. $\mid 1, +1\rangle$ is associated with the W^+, whilst $\mid 1, -1\rangle$ is associated with the W^-. Expressed more formally, the W boson only couples to left-handed fermions (i.e. the right-handed fermion coupling, $c_R(f) = 0$), and right-handed anti-fermions.

Rotating these states by θ^* expresses the observed angular distribution of the charged decay lepton (in the W rest-frame) in terms of helicity states for the boson (see Figure 2.4(b), where the dashed line represents the W boson flight direction in this case). The general form for such rotations is given by:

$$\mid J, M\rangle = \sum_{M'=-J}^{+J} d^J_{M,M'} \mid J, M'\rangle \tag{2.6}$$

where $d^J_{M,M'}$ are the components of the Wigner d-matrices, and $d^J_{M,M'} = (-1)^{M'-M} d^J_{M',M}$. Note that $M' = -1, 0, +1$ represent left-handed, longitudinal and right-handed polarised boson states respectively. Squaring the amplitudes leads to the following parameterisation of the W boson cross-section:

$$\sigma(\theta^*_{\ell+}) \sim f_L \frac{(1 - cos(\theta^*_{\ell+}))^2}{4} + f_0 \frac{sin^2(\theta^*_{\ell+})}{2} + f_R \frac{(1 + cos(\theta^*_{\ell+}))^2}{4} \tag{2.7}$$

$$\sigma(\theta^*_{\ell-}) \sim f_L \frac{(1 + cos(\theta^*_{\ell-}))^2}{4} + f_0 \frac{sin^2(\theta^*_{\ell-})}{2} + f_R \frac{(1 - cos(\theta^*_{\ell-}))^2}{4} \tag{2.8}$$

where the three parameters f_L, f_0, f_R determine the corresponding amount of left-handed, longitudinal, and right-handed helicity respectively, and $f_i > 0$, $(f_L + f_0 + f_R) = 1$ by definition. The f_i coefficients are in general a function of both the boson P_T and rapidity (see Chapter 6 for more information). Expectations from theoretical calculations for the evolution of these f_i parameters in the helicity frame as a function of $P_T(W^\pm)$ at $\sqrt{s} = 14$ TeV are shown in Figure 2.9 [2]. The calculations are performed for the $W + 2$ jets case, where it is still clear that the W bosons are predominantly left-handed, and this left-handedness increases with $P_T(W)$, supporting the statements made in Section 2.4.1.

The most general form of the differential cross-section derived above (to leading order in QCD) is given by [35]:

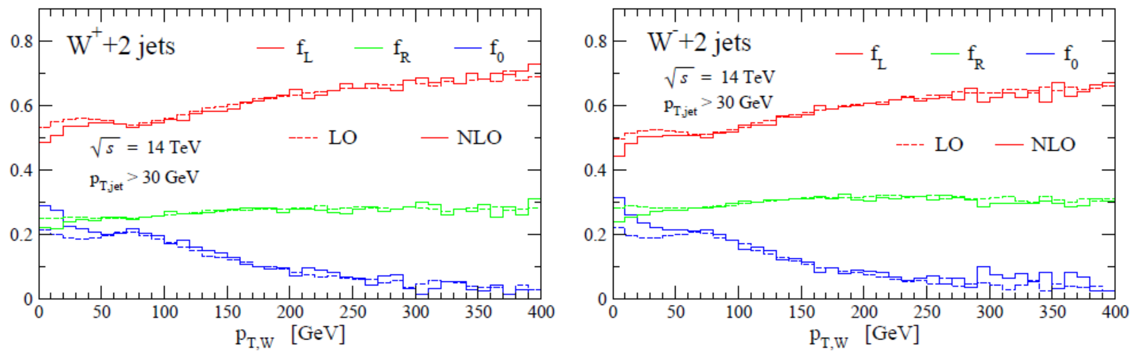

Figure 2.9: The Leading-Order and Next-to-Leading-Order expectations for f_L, f_0 and f_R as a function of $P_T(W^+)$ (left), and $P_T(W^-)$ (right), for the $W+2$ jets case at $\sqrt{s} = 14$ TeV. [2]

$$\begin{aligned}\frac{\mathrm{d}N}{\mathrm{d}\Omega} \sim (1+\cos^2\theta) + \tfrac{1}{2}A_0(1-3\cos^2\theta) + A_1 \sin 2\theta \cos\phi \\ +\tfrac{1}{2}A_2 \sin^2\theta \cos 2\phi + A_3 \sin\theta\cos\phi + A_4\cos\theta\end{aligned} \tag{2.9}$$

where the A_i are the ratios of the helicity cross-sections of the W boson to its total unpolarised cross-section. These coefficients also depend on the W boson charge, transverse momentum, $P_T(W)$, and rapidity, $|Y(W)|$. Integrating Equation (2.9) over the azimuthal angle yields:

$$\frac{\mathrm{d}N}{\mathrm{d}\cos\theta} \sim (1+\cos^2\theta) + \tfrac{1}{2}A_0(1-3\cos^2\theta) + A_4\cos\theta. \tag{2.10}$$

Comparing to Equations (2.7) and (2.8), by grouping together terms in $\cos\theta$ and $\cos^2\theta$, shows the equivalence of A_0 to $(f_L + f_R) \equiv f_0$ and A_4 to $\pm(f_L - f_R)$. These A_i coefficients make-up the elements of the helicity density matrix, of which the f_i coefficients are the diagonal elements. By virtue of defining both a polar and azimuthal angle, the off-diagonal elements of this matrix are probed via the ϕ^* distribution.

Whilst the A_0 and A_4 coefficients allow a study of the W helicity parameters, the other coefficients are useful for studying QCD effects on the production of the W [36], e.g. the A_2 coefficient is not equal to A_0 only if the effects of gluon loops are taken into account. Also, A_3 is only affected by the quark-gluon interaction, and hence can be used to constrain the gluon PDFs. At next-to-leading-order, the coefficients

A_5, A_6 and A_7 appear, which are P-odd and T-odd and may play an important role in direct CP-violation effects in W production and decay [37].

For the Z boson, given that the right-handed coupling to leptons is non-zero, the f_i coefficients above can no longer be interpreted as boson helicity components. Rather, the general relationship between boson handedness V_i, and the f_i is given by:

$$\begin{pmatrix} V_L \\ V_R \\ V_0 \end{pmatrix} = \frac{c_L^2 + c_R^2}{c_L^4 - c_R^4} \begin{pmatrix} c_L^2 & -c_R^2 & 0 \\ -c_R^2 & c_L^2 & 0 \\ 0 & 0 & \frac{c_L^4 - c_R^4}{c_L^2 + c_R^2} \end{pmatrix} \begin{pmatrix} f_L \\ f_R \\ f_0 \end{pmatrix} \tag{2.11}$$

No new information is obtained by studying both charged leptons in the Z case. The parameterisation of Equation 2.9 is the same for Z bosons, although the values of the coefficients will be different in general.

Chapter 3

The Large Hadron Collider

3.1 Introduction

Straddling the Franco-Swiss border, between 45 and 170 metres underground, the Large Hadron Collider [38] (LHC) is a two-ring circular synchrotron with a circumference of 26.7 km, housed in the existing tunnel constructed for the Large Electron Positron (LEP) experiment. It has been designed to collide beams of protons at a centre of mass energy $\sqrt{s}$ = 14 TeV, and up to a luminosity of 10^{34} particles $\text{cm}^{-2}\text{s}^{-2}$. In a separate mode, the LHC can also accelerate lead and gold ions to 2.7 TeV per nucleon in a bid to study quark-gluon plasmas.

As motivated from Sections 1.1.2 and 1.1.3, the LHC is a discovery machine whose primary objectives are to discover the Higgs boson and look for physics beyond the SM, such as evidence of the particles predicted by supersymmetric theories. The LHC will also enhance our understanding of known particles, and known effects such as CP-violation. This motivates the extremely large collision energy and luminosity, in an attempt to probe the extremely small cross-sections for such 'new' processes when compared to known processes. An illustration of the production cross-section (in the proton-proton environment) of different physics processes as a function of centre of mass energy is shown in Figure 3.1. The Higgs production cross-section is between nine and eleven orders of magnitude smaller than the total inelastic proton-proton cross-section, depending on the Higgs boson mass.

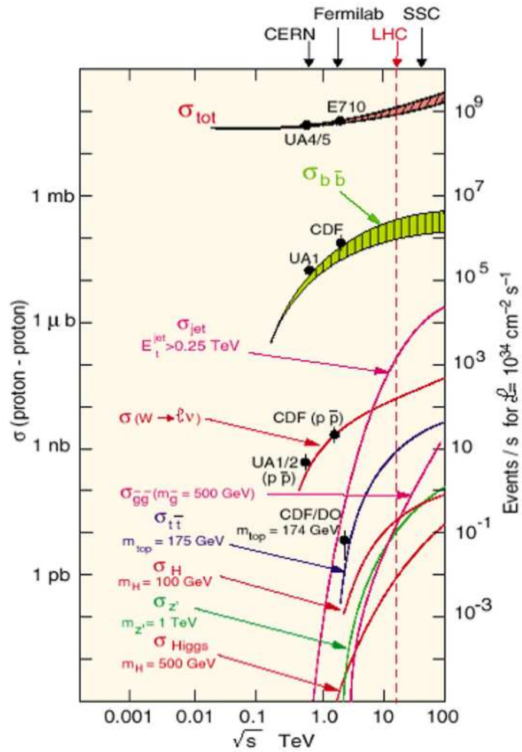

Figure 3.1: The production cross-sections of various physics processes in a proton-proton environment, as a function of centre of mass energy.

The two counter-rotating proton beams are arranged in bunches, which are approximately cylindrical and orbit at a rate of 40 MHz in the LHC. To illustrate the steps required to achieve this, the CERN accelerator complex is shown in Figure 3.2. The beam begins as hydrogen gas that is ionised and fed into the linear accelerator LINAC2. There, it is accelerated to 50 MeV per proton before being injected into the Proton Synchrotron Booster (PSB), which takes this energy up to 1.4 GeV. The Proton Synchrotron (PS) and Super Proton Synchrotron (SPS) accelerators take this energy up to 25 GeV and 450 GeV respectively, before the beam is injected into the LHC via the transfer lines TI2 and TI8, at which point it is accelerated up to the design energy of 7 TeV. The focusing and bending of the beams in the LHC is performed using an array of superconducting dipole and quadrupole magnets, along with a large number of beam correcting magnets (triplets, multipoles etc).

The bunch structure used to fill the LHC ring is shown in Figure 3.3. The PS produces a batch of 72 bunches, and three/four of these batches are then injected into the SPS, before arriving at the LHC. This procedure is repeated 12 times. In

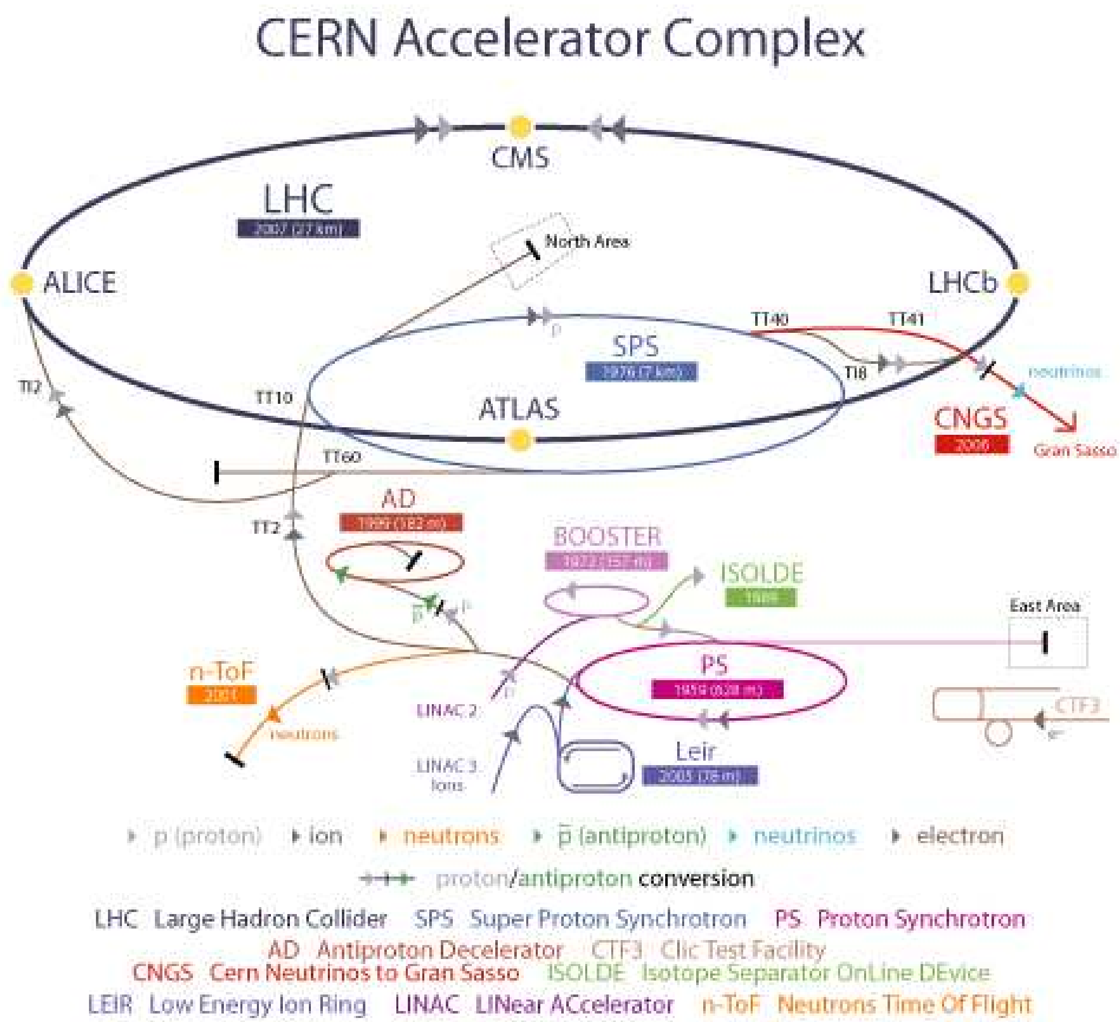

Figure 3.2: The CERN accelerator complex.

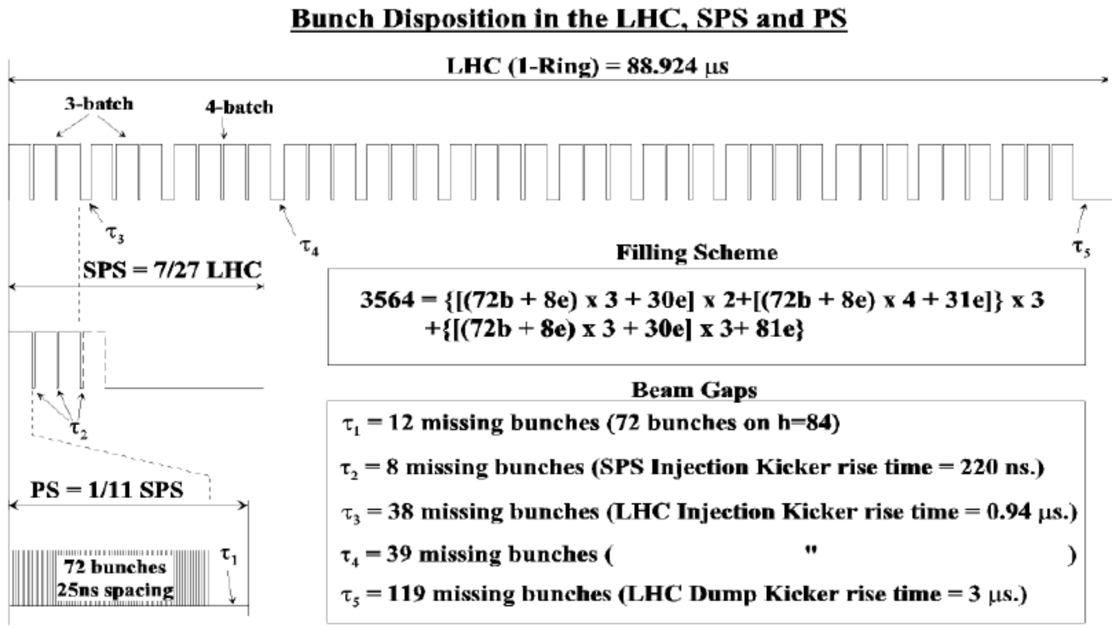

Figure 3.3: The bunch structure used to fill the LHC ring.

total, each orbit contains 3564 of these bunch slots, of which 2808 are filled with $\mathcal{O}(10^{11})$ protons per bunch. At the maximum luminosity of $\mathcal{L} = 10^{34}$ cm^{-2}s^{-1}, there are on average 22 events per bunch crossing.

There are four main experiments at the LHC; LHCb (Large Hadron Collider Beauty experiment) and ALICE (A Large Ion Collider Experiment) are studying b-physics and heavy ion physics respectively, whereas ATLAS (A Toroidal LHC Apparatus) and the CMS (Compact Muon Solenoid) are general purpose detectors aiming to discover new physics at the TeV energy scale.

In September 2008, the LHC was on track for first collisions at a centre of mass energy of 14 TeV. However, a faulty interconnection between two LHC dipole magnets failed during a magnet quench and the resulting release of stored energy resulted in a catastrophic helium leak, $\mathcal{O}$(5tonnes). This caused major damage to the machine, and it was not until November 2009, following an extensive period of recuperation, that beams were circulating in the LHC once again. The decision was taken however to operate at half the design centre of mass energy, i.e. $\sqrt{s} = 7$ TeV, and the first collisions at this energy took place in March 2010.

3.2 The Compact Muon Solenoid Detector

The CMS detector, illustrated in Figure 3.5, is composed of (moving radially outwards) a pixel tracker, a silicon strip tracker, an active lead tungstate electromagnetic calorimeter (ECAL), a sampling brass-plastic hadronic calorimeter (HCAL), a four Tesla superconducting solenoid magnet, an outer HCAL (to detect punch-through events), and four muon chambers interleaved with the iron return yokes. Its design is based around very high quality lepton and photon reconstruction, motivated in part by the SUSY decay cascades, but mainly by the decay modes of the SM Higgs boson, as shown in Figure 3.4 e.g. $H \to \gamma\gamma$ which has a very clean signature. This requires a high performance ECAL, in order to distinguish such photons from background modes such as $\pi^0 \to \gamma\gamma$.

The 4T magnetic field is required to induce sufficient bending of the charged particles' trajectories in the transverse plane, so that both their charge and momenta can be measured, up to the highest energy particles expected at the LHC. The high precision tracking is also of great benefit in reconstructing vertices which is essential in the presence of both in-time pileup (on average 22 events per crossing) and out-of-time pileup (particles of lower momenta spiralling close to the centre of the detector in the magnetic field), as well as reconstructing displaced vertices from e.g. c and b-quark decays. Besides the outer HCAL, the calorimeters are positioned inside the magnetic coil to eliminate energy losses due to interactions with the magnet system, and this places restrictions on the overall size of the calorimeters.

The coordinate system used is defined such that the z-axis points along the direction of the beam pipe, the y-axis points vertically upwards, and the x-axis points radially towards the centre of the LHC ring, with the origin defined at the interaction point of the two proton beams. The azimuthal angle ϕ is measured from the x-axis in the $x-y$ plane, and the polar angle θ is measured from the z-axis, and expressed in terms of the Lorentz invariant quantity pseudo-rapidity $\eta = -\log[\tan(\theta/2)]$. The CMS is designed to be as hermetic as possible, with a total coverage of $|\eta| < 5$ ($|\eta| < 3$ at full detector resolution), in order to account for as many of the particles produced in an event, and hence provide a more accurate determination of the missing transverse energy per event, an important signature of potential physics beyond the SM.

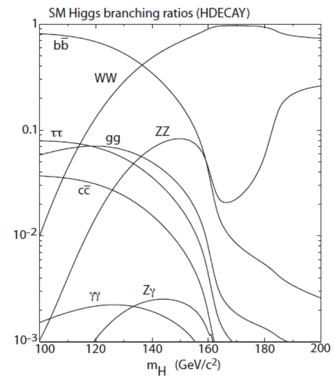

Figure 3.4: The Higgs boson decay modes for $100 < M_H < 200$ GeV

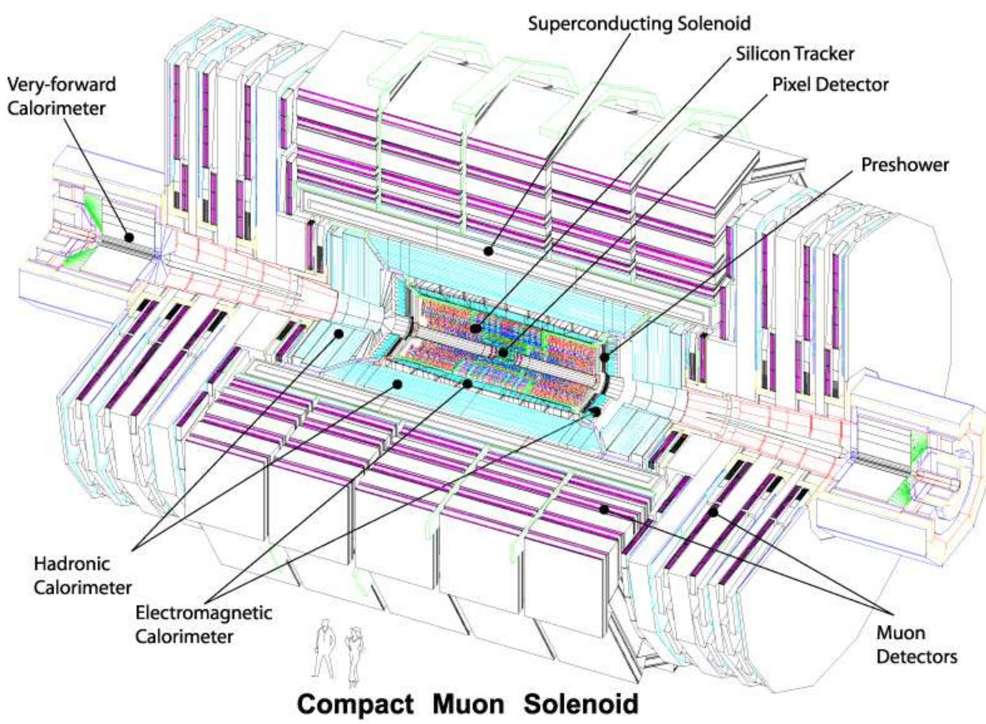

Figure 3.5: An illustration of the CMS detector. [3]

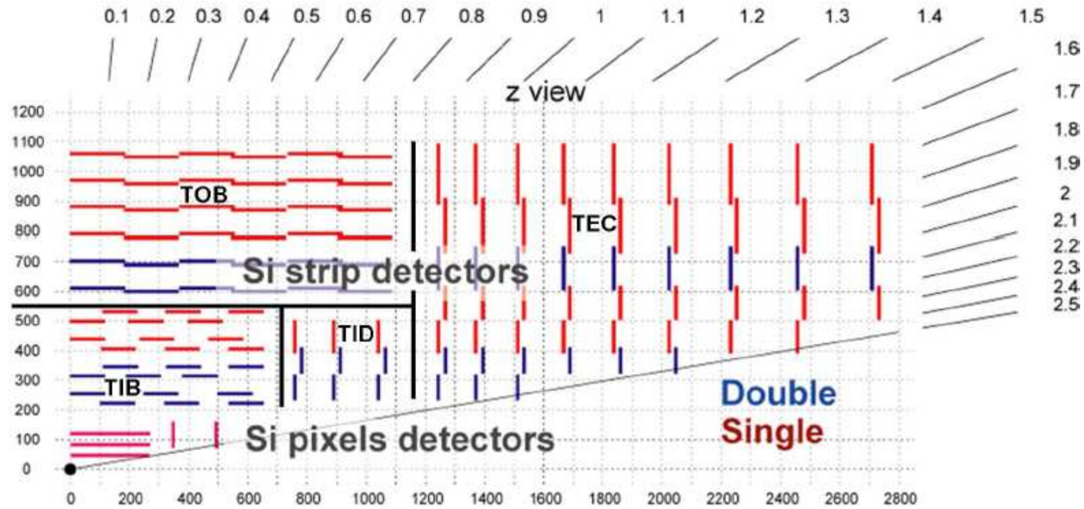

Figure 3.6: The layout of the CMS tracker (a quarter slice in z is shown).

3.2.1 The Tracker

The tracker is designed to record the paths taken by particles passing through it, to allow the momenta of charged particles to be determined from their curvature in the 4T magnetic field, as well as record the positions of any vertices. The tracker is composed of an inner pixel detector, and an outer strip tracker. It is made entirely from silicon, which scintillates as particles pass through it, allowing high resolution measurements to be performed. The tracker covers a pseudorapidity range of $|\eta| < 2.5$. The pixel detector is the closest detector to the beam pipe, at a radius between 4.3 and 10.2cm, and as such experiences the highest particle fluences of any CMS subdetector. There are $\sim 45 \times 10^6$ readout channels, which seed the track reconstruction, and measure to a position resolution of about 10 microns in $r\phi$ and 15-20 microns in z. The silicon strip tracker is made up of several parts, as shown in Figure 3.6: The Tracker Inner Barrel (TIB), Tracker Outer Barrel (TOB), Tracker EndCap (TEC) and the Tracker Inner Discs (TID). In all, there are approximately a further ten million readout channels, the information for which is used for track reconstruction. The TIB has a 230 micron resolution in z, and a 23-34 micron resolution in $r\phi$, whereas the TOB which is further out, has a 530 micron resolution in z, and a 35-52 micron resolution in $r\phi$.

3.2.2 Electromagnetic Calorimeter

The ECAL is designed to measure the energies of electrons and photons, which lose their energy by radiation. It covers a total pseudorapidity range of $|\eta| < 3$, but $|\eta| < 2.5$ for precise measurements. The ECAL is composed of over 75,000 lead tungstate crystals, which scintillate as the particles deposit their energy. The light emitted is then collected and amplified by photodetectors. There are two types of photodetector used in the CMS; silicon avalanche photodiodes in the barrel, and vacuum phototriodes in the endcaps, which have a lower gain but are more radiation tolerant. Lead tungstate is used because of its short radiation length ($X_0 \sim 0.9$ cm), small Molierè radius (~ 2.1 cm) and radiation hardness, as well as its rapid scintillation time, which is important in avoiding pile-up. The crystal dimensions are $22 \times 22 \times 230$ mm ($\sim 26X_0$), and so on average all the energy of an electron or photon can be absorbed, and over 90% of the shower from a photon can be contained within a single crystal.

Using a 100 GeV test beam, the energy resolution of the ECAL was found to be

$$\frac{\sigma(E)}{E} = \frac{2.8\%}{\sqrt{E}} \oplus \frac{124\text{MeV}}{E} \oplus 0.26\% \tag{3.1}$$

which is better than the design value of $\frac{\sigma(E)}{E} < 0.6\%$ at 100 GeV. The ECAL also contains two identical preshower detectors in the endcap region, where the particle fluences are expected to be higher. They are composed of two layers of lead each and their purpose is to initiate showering from electrons, photons and π^0 mesons. This improves the discrimination of hadrons, as well as improving the position measurement of the electrons and photons.

3.2.3 Hadronic Calorimeter

The HCAL is a sampling calorimeter composed of brass absorbers and plastic scintillator tiles, except in the hadron forward region in which steel absorbers and quartz fibre scintillators are used because of their increased radiation tolerance. It is designed to measure the energies of strongly interacting particles, and its primary requirements are to provide good jet energy resolution and containment of showers to allow accurate estimates of the missing transverse energy and to protect the muon system against punch-through. The HCAL is 11 interaction lengths in depth, and consists of several regions, with the barrel, outer barrel and endcap providing pseudo-rapidity coverage of $|\eta| < 3$, and the hadron forward calorimeter providing coverage over the range $3 < |\eta| < 5$. The measured energy resolution of the Hadronic Barrel calorimeter using test beam was found to be

$$\frac{\sigma(E)}{E} = \frac{94.3\%}{\sqrt{E}} \oplus 8.4\% \tag{3.2}$$

compared to the design value of $\frac{\sigma(E)}{E} = \frac{100\%}{\sqrt{E}} \oplus 4.5\%$.

3.2.4 Muon Chambers

Muons do not feel the strong force, and are too massive to radiate energy away via Bremsstrahlung (a particle of mass m radiates at a rate proportional to m^{-4}). Instead, they lose their energy by ionisation, and outside the superconducting solenoid are four muon detection layers interleaved with the iron return yokes. Three types of gaseous chamber are used. Measurements from the Drift Tube (DT) chambers in the barrel ($|\eta| < 2.1$), the Cathode Strip Chambers (CSC) in the end-cap disks ($0.8 < |\eta| < 2.4$) and the Resistive Plate Chambers (RPC) in both the barrel and endcap ($|\eta| < 1.6$) are used in a complementary fashion for triggering and reconstruction. The best reconstruction performance is obtained when the muon chamber information is combined with the inner tracking information, as shown in Figure 3.7.

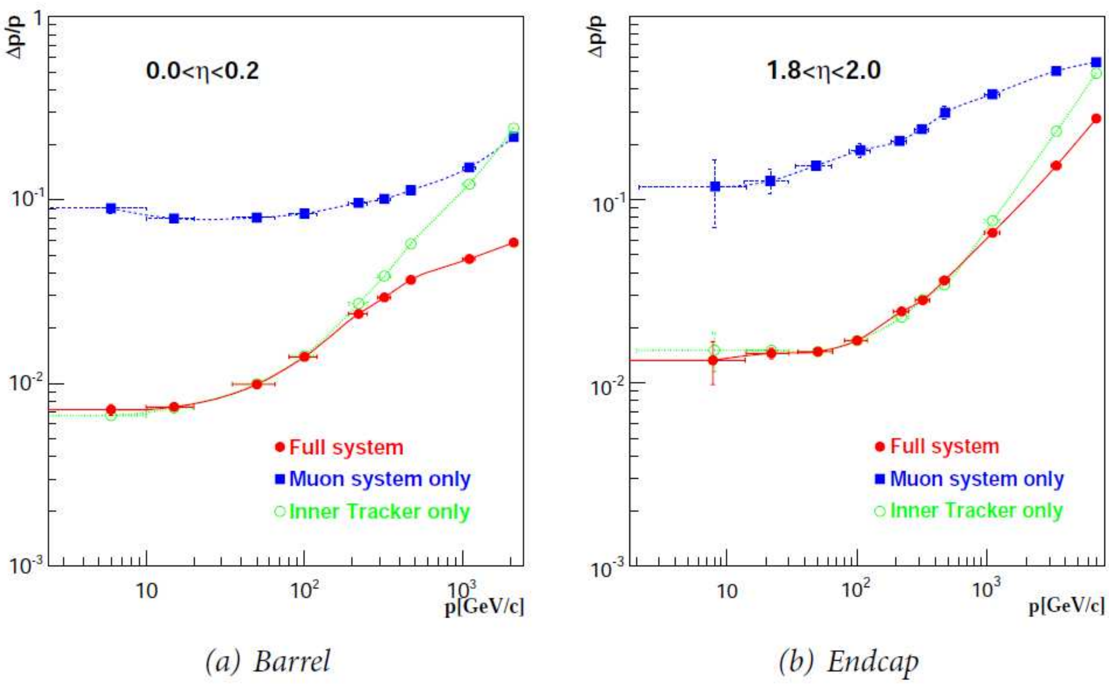

Figure 3.7: The momentum resolution ($\Delta p/p$) of reconstructed muons as a function of muon momentum in both the (a) barrel, and (b) endcap regions of the CMS detector. [4]

Chapter 4

Commissioning the CMS Global Calorimeter Trigger

4.1 The Need for a Trigger

As described in Section 3.1, bunches of protons at the LHC cross at a rate of 40 MHz, and there are 22 events per bunch crossing on average. This corresponds to approximately 1 MB of data per such crossing, which is equivalent to a data rate of $\mathcal{O}(10^{12})$ bytes per second. When it comes to saving these data, there are two limits to consider. The first is how quickly data can be saved to tape (this is of the order of a few 100 Hz), whilst the second is a bandwidth limit on the electronics of the Data Acquisition (DAQ) system (this is around 100 kHz). This means that in order to overcome the discrepancy between the production and storage rates, there must be a certain amount of online selection, i.e. before any events are stored.

At the CMS, this is achieved in the form of a two-level trigger system, the Level-1 (L1) trigger and the High-Level Trigger (HLT), an overview of which is shown in Figure 4.1. The trigger system reconstructs physics objects using raw detector data of a coarser granularity (for reasons of latency) and selects the data to be recorded based on the properties of these reconstructed objects, e.g. the transverse energy of a reconstructed jet. The choice of what exactly to trigger on is motivated from

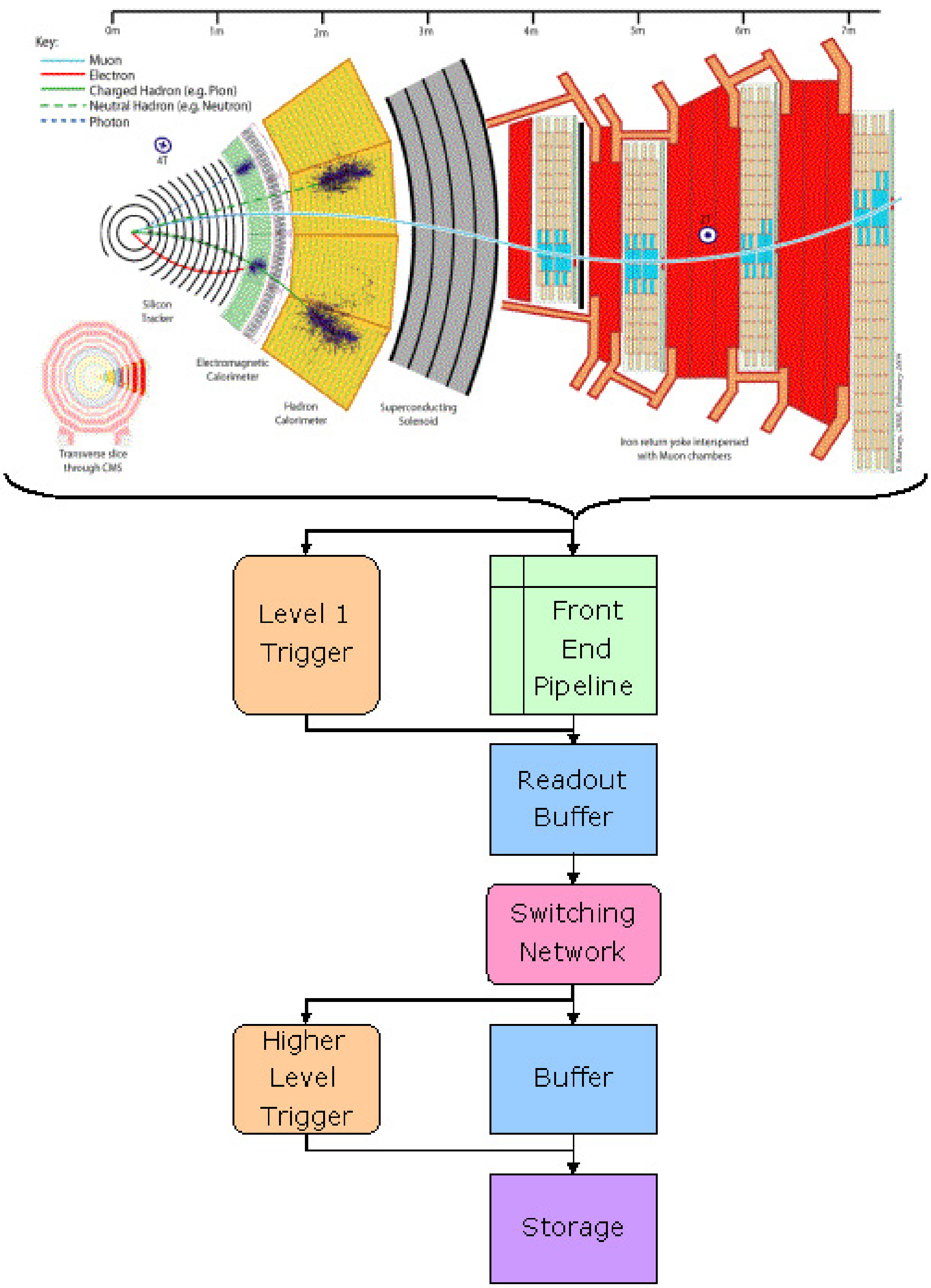

Figure 4.1: An overview of the two-level trigger system used at the CMS. The pipeline length on the front-end electronics is 4.0 μs, by which time the Level-1 Trigger must have made a decision on whether or not to pass the event onto the High-Level Trigger. [5]

the event signatures discussed in Section 3.2, namely jets, electrons, photons, muons and total and missing transverse energy quantities.

The CMS L1 trigger is designed to reduce the event rate from 40 MHz to 100 kHz using data from the calorimeters and muon chambers, but not the tracker. The system is also designed to be free of dead time, i.e. data from each and every bunch crossing is analysed without any interference from other bunch crossings. This forbids the use of iterative algorithms, and in turn dictates the use of a pipelined processing architecture. The system is therefore a high-bandwidth, fixed-latency 'image processor', where all data may be stored for up to 4.0μs (160 bunch crossings) in pipeline memories on the respective subdetector front-end electronics. During this time, the L1 trigger algorithms must make decisions every 25 ns on whether or not to pass the event on to the HLT for further consideration. The trigger algorithms are implemented on a custom hardware platform composed of FPGAs (Field Programmable Gate Arrays) and ASICs (Application Specific Integrated Circuits), and are highly parallel in their approach in order to meet the overall latency constraints. FPGAs can also be reprogrammed to accommodate new ideas (as discussed in Chapter 5).

An overview of the CMS L1 trigger is shown in Figure 4.2, which shows the divide between the calorimeter and muon triggers. The Global Trigger (GT) uses information from both these systems to make a decision called the 'Level-1 Accept' (L1A). For example, the muon system (via the global muon trigger) supplies the top-four muon candidates ranked in momentum to the GT. This L1A decision is then propagated to all detector subsystems so that the raw information may be read out for analysis at the HLT. The calorimeter trigger is discussed in more detail in Section 4.2.

The HLT is designed to reduce the event rate from the L1 trigger from 100 kHz to 100 Hz. Seeded by the L1 information, it uses the complete detector information, both at the full resolution and including the tracker, to improve on the reconstruction of the objects. The HLT is implemented on a high speed PC farm, containing approximately 3000 computers. The selected events are then written to tape and analysed offline.

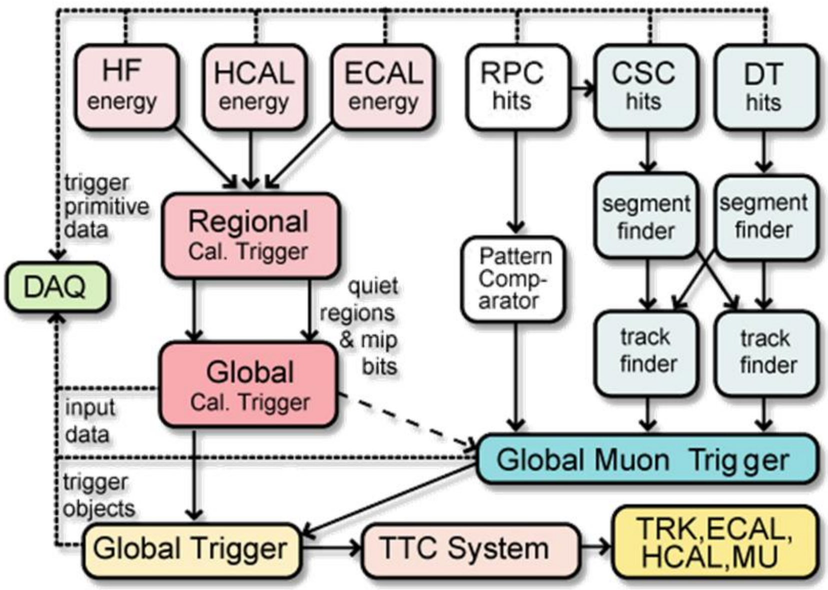

Figure 4.2: An overview of the CMS L1 trigger system, showing the global calorimeter and muon triggers, and the global trigger. [5]

4.2 The Level 1 Calorimeter Trigger

The objects passed from the calorimeter trigger to the GT include electron/photon and jet candidates. The corresponding algorithms which find such objects span different physical sizes in the detector, which determines how coarse-grained the input information must be. The CMS detector can be unwrapped and represented as a two-dimensional array of 396 calorimeter regions, with 18 divisions in ϕ ($-180\,^\circ < \phi \leq 180\,^\circ$) and 22 in η ($-5 < \eta < 5$). Each division in ϕ corresponds to $20\,^\circ$, whilst the η divisions correspond to $\Delta\eta \sim 0.348$ in the barrel, and $\Delta\eta = 0.5$ in the forward calorimeters. A calorimeter region is defined to be a group of 4×4 trigger towers. In the barrel, a trigger tower corresponds to 5×5 ECAL crystals, with the corresponding HCAL region behind them. The jet-finding algorithm works on a sliding window of 3×3 calorimeter regions across the entire (η, ϕ) space, whilst the electron/photon finder works on a sliding window of 3×3 trigger towers for $|\eta| < 3$. Given that electron/photon candidates span a much smaller physical space in the detector than jets, the respective calorimeter trigger algorithms are implemented in the hardware of the Regional Calorimeter Trigger (RCT) and the Global Calorimeter Trigger (GCT). The candidates are then sorted in terms of a quantity called rank by the GCT, before being passed to the GT. The rank is equivalent to the transverse energy, although it could in principle also contain information on the location of the candidates.

For every event, the GCT performs the following tasks:

- Electron/photon candidates - up to 72 non-isolated and 72 isolated electron/photon candidates found by the RCT are sorted, with the four highest-rank objects of each type passed to the GT. This is equivalent to a data rate of 29 Gbs^{-1} per electron type. A description of the electron/photon-finding algorithm is given in Section 4.2.1,
- Jet candidates - transverse energy sums supplied by the RCT as calorimeter regions (equivalent to an input data rate of 172.8 Gbs^{-1}) are used to perform jet-cluster finding, and the energies of the resulting jets are converted into ranks. The jets are then classified as either central, tau (τ), or forward, and the four highest-rank jets of each type are passed on to the GT. A description of the jet-finding algorithm is given in Section 4.2.2,
- Energy sums
  - The total transverse energy, E_T, is the scalar sum of all regional transverse energies.
  - The total jet transverse energy, H_T, is the scalar sum of all identified clustered jets with energy above a programmable threshold.
  - The missing transverse energy, E_T^{miss}, is the negative vector sum of all regional transverse energies. This is calculated by projecting regional transverse energies onto the x and y axes, rotating the resulting x and y components by $180\,^{\circ}$, and combining them as a vector sum. More information is given in Chapter 5

Two major extensions to the baseline system described above have also been identified and commissioned. The first of these relates to a H_T^{miss} trigger, the jet analogue of E_T^{miss}, which is discussed in Chapter 5. The second involves the innermost two rings of the hadronic forward (HF) calorimeter, in both positive and negative pseudo-rapidity. The total transverse energy in each of the four rings, known as the "HF Ring Sums", are calculated, as are the number of regions in each ring for which the energy deposition exceeds a programmable threshold, the "HF Bit Counts". A coincidence measurement of these quantities in both positive and negative pseudo-rapidity provides a method for triggering on minimum-bias events. An improvement to the identification method of τ-jets, discussed in Section 4.2.2, has also been implemented and commissioned.

In addition to these tasks, the GCT acts as a readout device for both itself and the RCT by storing information until receipt of a L1A, and subsequently sending these data to the DAQ system for both diagnostics and seeding at the HLT.

4.2.1 The Electron/Photon-Finding Algorithm

Given that tracking information is not included at L1, no attempt is made to distinguish between electron and photon candidates at this stage. Since electrons are 'narrow' objects, their detection algorithm occurs at the RCT stage, and works over a sliding window of 3×3 trigger towers. As shown in Figure 4.3, the energy deposition in the central trigger tower is first calculated, and added to the largest energy deposition of its four nearest neighbours, to ensure candidates split over two trigger towers are properly handled. If the resulting value is above a certain programmable threshold, the ratio of HCAL to ECAL energy deposition in the central tower is calculated. To ensure that the particle considered is not a hadron, this ratio is set to be below 5%. The Fine Grain (FG) algorithm is then performed, which examines the central tower only and ensures that there is a fractional energy deposition of over 90% in any contiguous 2×5 crystal strip along ϕ, in the whole 5×5 tower. If a candidate satisfies all such criteria, it is at least a non-isolated electron/photon candidate. To check whether or not it is isolated, both the FG algorithm and HCAL

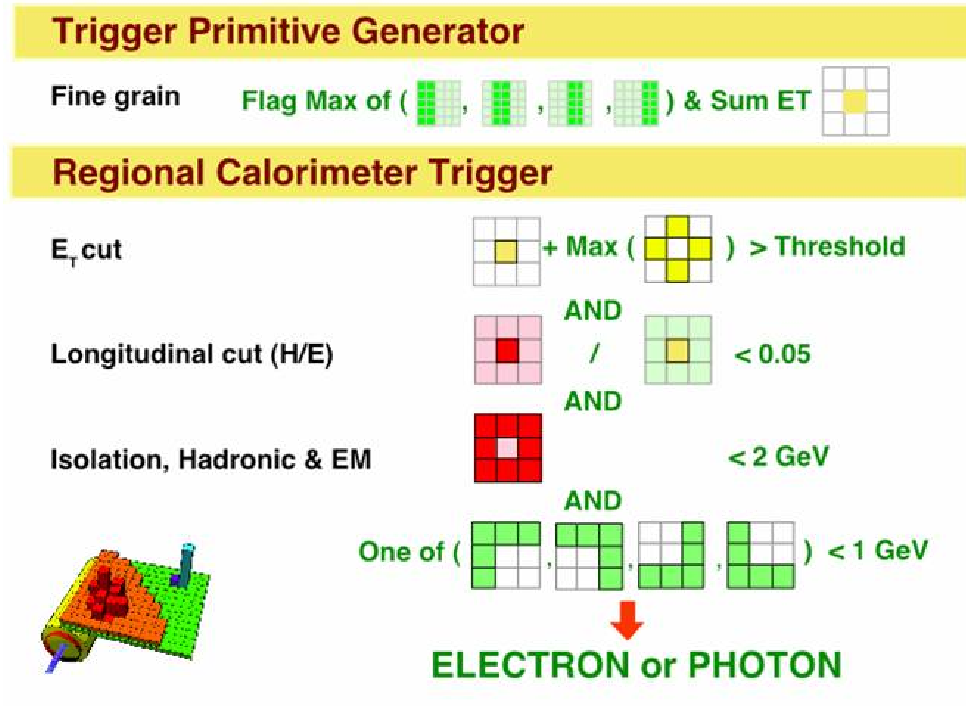

Figure 4.3: The electron/photon-finding algorithm at L1. Each cell represents a trigger tower, which is composed of 5 × 5 ECAL crystals in the barrel. The thresholds shown are all programmable. [5]

to ECAL energy deposition ratio are calculated for each of the central tower's 8 neighbouring cells. The algorithm then ensures that there is at least one 'quiet' corner. A 'quiet' corner is defined as one in which the ECAL deposition in each of the trigger towers in at least one of the four five-trigger-tower corners is below some programmable threshold (1 GeV). Upon passing these additional criteria, the object is identified as an isolated electron/photon candidate, and the RCT then sends this candidate data to the GCT, which sorts and selects the four highest-rank candidates to pass onto the GT.

4.2.2 The Jet-Finding Algorithm

A jet candidate is identified if the sum of the ECAL and HCAL energies of the central calorimeter region of the 3×3 window (see Figure 4.4) has an energy deposition greater than all its neighbours. The jet is then centred at this region, with the transverse energies of the 3×3 area summed into it. The transverse energy contributions from both the ECAL and HCAL for each calorimeter region are summed and supplied by the RCT. The RCT also calculates whether or not to set a τ-veto bit for each calorimeter region, depending on whether or not energy depositions in up to 4 contiguous trigger towers are below a programmable fraction of the regional E_T (see Figure 4.4(right)).

A jet found in the range $3 < |\eta| < 5$ is classified as a forward jet. A jet found in the range $|\eta| < 3$ can either be classified as a central or τ-jet, depending on the result of the τ-identification algorithm used. There are two such algorithms available in the GCT firmware:

- v1: If any of the nine τ-veto bits (one for each of the 3×3 regions that comprise the jet) is set, then τ-jet identification is vetoed, and the candidate is classified as a central jet. Conversely if none of the nine τ-veto bits are set then the jet is classified as a τ jet.

- v2: Using this algorithm, the τ-veto bits are ignored. Instead, for a jet candidate to be classified as a τ jet, up to a maximum of one of the eight calorimeter regions neighbouring the jet seed is permitted to have a transverse energy above some programmable isolation threshold. Otherwise, the candidate is identified as a central jet.

It is also possible to apply separate corrections to the top-four identified τ, central and forward jets, as a function of η and E_T. Whilst this feature was not utilised for 2010 data taking, it is expected to be used in future running.

4.2.3 The GCT Hardware

The hardware of the GCT is modular, and is divided into several cards each performing a different task relating to the determination of quantities and candidates thus identified. The data from the RCT are the input to the first set of these cards, the source cards, as shown in Figure 4.5(a). There are 63 source cards in the system, with seven belonging to each of the nine RCT-crate pairs, as shown in Fig. 4.6. These source cards serialise the data and re-transmit it on four optical

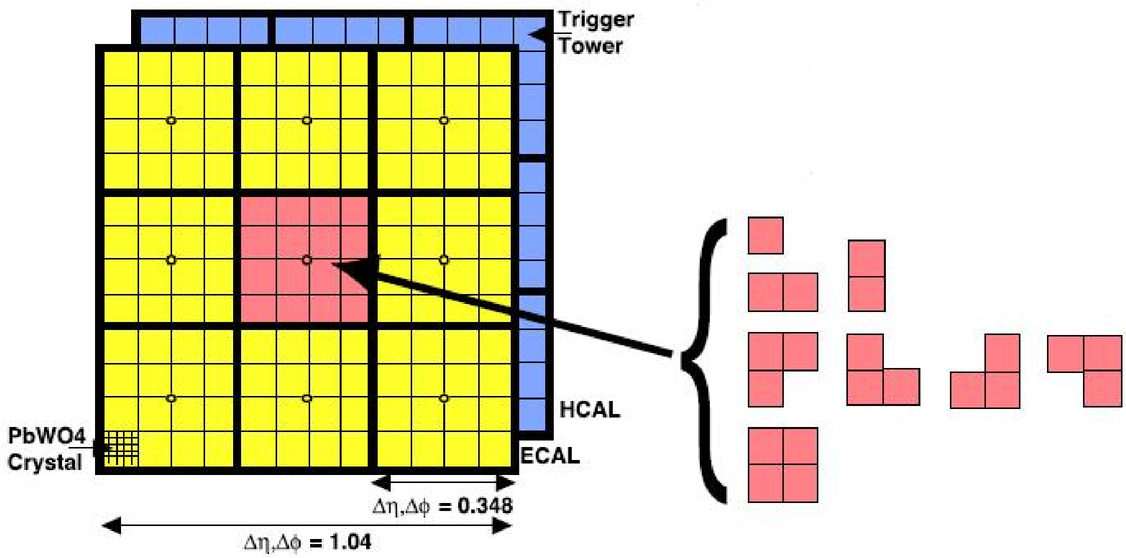

Figure 4.4: The 3×3 jet-finder window at L1. Each cell represents a trigger tower, which is the sum of the transverse energy contributions from both the ECAL and HCAL. The τ-jet veto patterns are shown on the right.

fibres, passing relevant information to the next set of cards, the electron and jet leaf cards (Figure 4.5(b)), and internally across the $\eta = 0$ region on an RCT-crate pair. This is necessary to ensure that the algorithms correctly analyse centrally-emitted electrons and jets, as discussed in Section 4.2.4.

There are two electron leaf cards, whose job it is to sort the electron candidates already found at the RCT level in both the $\eta > 0$ and $\eta < 0$ regions, and six jet leaf cards, which perform jet finding and are evenly split between the two η regions. Data from the jet leaf cards are then passed onto the wheel cards (Figre 4.5(c)), which sort jet candidates from both sides of the detector, in a similar vein to the electron leaf cards, and calculate energy sums. Finally, the concentrator card (Figure 4.5(d)) takes information on the electron candidates from the two electron leaf cards, and the jet candidates along with the energy sums from the two wheel cards, before communicating with the GT via an optical interface.

4.2.4 Jet-Finding Algorithm: Hardware Implementation

The challenges associated with building a system as specified above centre around handling the enormous data throughput and the processing required for the jet-

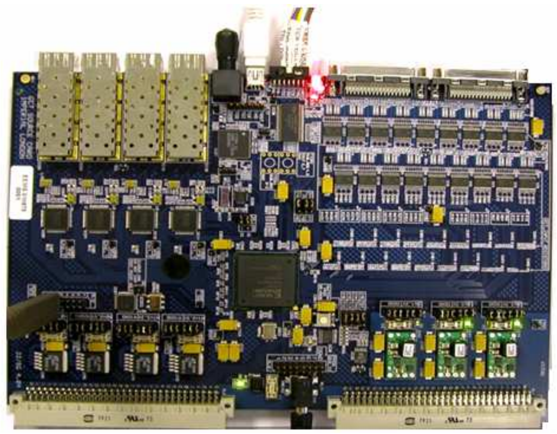

(a) The GCT source card.

(b) The GCT leaf card.

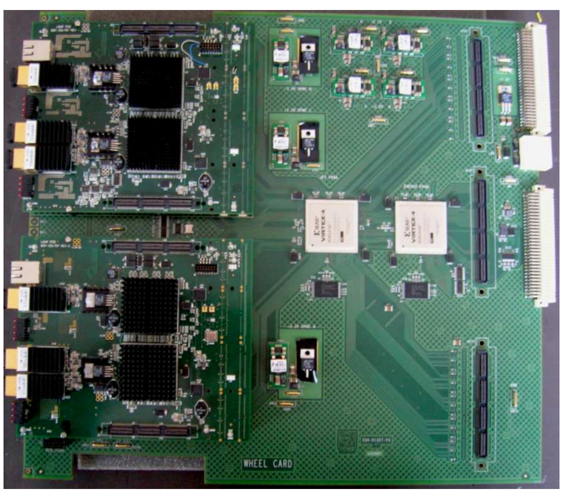

(c) The GCT wheel card.

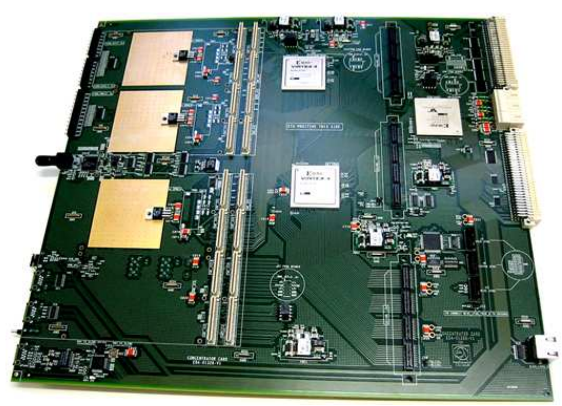

(d) The GCT concentrator card.

Figure 4.5: Photos of the GCT source card (a), leaf card (b), wheel card (c), and concentrator card (d). The wheel card is shown with two leaf cards attached.

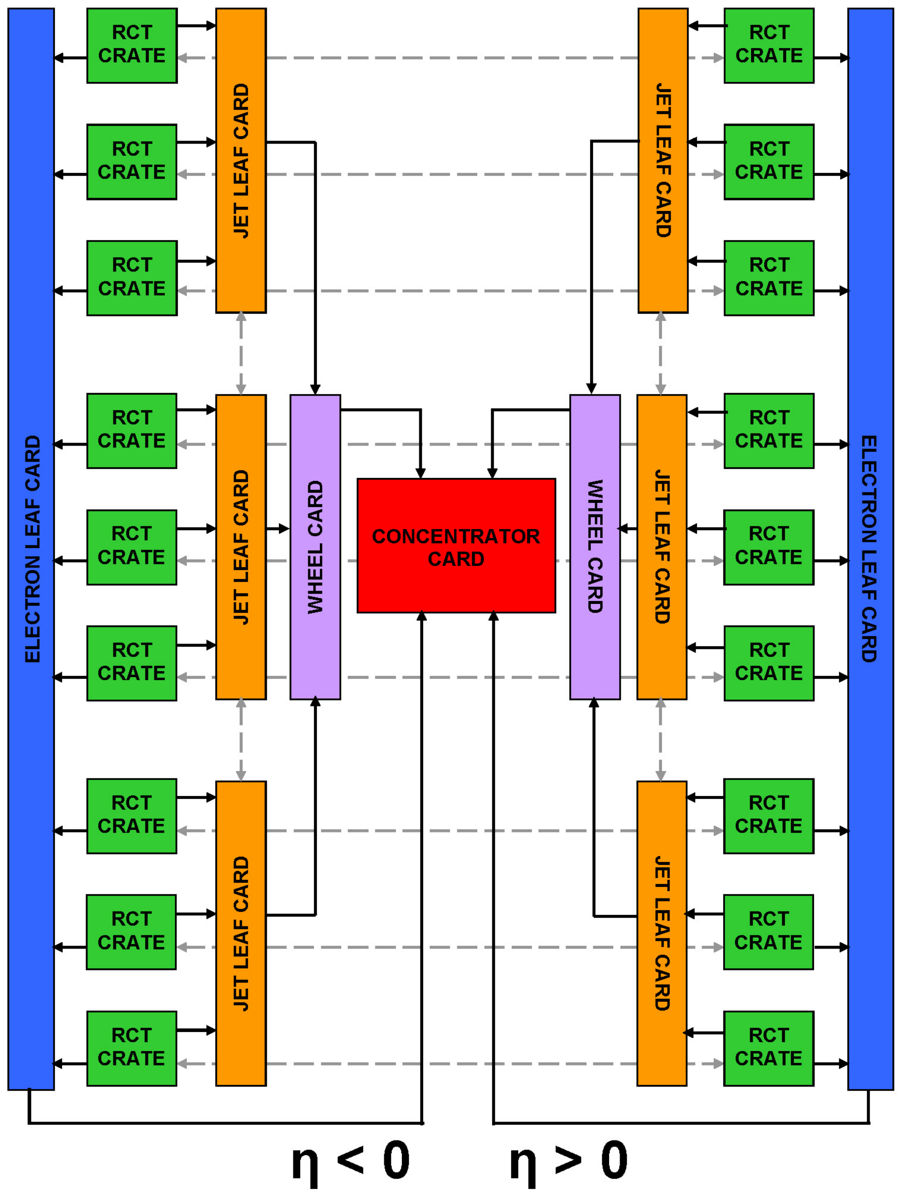

Figure 4.6: An overview of the GCT system, which is made up of several sets of cards. 63 source cards, split across 18 RCT-crates, are the input to the GCT. Solid arrows indicate the direction of data flow, whilst dashed arrows indicate data-sharing between crate-pairs across the $\eta = 0$ boundary as well as between jet leaf cards.

finding, along with the fact that a significant proportion of data has to be duplicated and shared for object finding to take place in the required latency. This sharing can require data flows similar in magnitude to that of the input data volume, depending on the method used.

In order to reduce the total data shared, the GCT hardware employs a pre-clustering algorithm [39] which involves 18 "jet-finders" operating on the entire (η, ϕ) space simultaneously, sharing information with their neighbours only when clustered jets are found. These jet-finders naturally map onto the boundaries defined by the RCT crates, as shown in Figure 4.7, so that each jet-finder acts on data from a single RCT crate, an area spanning 11 calorimeter regions in η (half the detector) and two in ϕ ($40\,^{\circ}$). A maximum of three jets can be found by each of the ϕ strips in a jet-finder, and hence 108 ($= 3 \times 2 \times 18$) in total per event. In order to maintain continuity across the $\eta = 0$ boundary, the original design made the immediately adjacent cells in η available to each jet-finder. This was subsequently changed to share information from two adjacent cells, for reasons as discussed in Section 4.3.4.

An example of the jet-finding algorithm is shown in Figure 4.8. The first stage involves creating a $2{\times}3$ mini-cluster around any local maxima identified in the $12{\times}2$ strip. Equality statements between regions are set-up such that the central cell is required to be greater than its neighbours in certain directions, but greater than or equal to its neighbours in others. This ensures that clustered jets are formed with a clear separation (i.e. at least one calorimeter region) in both η and ϕ.

In the second stage, the jet-finder transfers the three largest mini-clusters in a given ϕ strip to the closest ϕ strip on the neighbouring jet-finder. These are then compared against the existing mini-clusters in that ϕ strip, and those that are adjacent or diagonally adjacent to a larger mini-cluster are removed. The equalities are once again set-up to prevent problems occurring with two mini-clusters having the same value. In the third and fourth stages, the surviving mini-clusters have their three adjacent regions summed in to produce a $3{\times}3$ clustered jet.

The jet-finder as described reduces the data sharing requirement from 66% to 25% of the aggregate input data, when compared to the sliding window method. At this point, it is worth highlighting several features of the algorithm.

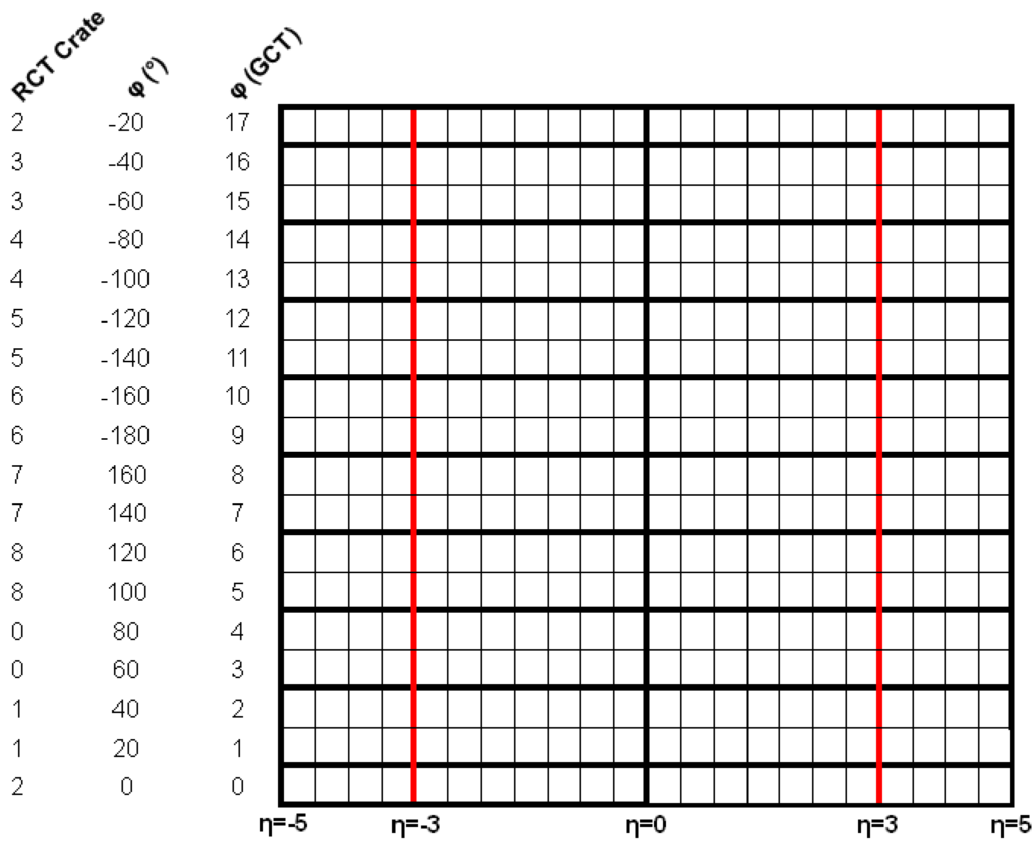

Figure 4.7: The calorimeter map that the 3×3 jet-finder operates over is made up of 396 calorimeter regions; each jet-finder is mapped onto an RCT crate which is made up of an 11×2 strip of these regions. RCT crate labels are shown for negative pseudo-rapidity only.

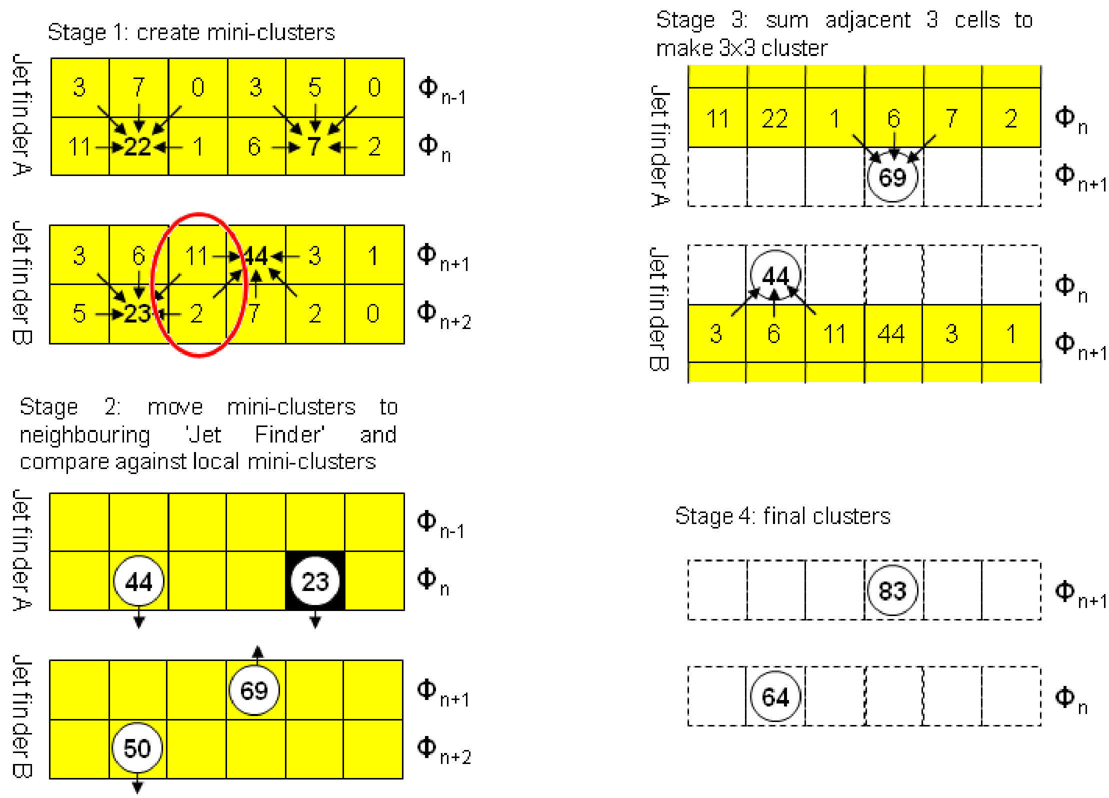

Figure 4.8: The jet-cluster method, with only six cells in η shown. An example of overlapping jets is highlighted.

- Vertical phase sensitivity - an artefact of pre-clustering is a sensitivity to where the boundaries between jet-finders are drawn. Working through the example of Figure 4.8 again, it should be clear that different results would be obtained if the jet-finder was offset by one unit in ϕ. It is important to note however, that whilst shifting the boundaries would result in different jet energies, the objects would not be missed by the trigger. Given each jet-finder spans two regions in ϕ, this vertical phase sensitivity is limited to just one unit in ϕ.

- Overlapping jets - a feature of the jet-finder as implemented is that it allows jets to be centred with a minimum of at least one region separation in both η and ϕ. At this limit, non-zero regions from overlapping 3×3 windows contribute energy to more than one jet, as highlighted in Figure 4.8. The net result is that there is more H_T than E_T in such events, as demonstrated by the correlation plot of Figure 4.9(a). Figure 4.9(b) however, shows the correlation plot produced by considering only events where the jet separation is at least two regions in both η and ϕ, showing no events with more H_T than E_T.

- "Maxima" finder - given that the jet-finder at L1 operates on a fixed 3×3 sliding window, it is only an approximation to the cone-finder which is used offline. If a jet spreads over an area larger than 3×3 regions, only the highest energy part will contribute to the L1 jet. In some cases therefore, not all energy depositions will contribute to a jet, thus partially explaining why there is more E_T than H_T in the correlation plot of Figure 4.9(b).

4.3 Commissioning the GCT

The GCT was installed and commissioned in the CMS experimental cavern in two stages, first with the necessary elements for the electron/photon trigger, and then with the remainder of the system for the jet and energy sum triggers. Given the complexity of the system, two major tools were developed and used extensively (Figure 4.10) that naturally map onto the two major steps needed for complete commissioning:

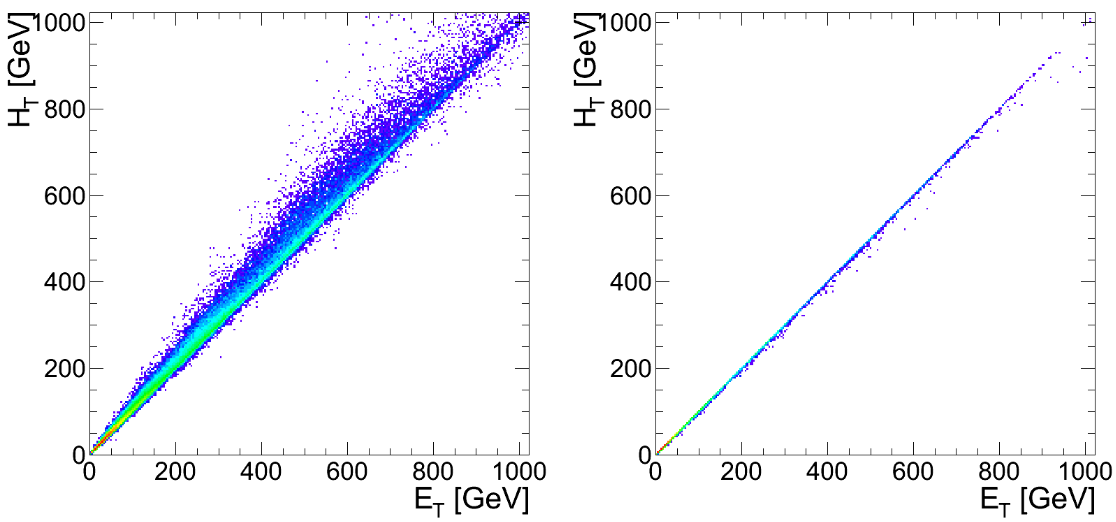

(a) The correlation with a minimum jet centre separation of one region in both η and ϕ.

(b) The correlation with a minimum jet centre separation of two regions in both η and ϕ.

Figure 4.9: Correlation plots of L1 H_T against L1 E_T for a QCD Monte Carlo generated sample as obtained from the GCT software emulator, one of the tools used during commissioning (see Section 4.3).

1. The ability to generate and load pattern files that emulate the input to the GCT, in order to validate the information reaching the start of the algorithms. Part of the GCT design allows for buffers where these patterns can be loaded at the input to the system, and then read back at the input to the processing algorithms. Between these steps, rearrangement of the data is necessary and so this validation is essential if an understanding of the jet-finding and subsequent processing is to make sense.

2. The ability to run the input to the GCT algorithms through a full C++ software emulation of the system and compare the outputs against each other. This bit-level emulation is made possible by the fact that the GCT is an entirely digital system, and ensures that the hardware functions as expected, which is especially useful for simulation studies.

In addition to the above, a one-sixth reconstruction of the GCT was assembled in the laboratory to enable fast testing, problem solving, and development when the full system was in use. In order to aid such debugging, intermediate data internal to the GCT hardware was also saved to disk, approximately doubling the size of the GCT output data, which is the reason why such information is suppressed during normal running.

4.3.1 Step 1a: Cable-mapping check

Before the tasks described above were undertaken, it was essential to check the cable mapping between the 252 optical fibres carrying data from the GCT input to the electronics which perform the algorithm processing. This was done by sending a unique number down each fibre, capturing at the output, and comparing to the number expected from a cable-mapping algorithm. This highlighted a small number of cable-mapping errors which were promptly resolved.

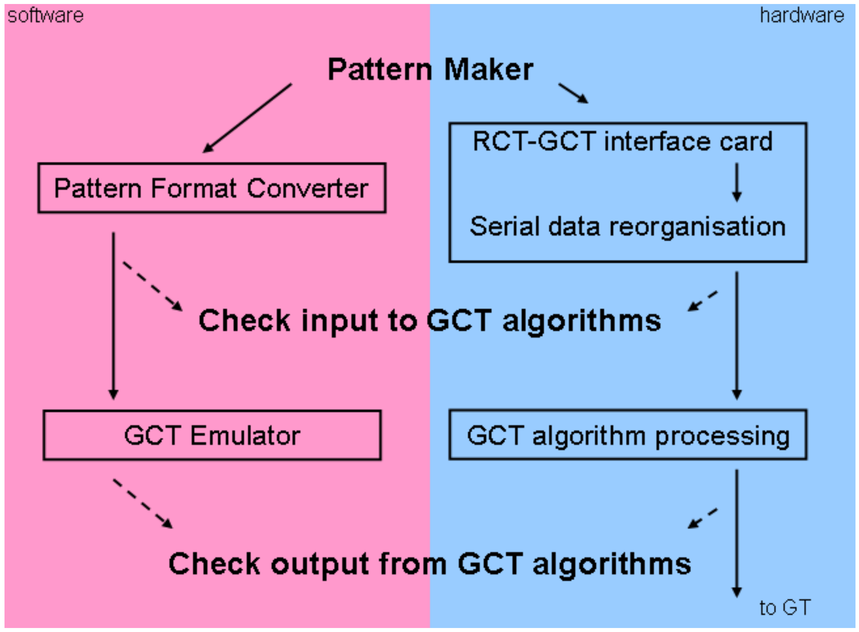

Figure 4.10: The GCT commissioning stages.

4.3.2 Step 1b: Link stability check

Once the cable mapping had been verified, the link stability was exhaustively tested. This was first done by testing the transmission quality of each link for data corruption using several different types of patterns. No cyclic redundancy check (CRC) or synchronisation loss errors were detected when tested in the laboratory system, and the links performed reliably each time. However, when ported to the experimental cavern system, CRC errors began to appear occasionally. This was eventually traced to a firmware synthesis/constraints problem that has since been resolved; a more complete description of this problem is discussed in [40]. The links were also stress tested continuously for over a fortnight, $\mathcal{O}(10^5)$ times, a process which involves resetting each link and transmitting data for approximately 10 seconds.

4.3.3 Step 1c: Validating the input to the GCT algorithms

As described, the GCT acts as a readout device for both itself and the RCT, and so a correct interpretation of the interface between these two systems is essential to validate the input area on which the algorithms operate. This is the first step in the

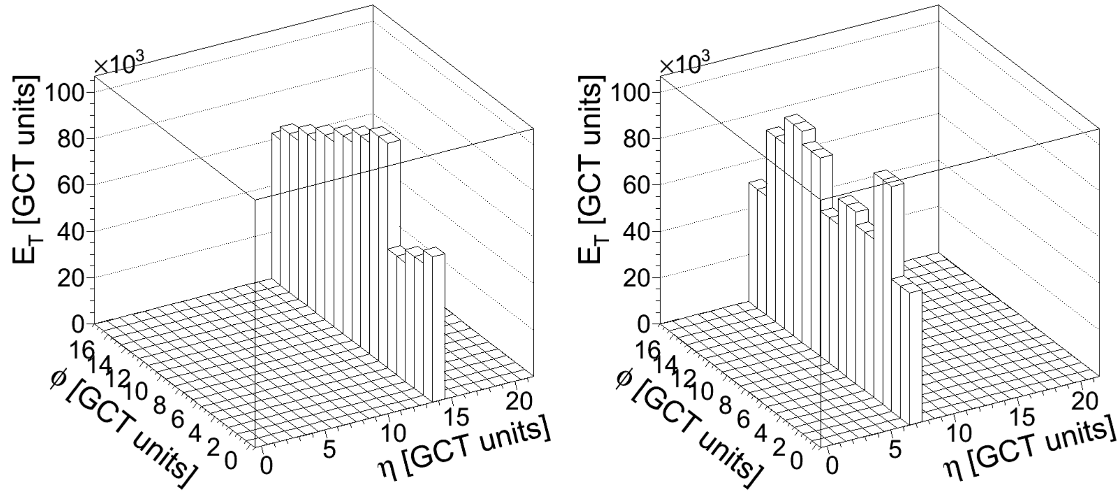

(a) The input regions to the GCT algorithms as generated with a pattern.

(b) The input regions to the GCT algorithms as seen by the hardware.

Figure 4.11: A sample pattern injected at the input to the GCT. Several geometric mismatches in η and ϕ can be seen between the intended input (a) and the corresponding output (b).

commissioning of the various outputs. Two checks were made at this point, both of which can be verified using patterns of varying complexity. The first checked that no errors were made in the reorganisation of serial data down the optical fibres into a format suitable for jet-finding and electron/photon candidate sorting. The second involved the interpretation of the raw data by the software unpacker. Patterns such as the one shown in Figure 4.11 were used to resolve several geometric mismatches in η and ϕ for the jet-finding input. The cause can be seen as a combination of a reflection along $\eta = 0$ and an ordering problem along the ϕ direction. A similar test for the electron/photon system was performed, which has a much simpler mapping. Another check was also made at this point to ensure that the duplicated regions which ensure the jet-finder remains continuous across the $\eta = 0$ boundary were identical. All such problems were resolved promptly.

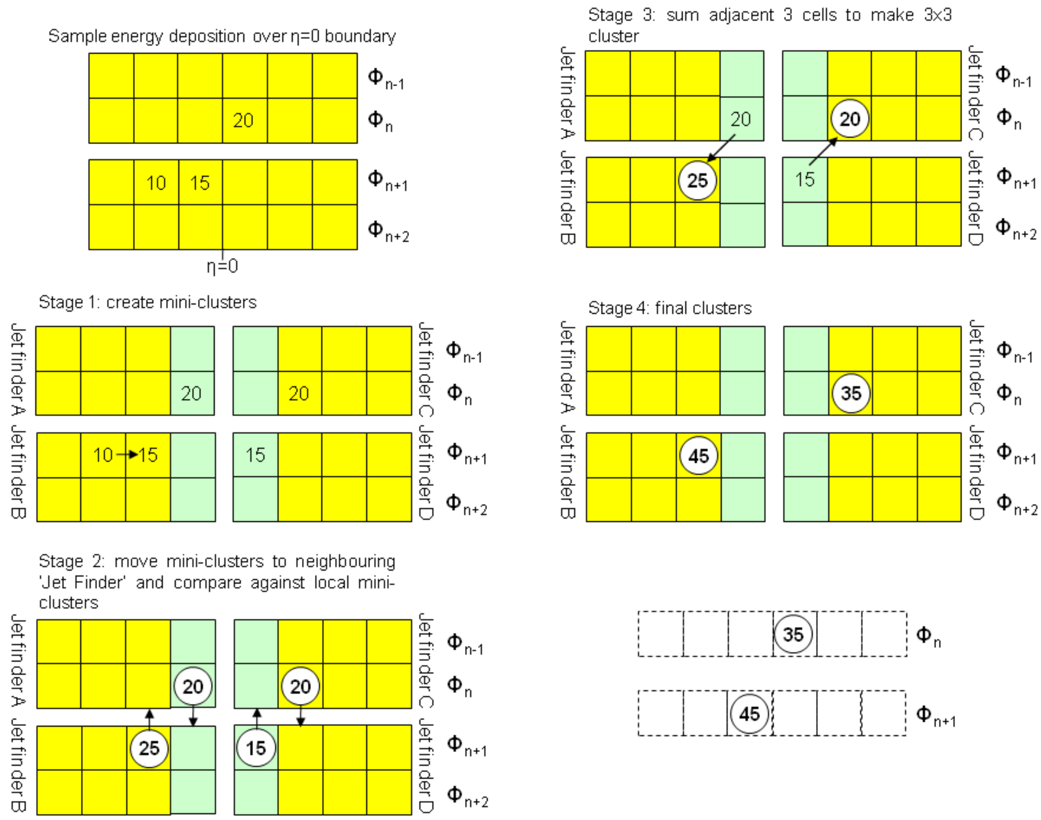

Figure 4.12: An illustration of the problem with sharing only one adjacent region at the $\eta = 0$ boundary with the jet finder as described in Figure 4.8

4.3.4 Step 2: Basic algorithm and emulator checks

Given the confidence that the input to the jet-finder was now correct, a similar logic was used to perform simple tests of the jet-finding algorithms. Patterns where the results of the jet-finding could be calculated by hand were used to test both the C++ emulator and hardware. Initially, single regions of energy were injected, and these picked out multiple problems, primarily in the interpretation between the different hardware components, but also in the software emulator. Several errors were seen with the classification of the different types of jets, and the handling of overflowing quantities.

More complicated patterns were then used to probe the behaviour of the jet-finding algorithm in hardware. Although the clustering worked as expected, a problem with the jet-finding along the $\eta = 0$ boundary was uncovered. This is summarised in Figure 4.12, which shows a sample energy deposition across the $\eta = 0$ boundary.

The first stage shows the information available to each of the four jet-finders, with duplicated regions shown with a green background. Once the pre-clusters are sent to neighbouring jet-finders and compared, it can be seen that a lack of duplicated information has resulted in two jets being created with no clear separation in η and ϕ, which is not allowed with the algorithm as prescribed. The result of this was an adaptation of the jet-finding algorithm, to use information from not one but two adjacent cells in η, so that each jet-finder operates on a 13×2 strip of calorimeter regions. In general, for an $n \times n$ jet finder (recall $n = 3$ for the GCT), where n is odd so that a jet centre can easily be defined, at least $\frac{(n+1)}{2}$ cells need to be shared across the boundary to maintain continuity.

4.4 Further Commissioning with Cosmic-Ray Muon Data

After completing the steps as outlined above, the GCT performance was tested by participation in global CMS cosmic-ray muon runs. In these runs, the muon trigger system of the CMS experiment was used as the primary trigger source, and consequently the calorimeter data taken by these triggers was dominated by noise. However, by using low thresholds and special calibrations it was possible to test the calorimeter trigger chain for electrons and jets using these data.

As the GCT reads out both its input and output, running the emulator over the input data provides a way of comparing the hardware output with that of simulation. Another software tool was developed at this stage to allow a detailed look at any discrepancies on an individual event basis, saving the input for such rogue events, along with the emulator and hardware output, in order to make debugging easier. Patterns were then created where necessary to recreate such problems in the laboratory system (described in Section 4.3) with additional debugging information. This software package also displays global rank, η and ϕ distributions of such errors, which may indicate the nature and hence number of underlying problems. Such a software tool proved invaluable in tracking down errors at the $\mathcal{O}(10^{-6})$ level. The typical output from this software package is shown in Figure 4.13. The folder names

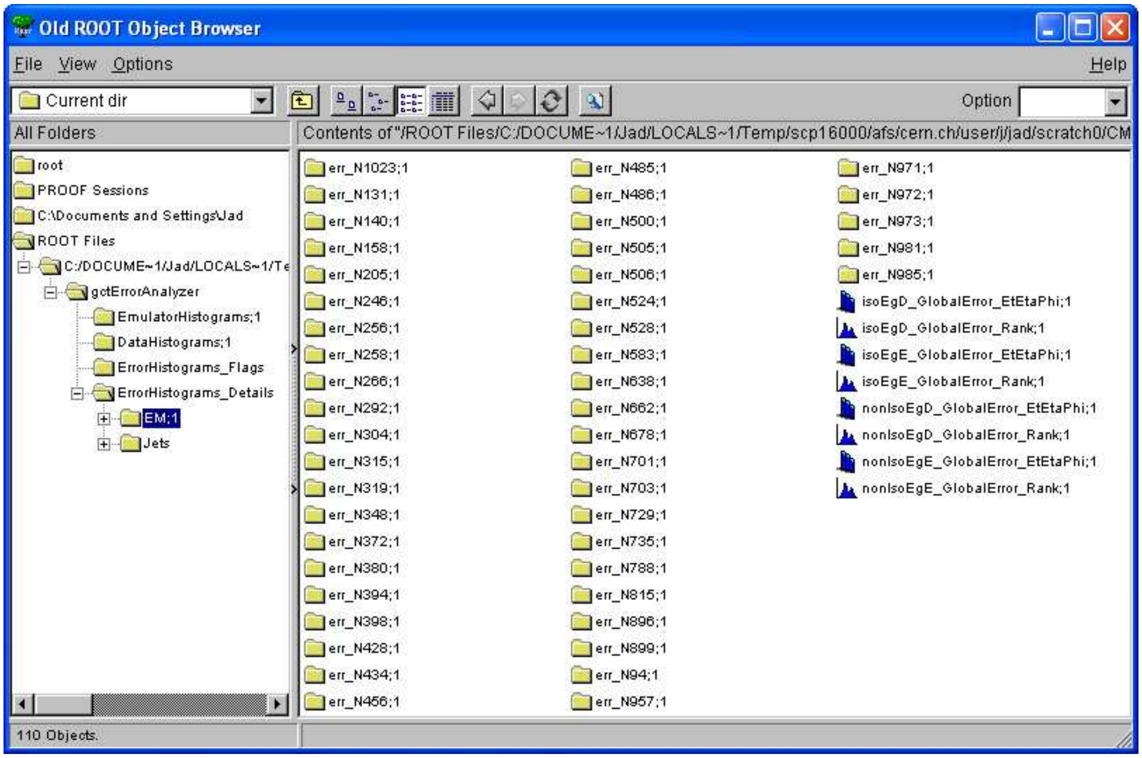

Figure 4.13: Sample output from the software package described in Section 4.4.

contain the event number (from a pattern test in this case), which allow the event to be tagged and isolated if required, and also an index that highlights the type of error (N in this case represents non-isolated electron/photon candidates). The global error histograms are shown on the right for both the hardware (data) and emulator outputs, represented by the D and E indices respectively. The software package also generates status flag histograms summarising the matching status of events, i.e. whether or not the rank and/or location (if applicable) of quantities matched, which is a useful metric in evaluating the overall status of the hardware vs emulator comparison. Also produced are the overall distributions for all quantities for both the emulator and hardware.

The GCT was involved in tens of thousands of such global runs, and discrepancies that occurred were identified quickly and understood promptly using this method. Such discrepancies can be grouped into three general categories:

1. Hardware problems - analysis of hundreds of millions of cosmic-ray muon events revealed subtle implementation features which patterns did not probe.

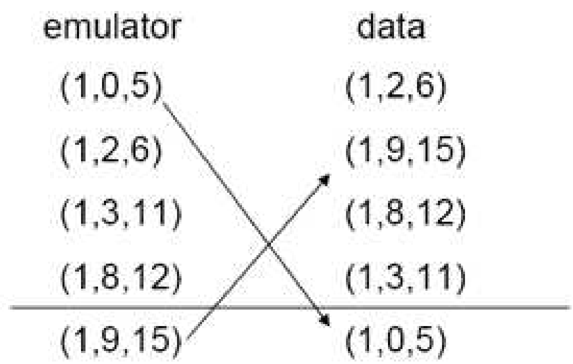

Figure 4.14: An illustration of the equal rank sorting discrepancy between the GCT software emulator and hardware. The (rank, η, ϕ) of the candidates are shown in GCT units.

These required updates to firmware, and more data to be taken for these updates to be verified.

2. Emulator problems - one of the most notable emulator discrepancies involved the preferences given to the sorting of equal-rank objects. Figure 4.14 shows an example of five equal-rank objects, which are found identically in both hardware and emulation. A difference in the priorities allocated during the sort process between the hardware and software meant that two different sets of top-four objects were passed on, leading to discrepancies on an individual event comparison basis. Whilst this was not a problem from a physics standpoint, such discrepancies had the effect of slowing down the validation process and masking other problems. Unlike firmware updates, software can be updated and verified without the need to take more data, as in this case where the software was adapted to describe the firmware sorting process.

3. Configuration problems - both the emulator and hardware have a set of configurable parameters which control the behaviour of the different triggers and system in general. For example there is a configurable threshold on the transverse energy of jets contributing to the total H_T. Discrepancies can arise from a mismatch between the emulator setup, and what these values were in the hardware when the data was taken. Although these configuration parameters are now stored in a database along with the time interval of their validity, some effort was required to ensure a correct match. Again, no more data has to be taken for such changes to be verified.

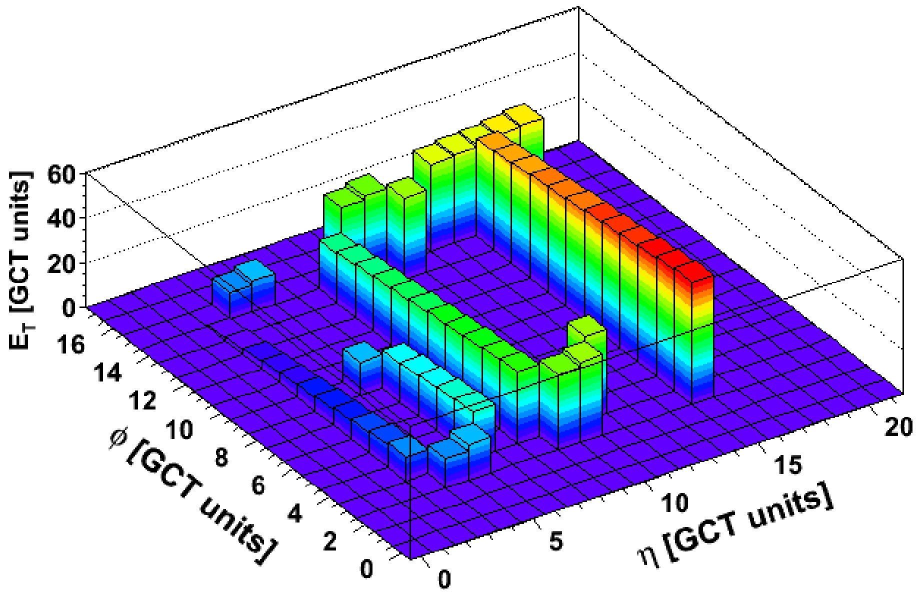

Figure 4.15: An example of a novelty pattern used during the GCT commissioning.

By using such global runs as an iterative process in commissioning the GCT, it should be noted that on some occasions, making progress on one front introduced errors elsewhere. In order to spot such occurrences, patterns were added to the suite described in Section 4.3 whenever new problems were uncovered. These were then cumulatively run and analysed for discrepancies with the emulator immediately after any firmware updates. Towards the end of the commissioning activities, several novelty patterns were added to this suite, an example of which is shown in Figure 4.15.

The tools developed to debug and commission the GCT discussed in this chapter are also used in a similar capacity for data quality monitoring (DQM). Currently, the data vs emulator comparisons are run online and it is planned that this will also be run offline. Any rogue events flagged up from such comparisons can then be placed into the DQM error stream (to be implemented), where they can be analysed with the software as described.

4.5 Performance

One way of determining the success of the procedure defined in this chapter is via a hardware vs emulator comparison from events generated by simulation. Figures 4.16 to 4.25 detail such a comparison for 2000 events from a possible SUSY signature, which shows 100% agreement for all GCT quantities on an event-by-event basis.

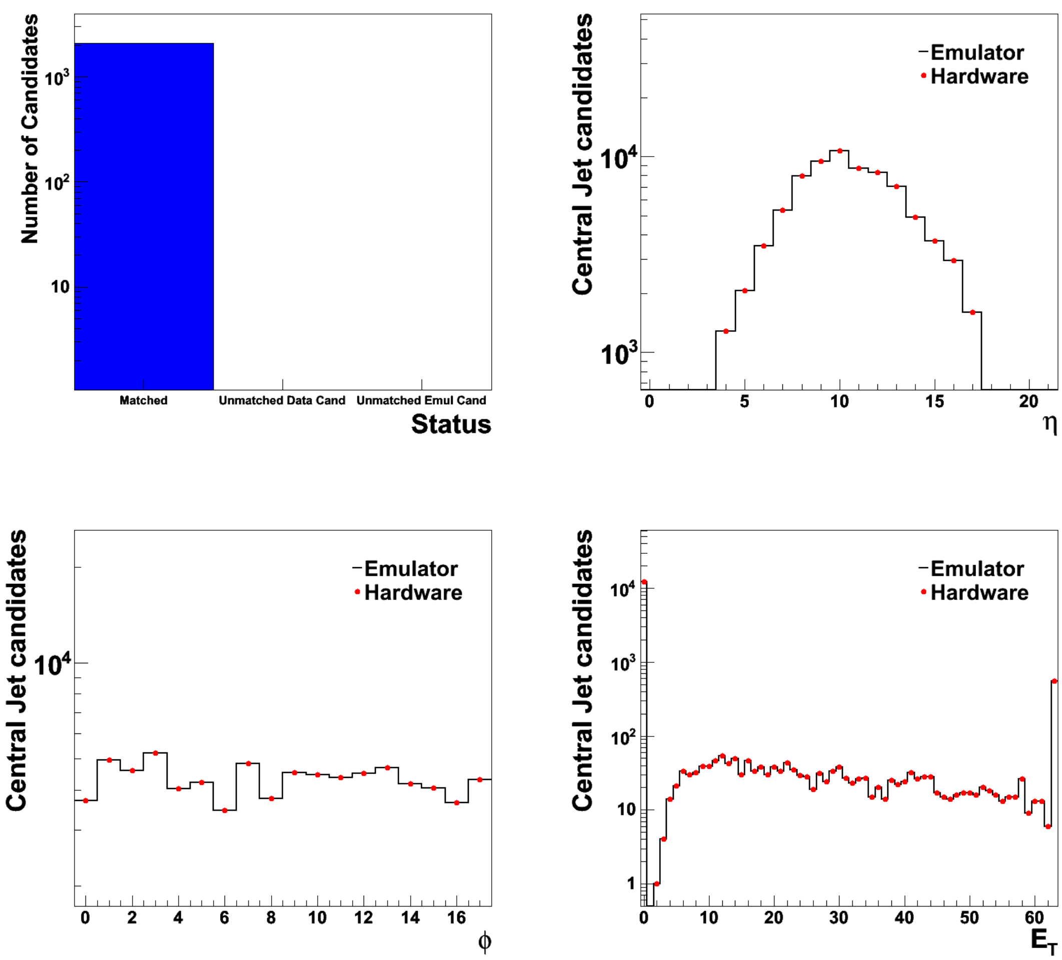

Figure 4.16: Central jet candidates

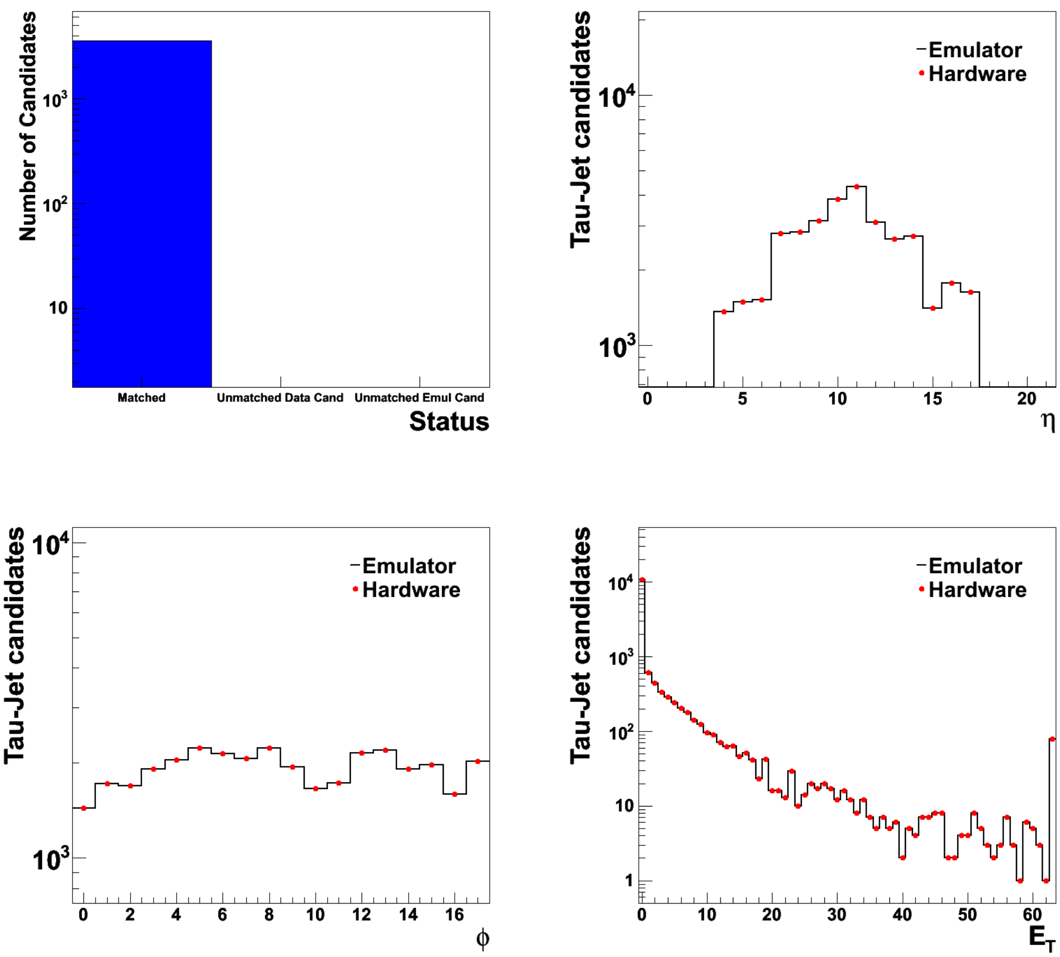

Figure 4.17: τ-jet candidates

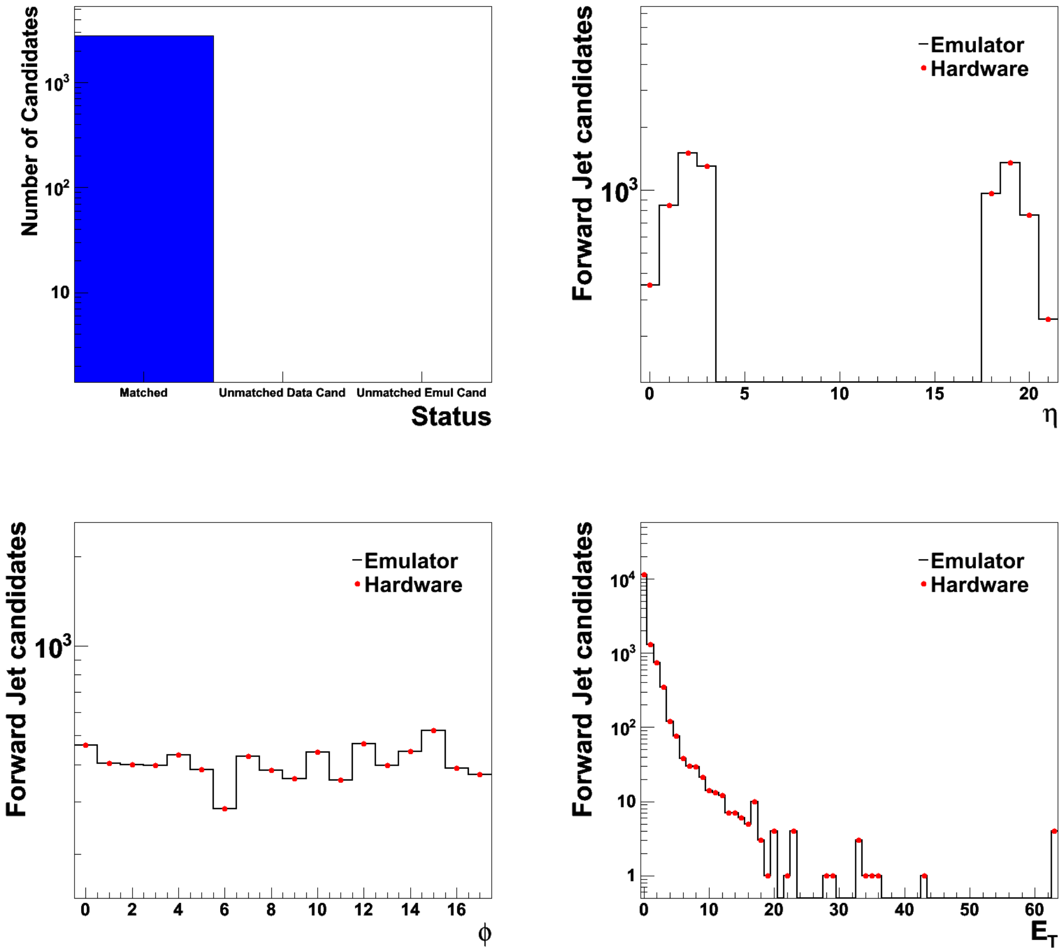

Figure 4.18: Forward jet candidates

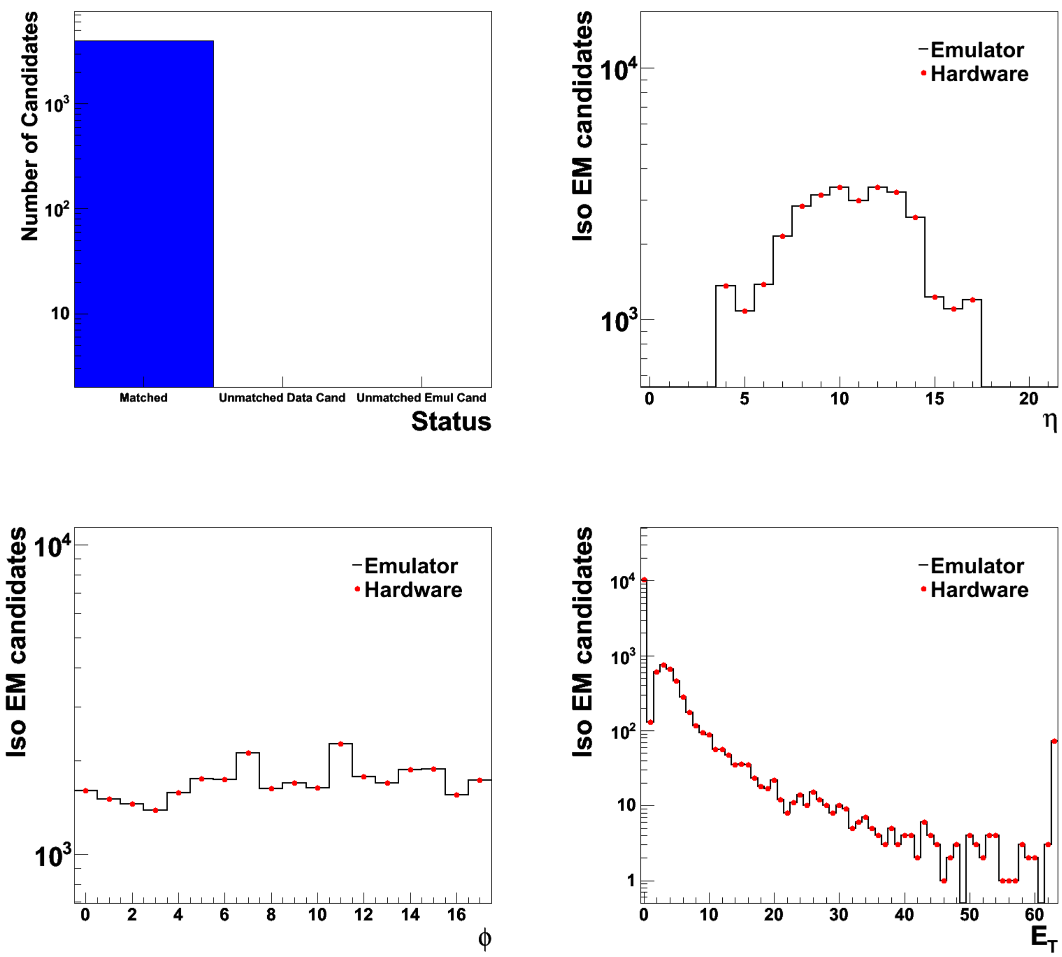

Figure 4.19: Isolated electron/photon candidates

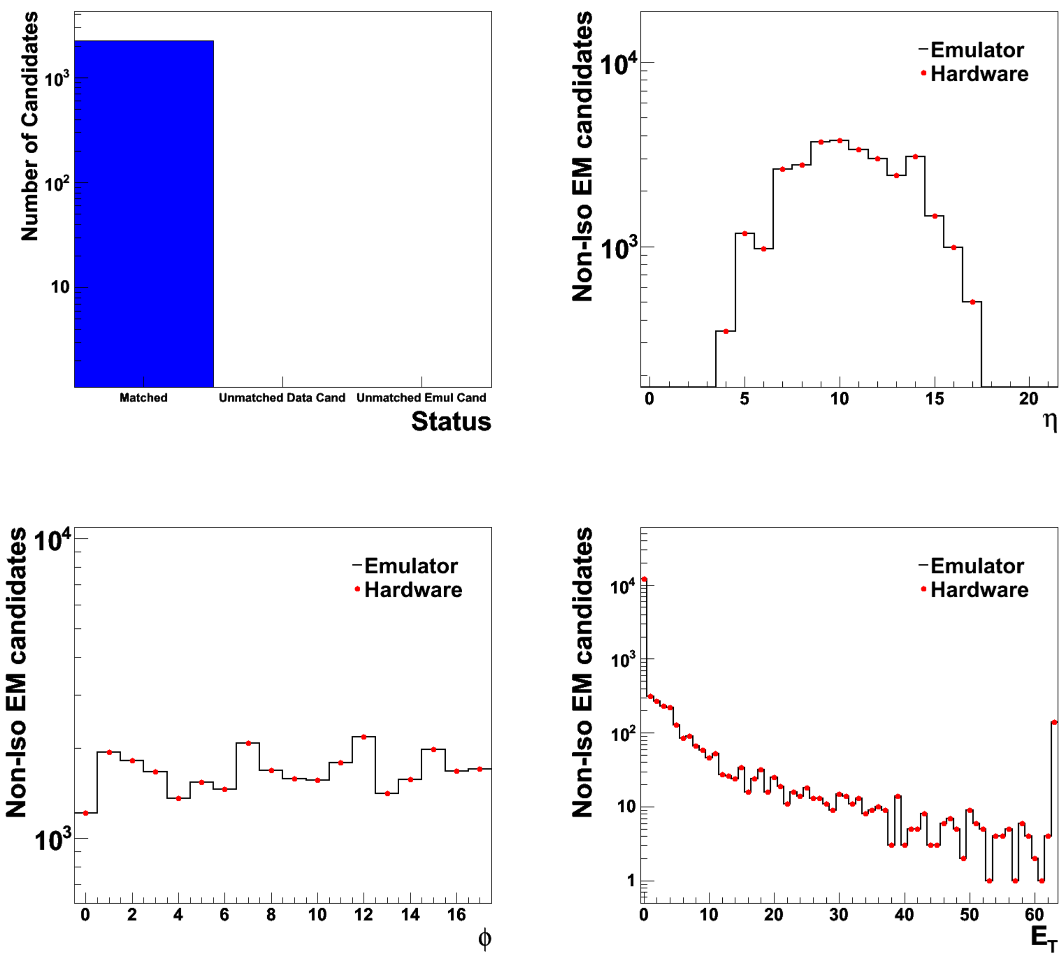

Figure 4.20: Non-isolated electron/photon candidates

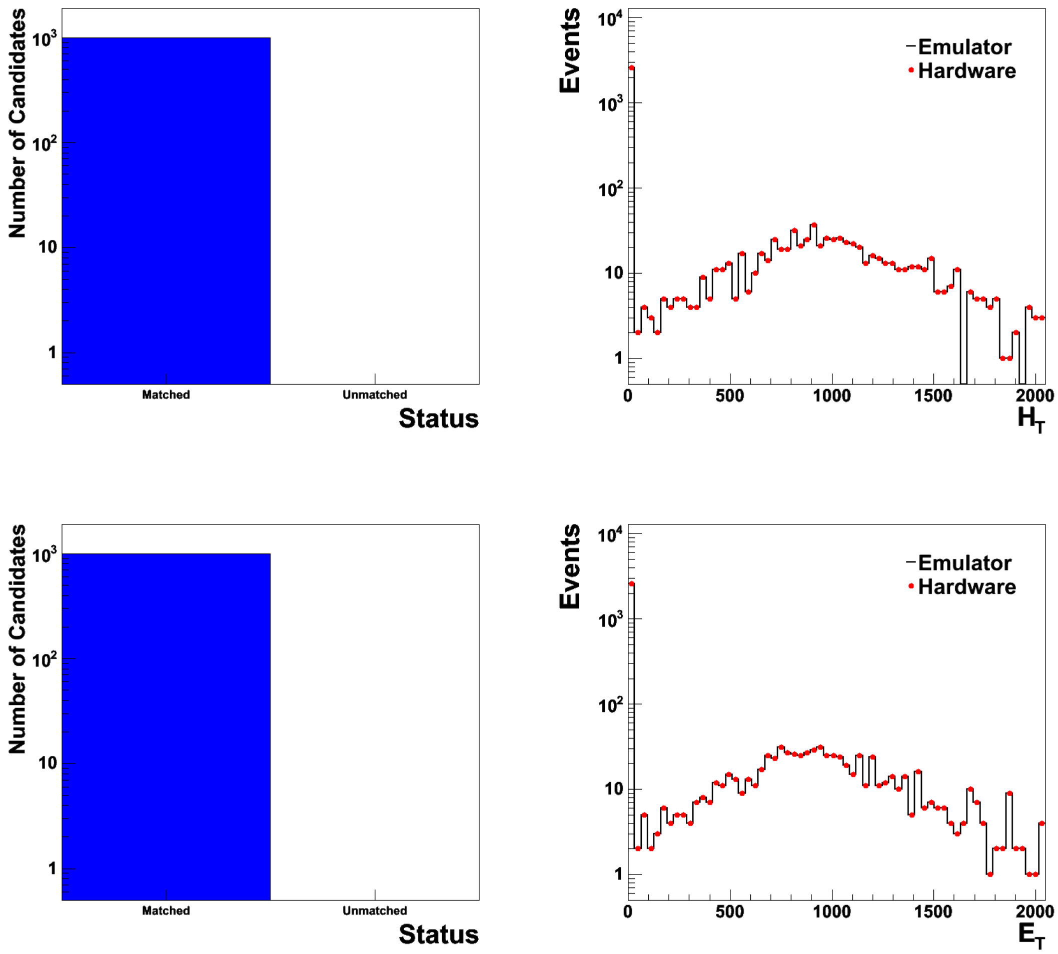

Figure 4.21: Total H_T (top) and total E_T (bottom)

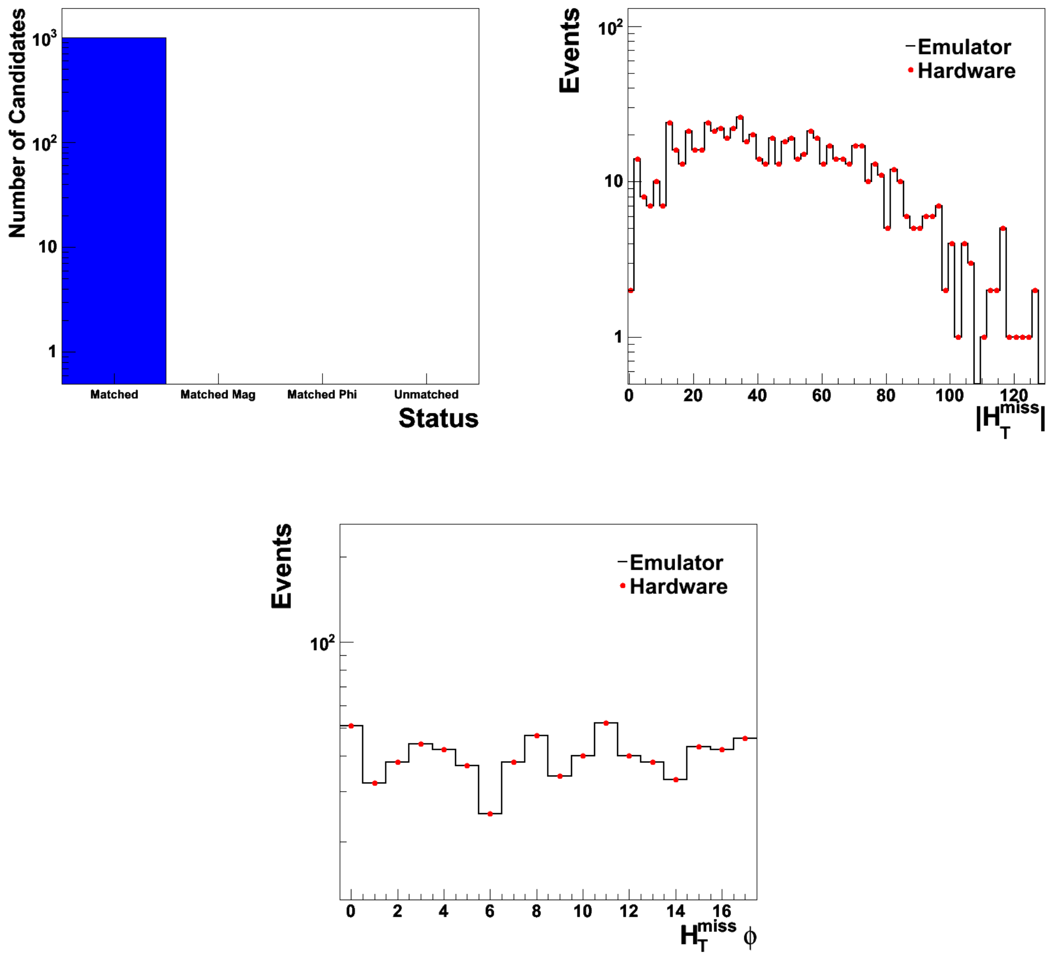

Figure 4.22: Missing H_T

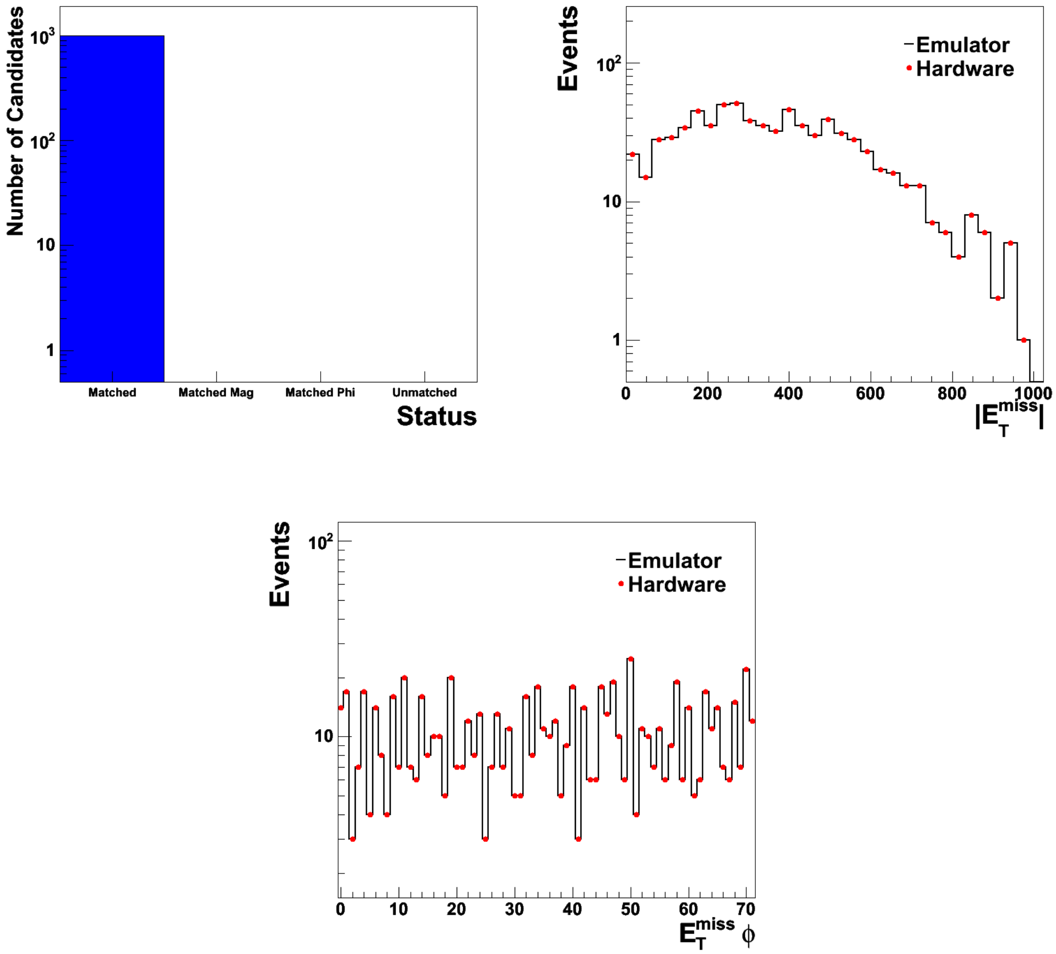

Figure 4.23: Missing E_T

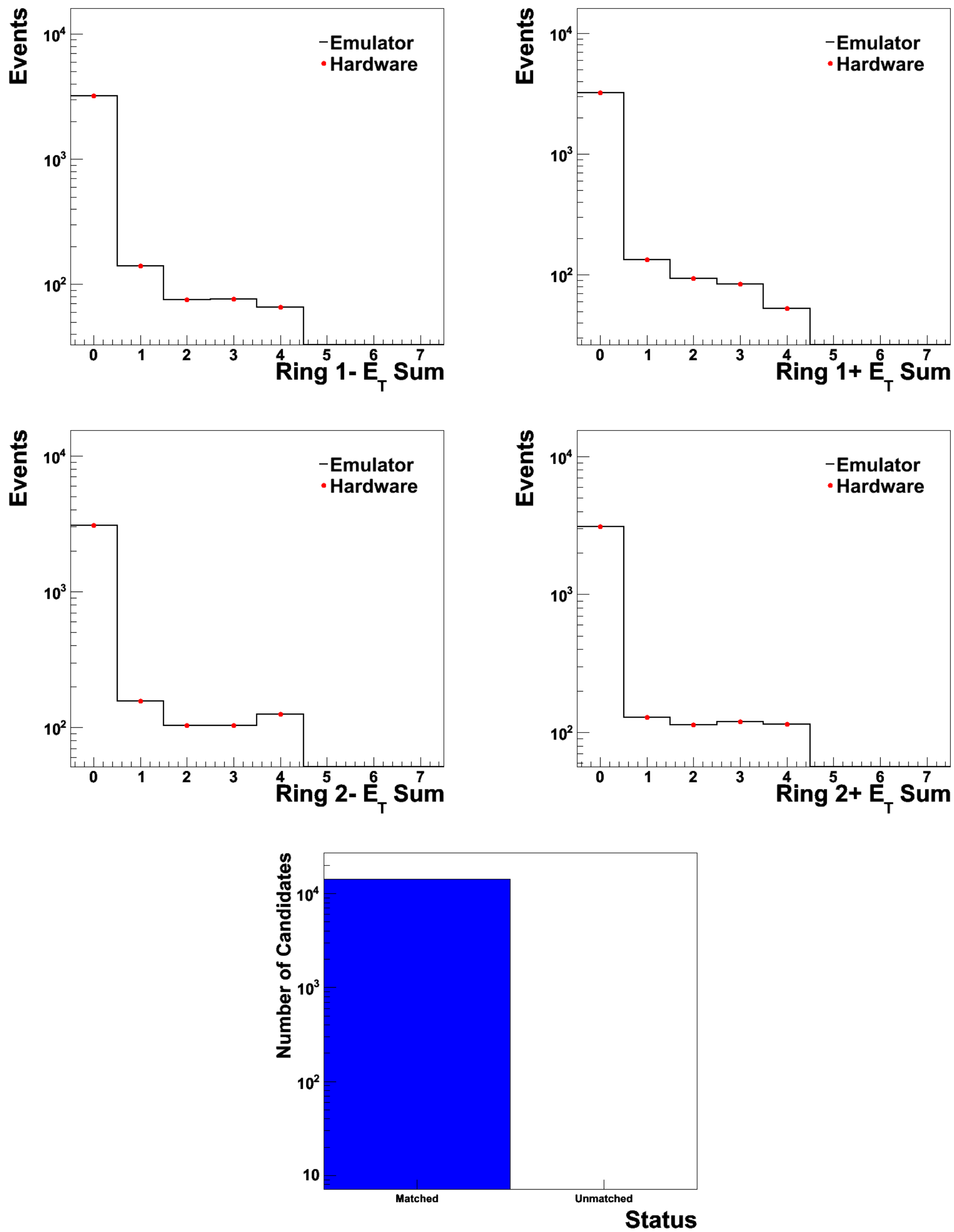

Figure 4.24: The HF ring E_T sums; inner ring in negative rapidity (top left), inner ring in positive rapidity (top right), second ring in negative rapidity (centre left), second ring in positive rapidity (centre right).

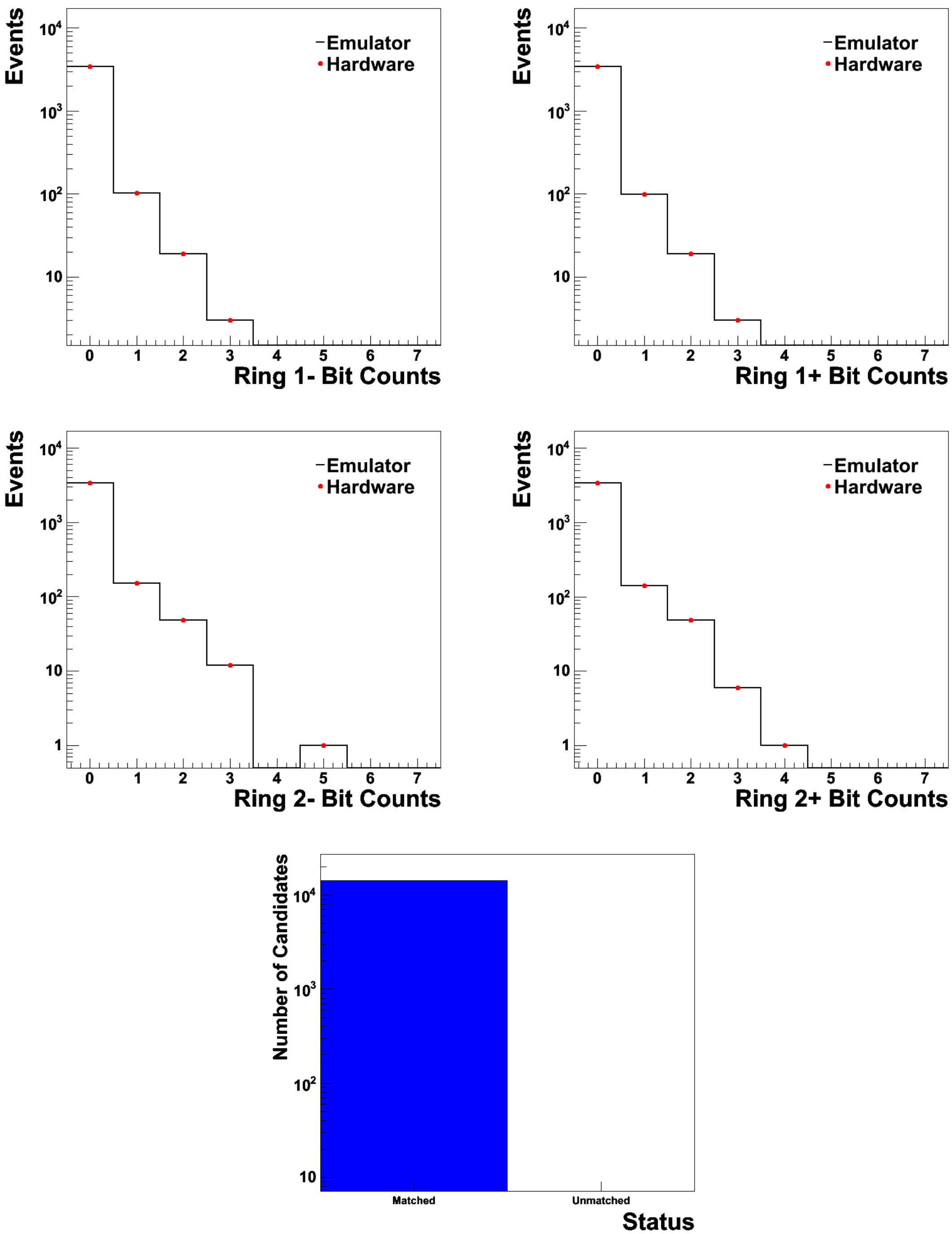

Figure 4.25: The HF ring bit counts above threshold; inner ring in negative rapidity (top left), inner ring in positive rapidity (top right), second ring in negative rapidity (centre left), second ring in positive rapidity (centre right).

Chapter 5

The Level-1 Missing H_T Trigger

5.1 Introduction

As discussed in Chapter 4, the Level-1 Trigger of the CMS experiment is designed to reduce the LHC event rate from 40 MHz to 100 kHz using information from the CMS calorimeters and muon chambers. One such trigger, the missing transverse energy (E_T^{miss}), is computed every event by calculating the vector sum of transverse-energy deposits from all 396 calorimeter regions, followed by a rotation through 180°. This is important for many different analyses, not least because large amounts of E_T^{miss} may indicate the existence of physics beyond the Standard Model. For example, SUSY is expected to have such a signature via the neutralino, and could be observed with a much lower integrated luminosity than for a potential discovery of the Higgs Boson. A missing energy trigger which is fast to commission and not affected by instrumental effects, pile-up, detector noise, hot channels etc. will therefore be important. It has been suggested in previous studies [41] and experiences at the Tevatron [42], that a missing transverse energy sum computed not from all calorimeter region E_T deposits, but from all jet-E_T deposits found in an event, a missing H_T trigger (H_T^{miss}), would satisfy this criterion.

The performance between these two missing energy triggers is compared in this chapter, by studying the QCD rate versus signal efficiency curves, for both SUSY and

Standard Model signals in simulation. Samples of both the mSUGRA benchmark parameter points [43] LM0 and LM1, and a $t\bar{t}$+jets sample are compared against a QCD sample, as this will have the largest cross-section for any process at the LHC (see Figure 3.1). As well as looking at missing energy triggers, the total transverse energy (E_T) and jet transverse energy (H_T) triggers are also compared. The response of the jet-based energy sums, H_T and H_T^{miss}, to jet energy corrections, individual E_T^{jet} thresholds, and restrictions on the acceptance of jets are also quantified.

5.2 Hardware Implementation

The total number of jets that can be found in an event at Level-1, and hence those contributing to both H_T and H_T^{miss}, is 108. A schematic of how the energy sum quantities are calculated in the GCT is shown in Figure 5.1. The total E_T is equal to $\sum_i E_T^i$ where i runs over all calorimeter regions, whilst the total H_T is equal to $\sum_j E_T^{\text{jet},j}$ where j runs over all jets found above a programmable transverse energy threshold. The missing energy sums are calculated by first working out the respective sums in bands of phi. These are then resolved into the corresponding x and y components, before being vectorially added, rotated by 180°, and recombined in quadrature into a magnitude and an angle. The total missing energy components are therefore equal to $E_T^{\text{miss},x} = -\sum_i E_T^i \cos\phi_i$ and $E_T^{\text{miss},y} = -\sum_i E_T^i \sin\phi_i$. The corresponding H_T^{miss} components are calculated as in the total energy case, by replacing the summation from calorimeter regions to all jets found above a programmable transverse energy threshold. The programmable thresholds for H_T and H_T^{miss} are independent.

The E_T^{miss} calculations are performed in hardware using the CORDIC algorithm [44] [45]. Given that the H_T^{miss} calculation can only be performed after jet-finding, it is required to be faster (to meet the overall trigger latency), and so a look-up-table is instead used to perform the x and y projections. This in turn requires more bandwidth. The precision of all the energy sum trigger quantities at the GCT are summarised in Table 5.1. The upper limit on the H_T^{miss} precision, seven bits, is a

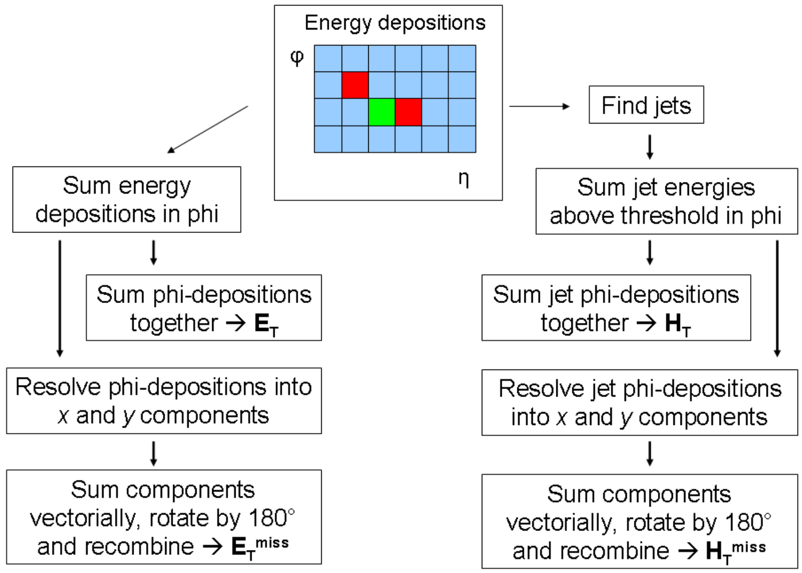

Figure 5.1: A schematic of the energy sum calculations performed in the GCT on the calorimeter regions.

Table 5.1: The precision of the energy sum trigger quantities in the GCT.

Quantity	Bit Precision
E_T	12 + overflow
H_T	12 + overflow
E_T^{miss} magnitude:angle	12 + overflow : 7
H_T^{miss} magnitude:angle	7 + overflow : 5

hardware bandwidth constraint; a result of the fact that the H_T^{miss} trigger was implemented retrospectively into the GCT specification. In order to make the ranges of the two missing energy trigger quantities more similar, the bottom three bits of the H_T^{miss} magnitude are truncated.

5.2.1 Jet-based Configurable Parameters

The use of jet-based energy sums at Level-1 provides an opportunity for two major configurable parameters, both of which are studied:

1. **Jet energy corrections**. Jet energy corrections are programmable (E_T, η) dependent corrections that, when applied, are applied to every jet that

is found. The η-dependent correction is designed to compensate for the response and geometry of the detector, whilst the E_T-dependent correction is designed to account for both the non-linear and non-compensating nature of the calorimeters. In the current implementation of the GCT it is not possible to apply these corrections to the H_T and H_T^{miss} quantities, but their effects are studied nevertheless to understand their potential and determine if they should be included in a possible upgrade. The jet energy corrections used in this study are discussed in [46].

2. **A programmable threshold cut on the jets used in the energy sums**. As previously discussed, two independent thresholds exist, one for H_T and one for H_T^{miss}. By making a threshold cut on a scalar sum such as H_T, the removal of jets will simply reduce the overall scalar sum. For a vector sum quantity such as H_T^{miss} however, there are two effects which arise and work against each other:

    (a) The introduction of fake missing energy into a perfectly balanced event (or otherwise) by not considering those jets which balance the event but fall below the threshold.

    (b) The removal of real missing energy by cutting out all jets in an event which lie below the threshold, but do not balance.

5.3 Monte Carlo Generated Samples

5.3.1 Samples Studied

In order to determine the effects of the jet-based configurable parameters, as well as analysing both the performance of the H_T^{miss} versus E_T^{miss} trigger and H_T versus E_T trigger, three types of Monte Carlo generated samples at proton-proton centre-of-mass energy of $\sqrt{s} = 10$ TeV were studied (motivated by the schedule of the LHC at the time):

Table 5.2: Information on the Monte Carlo generated samples used in this study [6] [7].

Sample	Generator	numbers of events $\times 10^6$
SUSY LM0	Pythia	0.2
SUSY LM1	Pythia	0.1
$t\bar{t}$	Madgraph	1.0
QCD (80 GeV $< \hat{p_T} < \infty$)	Pythia	21.0

1. **Supersymmetry** (SUSY). Two R-Parity conserving mSUGRA benchmark parameter points [43], LM0 and LM1, are analysed.

2. $\boldsymbol{t\bar{t}}$ **production in association with jets**.

3. **QCD**.

Full details of the numbers of events and generator used for each of the samples described above are shown in Table 5.2. The samples were run through a full simulation of the CMS detector, where a software emulation of the GCT hardware models the response of the various energy sum triggers. The following sections study the effects described in Section 5.2.1, and how this response varies between the signal samples above, i.e. with both true and fake missing energy content.

5.3.2 Characterising Samples

Before such an analysis is performed, it is helpful to attempt to characterise the samples, with a view to understanding the different responses to jet energy corrections and threshold cuts. The SUSY processes can be characterised by an experimental signature which has a real missing transverse energy, from particles which pass undetected through the CMS detector, along with high transverse-energy jets. The same is true for the $t\bar{t}$+jets process, albeit with a lower transverse energy content. The topology of QCD events is typically back-to-back, and as such the amount of missing energy in these events is close to zero and arises from jet energy mismeasurement in the detector. Semi-leptonic decays from QCD do give rise to real E_T^{miss} however.

Characterising Jet Energy Corrections

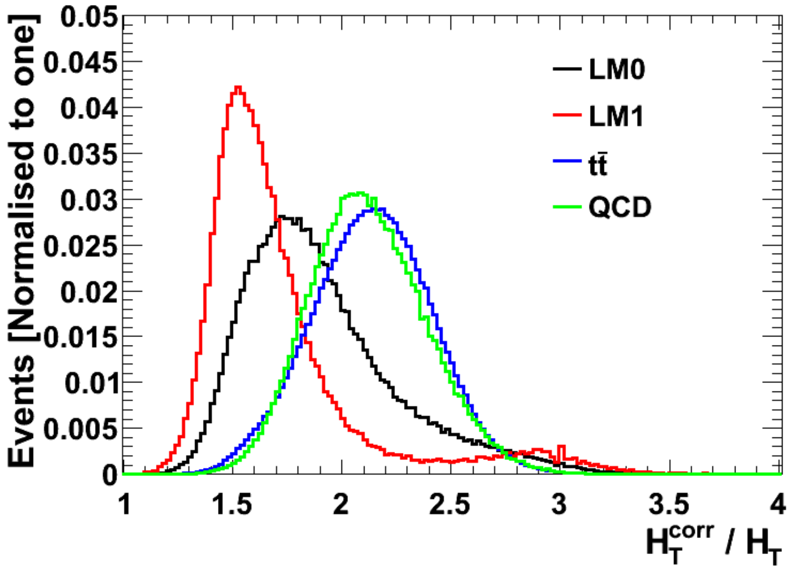

Figure 5.2: $H_T^{\rm corr}/H_T$, with no threshold applied, on an event-by-event basis for the different samples shown.

The effects of applying jet energy corrections are shown in Figure 5.2 for each of the samples. This is done by calculating, with no threshold cuts applied in both cases, the ratio of the sum of all corrected jets found in an event, $H_T^{\rm corr}$, to the sum of all uncorrected jets found in the same event, H_T. Effectively, different samples have different topologies and are affected differently by the (E_T, η) dependent corrections. Whilst it is clear that larger corrections are applied to the lower energy distributions, the shapes of these 'smearing functions' are also important. The LM1 correction is much finer than that of the other samples, which are similar. The tails of the SUSY 'smearing functions' are also longer than the Standard Model samples. This has consequences when constructing cumulative plots before and after applying jet energy corrections, as the shapes of such functions will affect the slope of cumulative plots, whilst the average value of the correction will determine when the cumulative curve inflexes. The correction smearing function for a sample is highly correlated to its initial distribution however, so translating effects relatively between samples is non-trivial.

Characterising Threshold Cuts

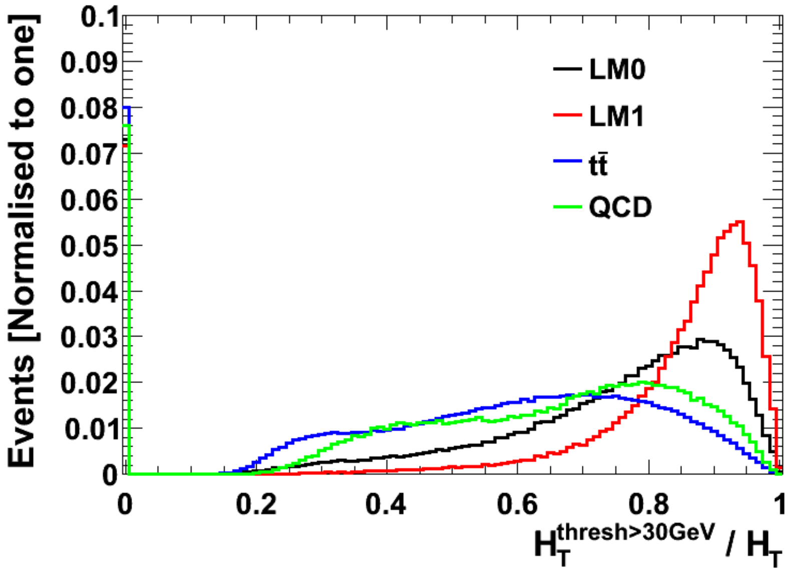

Figure 5.3: $H_T^{\text{thresh}>30\text{ GeV}}/H_T$ on an event-by-event basis for the different samples shown.

In a similar vein to the characterisation of jet energy corrections, Figure 5.3 shows the ratio of uncorrected H_T in an event with a threshold of 30 GeV on jets, $H_T^{\text{thresh}>30\text{ GeV}}$, to H_T. The distributions with the softest jets are affected the most by such a cut, both with the number of events which have no jets above the threshold and hence also no H_T^{miss}, and by the average scaling factor for H_T. The characteristics of these distributions will also affect the cumulative efficiency curves.

Characterising N_{jets} vs H_T

Figure 5.4 shows the correlation between the H_T and the number of jets found in an event, for the different samples at the Level-1 trigger, with no threshold applied to clustered jets. The number of jets found per event affects the sensitivity to jet energy corrections and threshold cuts, since a larger number of jets for some H_T implies a lower energy per jet, and hence both larger corrections and a larger threshold effect. This is especially true for the Standard Model samples, since the correlation between jet multiplicity and H_T for the SUSY samples in Figures 5.4(a) and 5.4(b) shows a

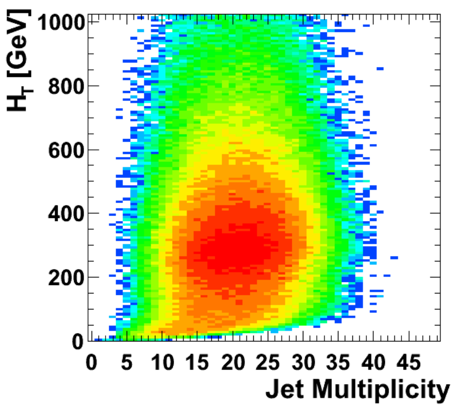

(a) SUSY LM0

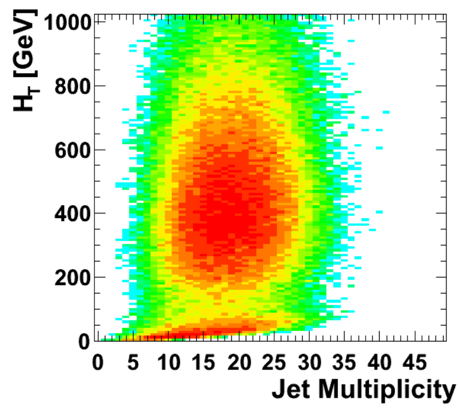

(b) SUSY LM1

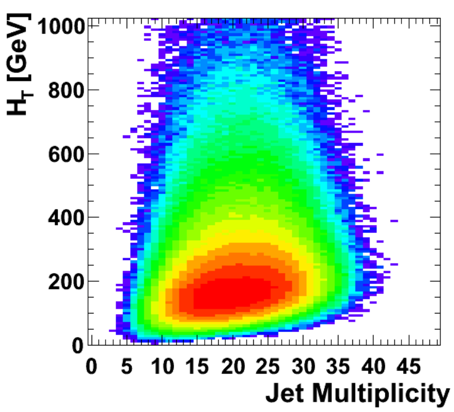

(c) $t\bar{t}$ + jets

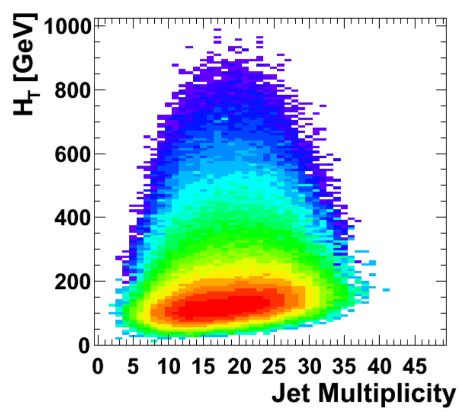

(d) QCD

Figure 5.4: Correlation between H_T and Jet Multiplicity (with no threshold) at the Level-1 trigger for samples of SUSY LM0 (a), SUSY LM1 (b), $t\bar{t}$ (c) and QCD (d).

circular contour, whilst this is more elliptical for the Standard Model $t\bar{t}$ and QCD samples in Figures 5.4(c) and 5.4(d) respectively. The SUSY samples also have a larger transverse energy content than the Standard Model samples, with the LM1 sample also exhibiting a softer component between 0 and 100 GeV, as can be seen in Figure 5.4(b).

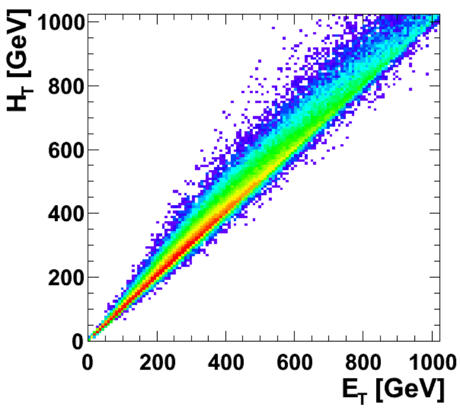

(a) SUSY LM0

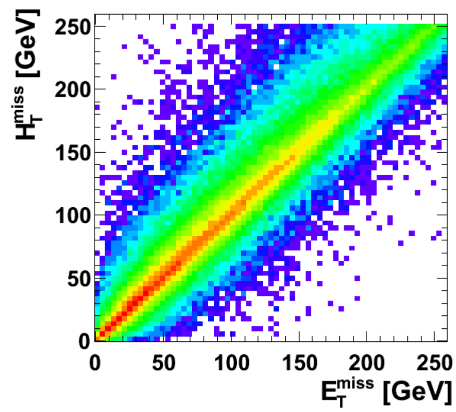

(b) SUSY LM0

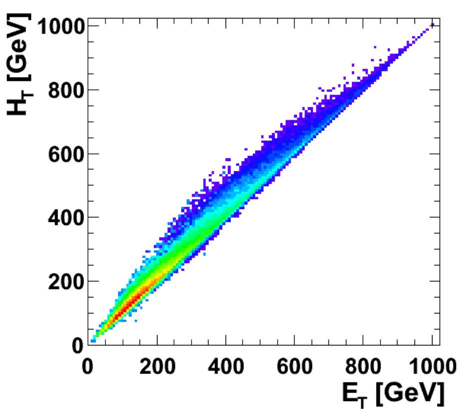

(c) QCD

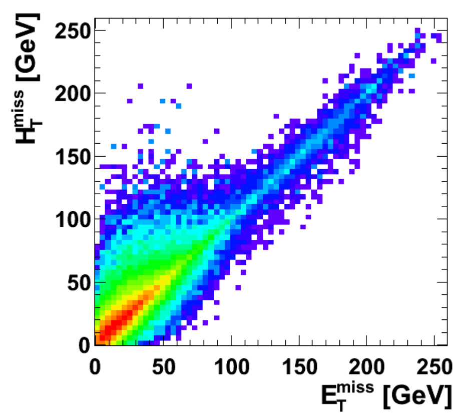

(d) QCD

Figure 5.5: H_T vs E_T correlations for SUSY LM0 (a) and QCD (c). H_T^{miss} vs E_T^{miss} correlations for SUSY LM0 (b) and QCD (d).

Characterising Overlapped Jets

As discussed in Section 4.2.4, the sliding window jet-finding method implemented in the GCT does not prohibit single energy depositions contributing to multiple jets. The extent to which this effect occurs is important when comparing H_T to E_T and H_T^{miss} to E_T^{miss}, and can most easily be characterised by looking at correlation plots of the above quantities. These are shown for both SUSY LM0 and QCD in Figure 5.5, where it is clear that in general, $H_T > E_T$. This effect is larger for

QCD, which implies that there is a corresponding higher rate of overlapping jets. The correlations for the missing energy quantities are broader, mainly due to the fact that clustered jet energies, and not individual region energies, are resolved into components before the vector summation. Again, in general $H_T^{\text{miss}} > E_T^{\text{miss}}$, where the effect is exaggerated for QCD in the region 0 to 100 GeV due to the higher rate of overlapping jets.

5.4 Signal Performance

5.4.1 Characterising Signal Performance

Figures 5.6(a) and 5.6(b) show the cumulative signal efficiency as a function of applied threshold on both total and missing energy quantities respectively for the SUSY LM0 sample, where the sensitivity to the jet configurable parameters discussed in Section 5.2.1 are applied. It can be seen that H_T and E_T perform very similarly, H_T having a slightly better efficiency, approximately 2% at 400 GeV, mainly due to the effect causing $H_T > E_T$ as previously described. The same plots for a QCD sample are shown in Figures 5.7(a) and 5.7(b) respectively. The difference in cumulative efficiency between H_T and E_T in this case is approximately 5% at 150 GeV, which can be attributed to the higher rate of overlapping jets in QCD, as discussed in Section 5.3.2. Similarly, H_T^{miss} performs better than E_T^{miss} by approximately 2% at 100 GeV for SUSY LM0, but 4% at 30 GeV for QCD for the same reasons. Recall that due to hardware bandwidth constraints on the available precision of H_T^{miss} only the range 0-256 GeV is considered.

The effect of applying a 30 GeV threshold cut on jets contributing to the H_T scalar sum reduce the total energy content, and hence the efficiency for both samples. This effect when compared to E_T is approximately 7% at 400 GeV for uncorrected jets in SUSY LM0, whilst approximately 20% at 150 GeV in QCD. The effect is larger for QCD due to the larger fraction of jets which are below the threshold, e.g. as shown by the first bin in Figure 5.3. By applying such a cut, an edge on this threshold is introduced – as it is not possible to create a scalar sum smaller than the threshold

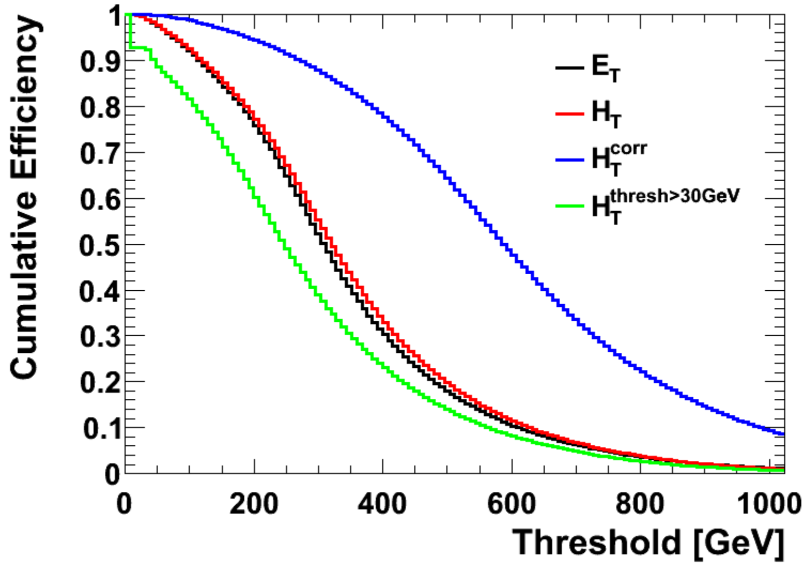

(a)

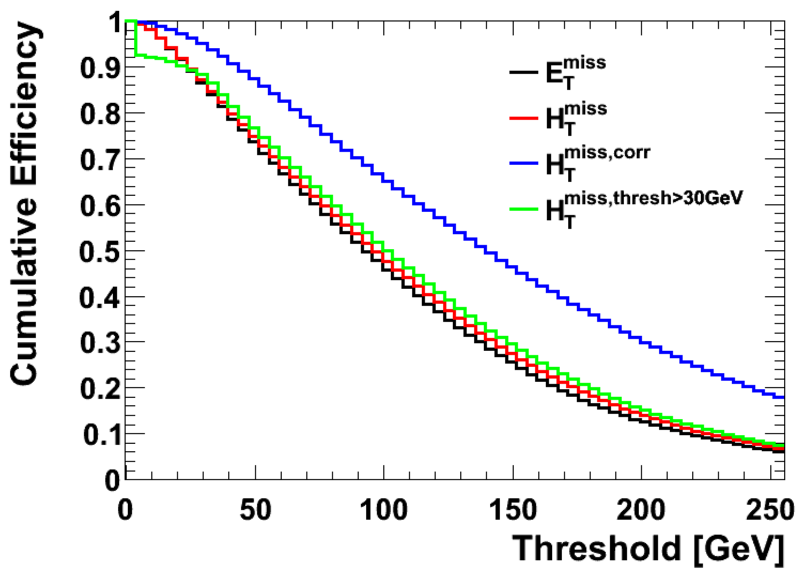

(b)

Figure 5.6: Cumulative efficiency distribution plots of a SUSY LM0 Monte Carlo generated sample for various (a) E_T-type quantities, (b) E_T^{miss}-type quantities.

using a jet larger than the threshold – increasing the number of events with zero H_T, which is mirrored by the plateau in the cumulative plots. The opposing effects

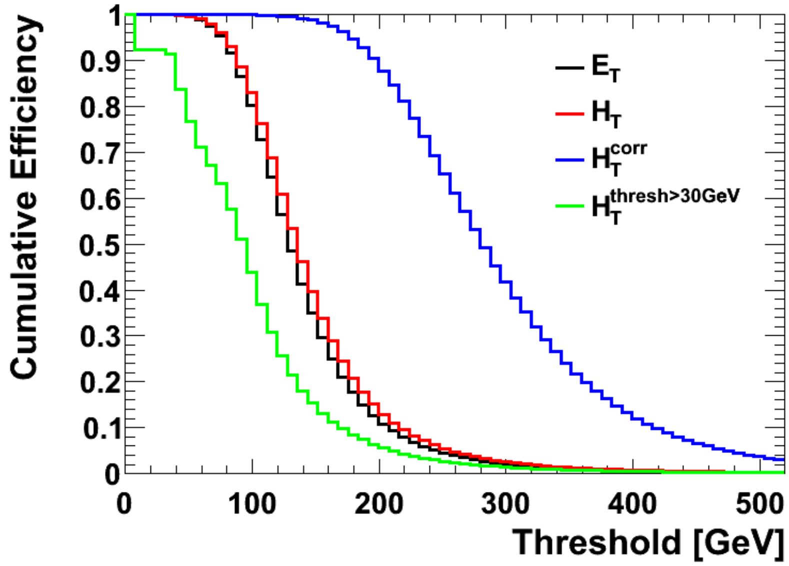

(a)

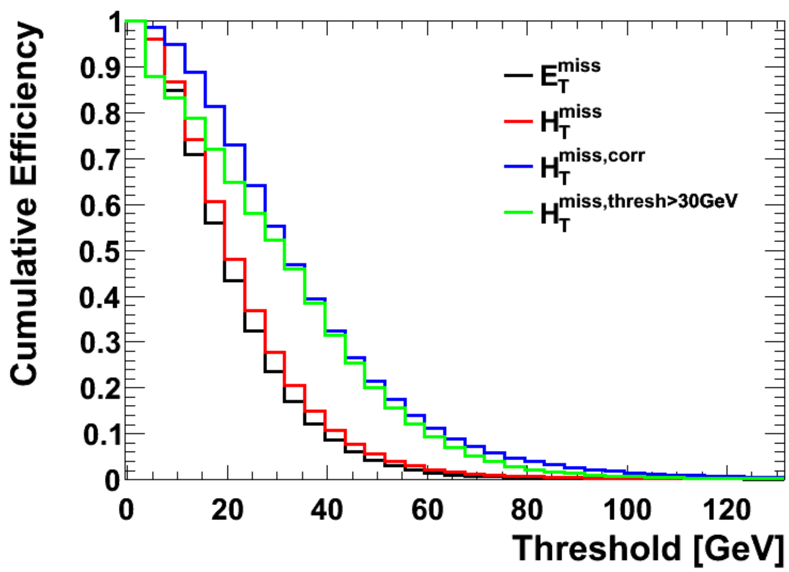

(b)

Figure 5.7: Cumulative efficiency distribution plots of a QCD Monte Carlo generated sample for various (a) E_T-type quantities (b) E_T^{miss}-type quantities.

of a threshold cut for H_T^{miss} as described in Section 5.2.1 are seen by the fact the cumulative signal efficiency relative to E_T^{miss} is lower in the region of the threshold cut i.e. 0-30 GeV, but larger beyond that, due to the introduction of fake missing energy. For the SUSY LM0 sample this difference in efficiency is approximately 2% at 100 GeV, whilst for the QCD sample, this number is approximately 20% at 30 GeV, again due to the higher number of jets which are not above the 30 GeV threshold in such a sample, which increases the H_T^{miss} content.

Similar curves are seen after jet energy corrections have been applied which increase the energy of each jet. The original distributions are convoluted with the curves shown in Figure 5.2 which has the overall effect of the cumulative efficiency curves falling both later and slower. For H_T^{corr} relative to E_T, a fixed efficiency of 50% for a SUSY LM0 sample occurs at 590 GeV corrected to 300 GeV uncorrected, whilst the same efficiency for QCD occurs at 280 GeV corrected to 130 GeV uncorrected. The convolution of the vector sum reduces the overall sensitivity for the comparison between H_T^{miss} and E_T^{miss}. A similar analysis for the SUSY LM1 and $t\bar{t}$ samples yield similar results conceptually, however the differences in sensitivity to the effects described relative to the QCD sample are now discussed.

5.4.2 Comparing Signal Performance

The combined effects of the various parameters on both the QCD and SUSY LM0 samples for E_T-type and E_T^{miss}-type quantities are shown in Figures 5.8(a) and 5.8(b) respectively. The various curves in the region of interest for the total energy quantities show that E_T and H_T perform within 1% across the range. The effect of making a 30 GeV threshold jet cut on H_T are more pronounced for LM0 signal efficiency however. For example for a fixed SUSY LM0 efficiency of 80%, the QCD 'rate' doubles to 36% relative to E_T. However the opposite is seen when applying jet energy corrections, which reduces the QCD 'rate' by 2% for the same SUSY LM0 signal efficiency of 80%. Similar results are obtained for the missing energy quantities E_T^{miss} and H_T^{miss}, however the convolution of the missing energy sum calculations reduces the agreement to $< 5\%$ across the range.

A similar analysis applied to a $t\bar{t}$ + jets sample is shown in Figure 5.9. Overall, the $t\bar{t}$ + jets sample has a lower signal efficiency for the same QCD rate relative to the

SUSY LM0 sample. This is primarily because of the lower energy jet distribution, which make the $t\bar{t}$ + jets and QCD distributions more alike. The sensitivity to the various parameters for the E_T-type distributions is the same as for the SUSY LM0 sample. However, the performance of the E_T^{miss} and H_T^{miss} triggers differ slightly at high $t\bar{t}$ signal efficiency, with the H_T^{miss} trigger with 30 GeV jet threshold performing within 5% of the H_T^{miss} trigger with no threshold applied.

The analysis using the LM1 benchmark point is shown in Figure 5.10. The major difference in the results can be attributed to the much harder jets, and hence resulting higher energy content, which changes the behaviour of the smearing functions in Figures 5.2 and 5.3 to a greater extent relative to QCD. This results in H_T^{corr} performing worse than E_T by e.g. 6% at a SUSY LM1 signal efficiency of 85%. This effect is smaller for $H_T^{\text{miss,corr}}$ relative to E_T^{miss}, at about 2%.

5.4.3 Characterising Detector Noise

In the absence of beam, CMS participated in many global cosmic-ray muon runs, such as those described in Section 4.4, in which the magnetic field was turned on and data taken was triggered primarily by cosmic-ray muons. However, such runs also included triggers from detector noise, in particular from the HCAL. The leading and second leading jet-E_T distributions are shown in Figure 5.11 from one such run triggered in this way. The maximum jet multiplicity for this run was five, with only one non-zero jet typically reconstructed offline per event. The distributions shown motivate values for a threshold cut on the H_T and H_T^{miss} triggers, ranging from 10 GeV to the 30 GeV threshold used in this study, which would largely suppress such backgrounds.

5.5 Conclusions

In general, with no thresholds or corrections applied to jets found at the Level-1 trigger, the performance of the jet-based and calorimeter-based energy sum triggers are very similar, with E_T and E_T^{miss} generally having a higher signal efficiency versus

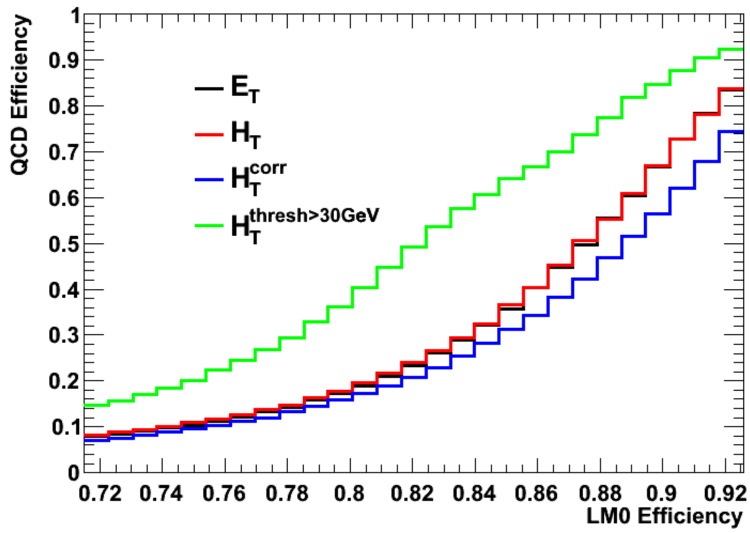

(a)

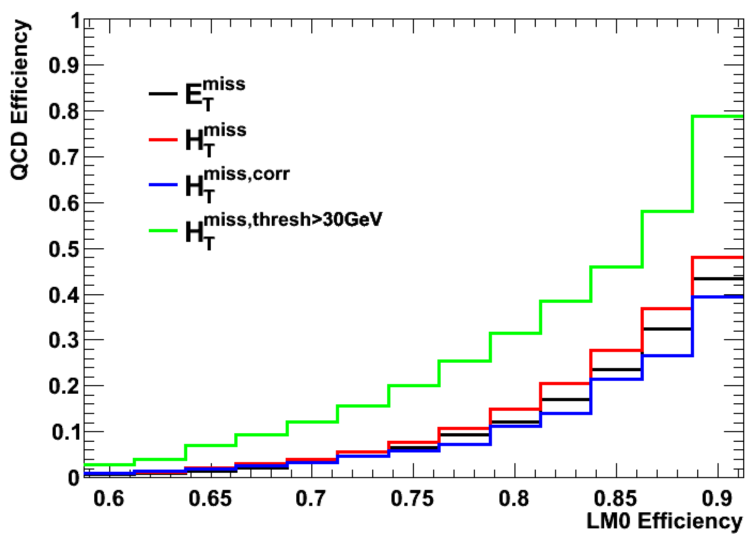

(b)

Figure 5.8: SUSY LM0 signal efficiency vs QCD efficiency plots for various (a) E_T-type quantities (b) E_T^{miss}-type quantities.

QCD rate for the signal samples analysed, more so for E_T^{miss}. This is primarily due to the jet-finding method implemented in the GCT. The application of thresholds

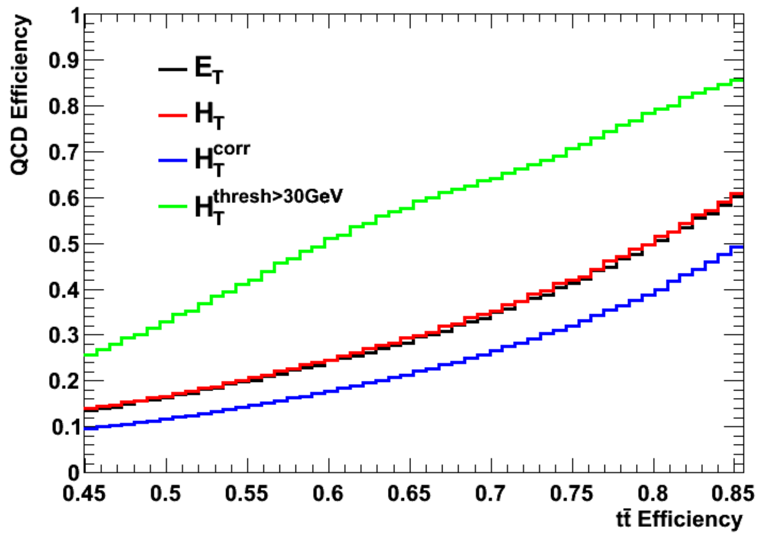

(a)

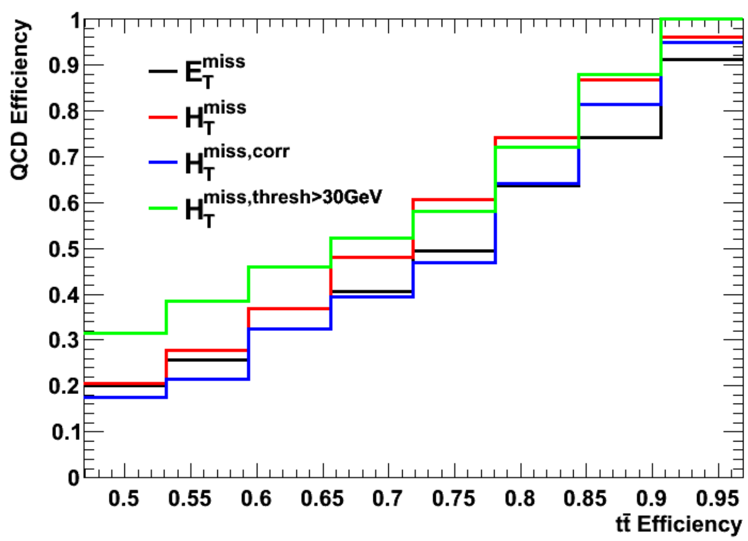

(b)

Figure 5.9: $t\bar{t}$ + jets signal efficiency vs QCD efficiency plots for various (a) E_T-type quantities (b) E_T^{miss}-type quantities.

and corrections to jets provides additional flexibility. Whilst imposing threshold cuts on both H_T and H_T^{miss} generally increases the QCD rate for a fixed signal

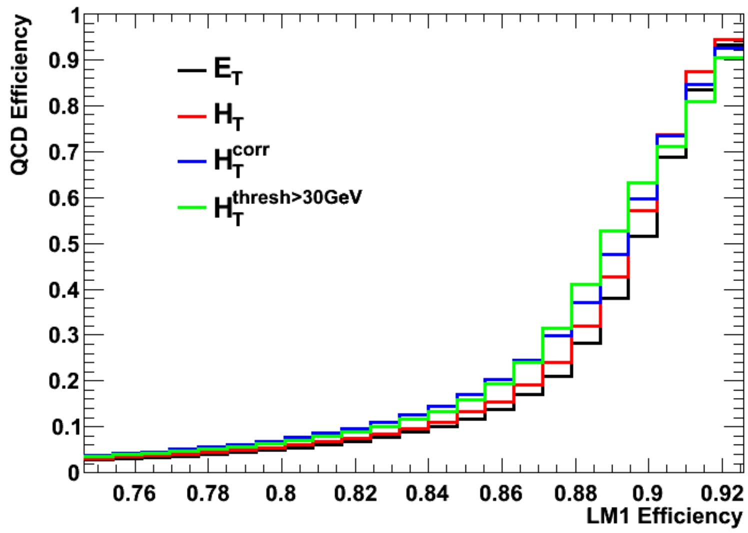

(a)

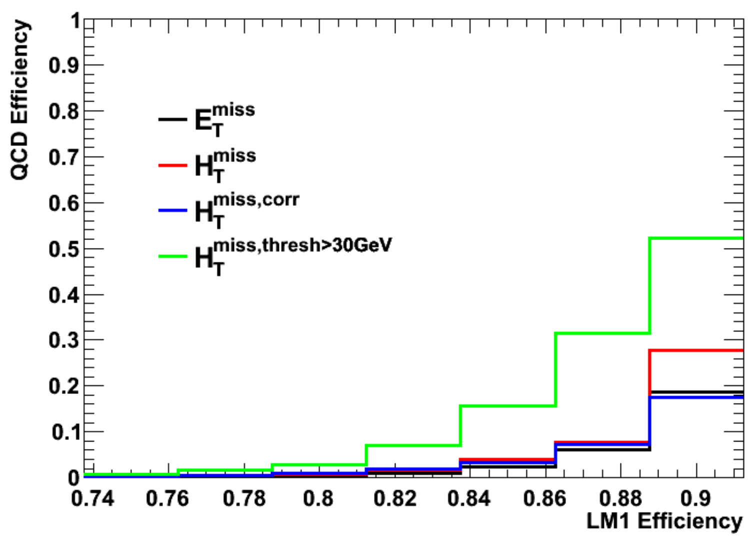

(b)

Figure 5.10: SUSY LM1 signal efficiency vs QCD efficiency plots for various (a) E_T-type quantities (b) E_T^{miss}-type quantities.

efficiency relative to E_T and E_T^{miss} respectively, basic characterisation of detector noise shows that such parameters are useful in reducing the noise rate. When

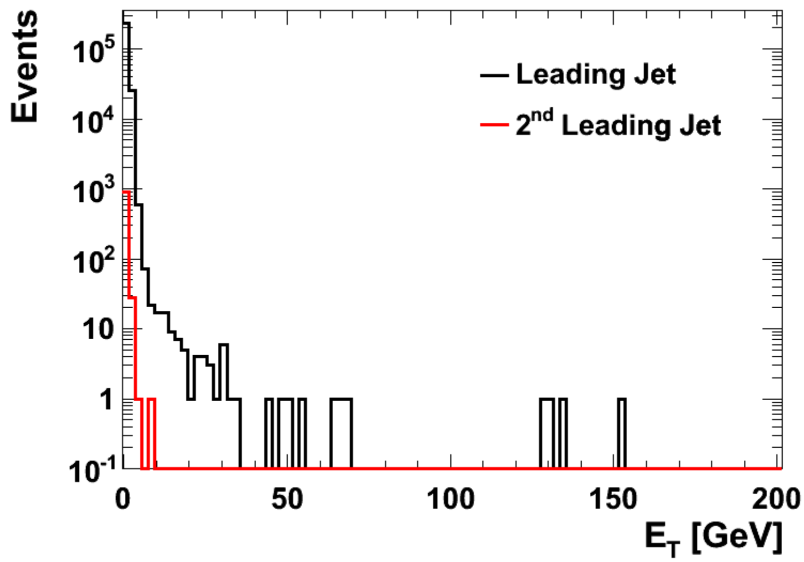

Figure 5.11: The leading, and second leading, jet-E_T distributions, as part of a run triggered on HCAL noise in the CMS detector.

jet energy corrections are applied, the performance of H_T and $H_T^{\rm miss}$ are generally improved so that they are more efficient than the E_T and $E_T^{\rm miss}$ triggers respectively. This effect is smaller for $H_T^{\rm miss}$ due to the convolution from the vector sum. There are cases however, where jet energy corrections can reduce signal efficiency, and this is shown for $H_T^{\rm corr}$ with the SUSY LM1 sample, which has a hard jet spectrum and a correspondingly sharp correction function.

In summary, jet-based energy sum triggers are complementary to the calorimeter-based triggers, and the configurable parameters discussed provide flexibility to adapt to the beam and detector conditions experienced.

Chapter 6

Utilising W Boson Polarisation

As motivated in Section 2.4, W bosons at the LHC are expected to exhibit a large transverse polarisation at high-P_T, which will predominantly affect the angular distribution of the decay products in the chosen frame of reference (the helicity frame in this case). Such an effect, when combined with charge asymmetry arguments, can be used as a tool in the search for New Physics.

6.1 Generator-Level Expectations

In order to test both the parameterisation of Equations (2.7) and (2.8), and the expectations discussed in Chapter 2, the MADGRAPH [6] Monte Carlo generator, interfaced to PYTHIA [7] was used to produce approximately ten million W+jets events and 1.2 million Z+jets events, at a proton-proton centre of mass energy of $\sqrt{s}$ = 7 TeV. The CTEQ6L1 set [47] from the LHAPDF package [48] of parton distribution functions were adopted.

The generator-level $\cos(\theta^*)$ distributions of the positively charged lepton in three bins of P_T(boson), for both W and Z bosons are shown in Figure 6.1 (see Chapter 2 for reminder of definitions). The results of fitting these distributions to the analytical form in Equation 2.7 are listed in Table 6.1. As expected, f_L is dominant for the W, and increases with $P_T(W)$. The f_L dependence can be seen from the $(1-\cos(\theta^*))^2$

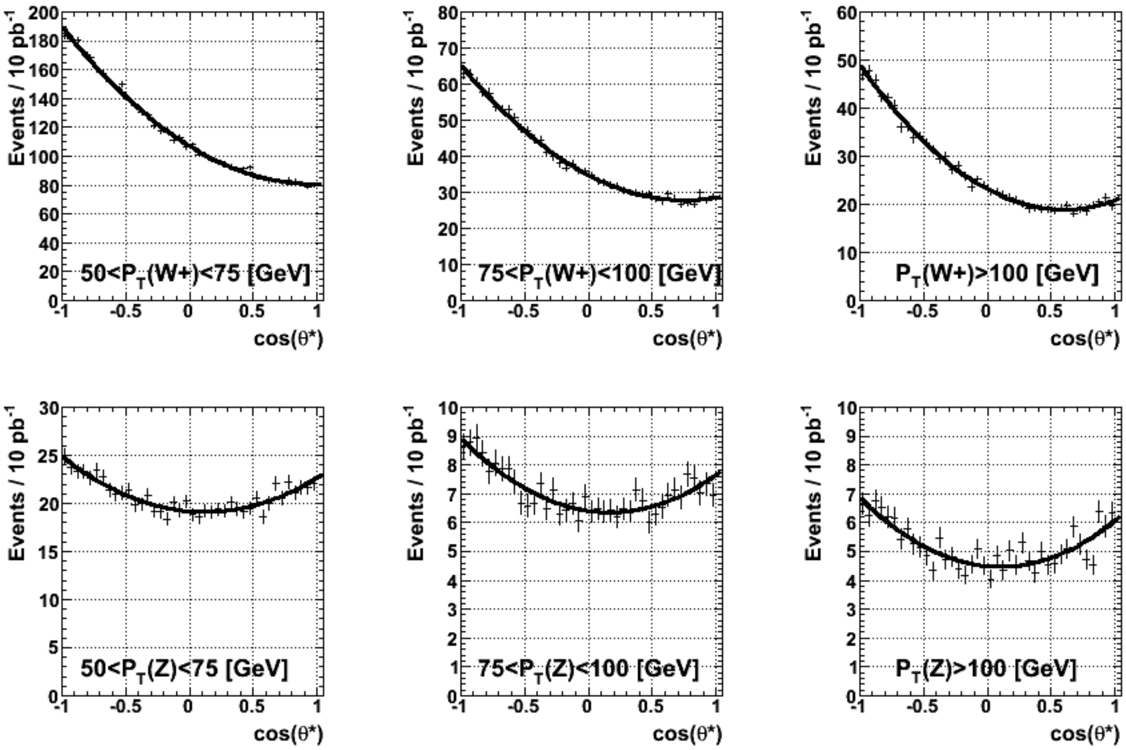

Figure 6.1: The $\cos\theta^*$ distribution from the positively charged lepton shown in bins of P_T(boson) for the W (top) and the Z (bottom). The expected yield for 10pb^{-1} is shown along with the analytical fit to Equation 2.7. The error bars shown are as a result of the number of events in the Monte Carlo sample. ($\sqrt{s} = 7$ TeV)

dominance of the $\cos(\theta^*)$ distribution, which is thus predominantly valued at -1 i.e. most of the energy from the decay goes to the left-handed particle, which is the neutrino in this case. A similar plot for the negatively charged lepton (not shown) has the $\cos(\theta^*)$ distribution predominantly valued at $+1$, which again implies that most of the energy from the decay goes to the left-handed particle, which is the charged lepton in that case. For the Z, a flatter distribution is expected, as the relationship between V_i and f_i is not the unity matrix and hence values of $\cos(\theta^*)$ at ± 1 are similar ($c_L^2/c_R^2 = 1.36$, see Section 2.4). Table 6.1 also lists the values of V_i for the Z-boson, which are obtained via the relation in Equation 2.11. This illustrates the fact that the Z boson is also predominantly left-handed as discussed, and makes studies of both bosons complementary in determining the A_i coefficients.

The evolution of the A_i parameters for $W^{\pm}$ bosons are shown as a function of $P_T(W)$ in the helicity frame in Figure 6.2. As expected, with increasing $P_T(W)$, the degree

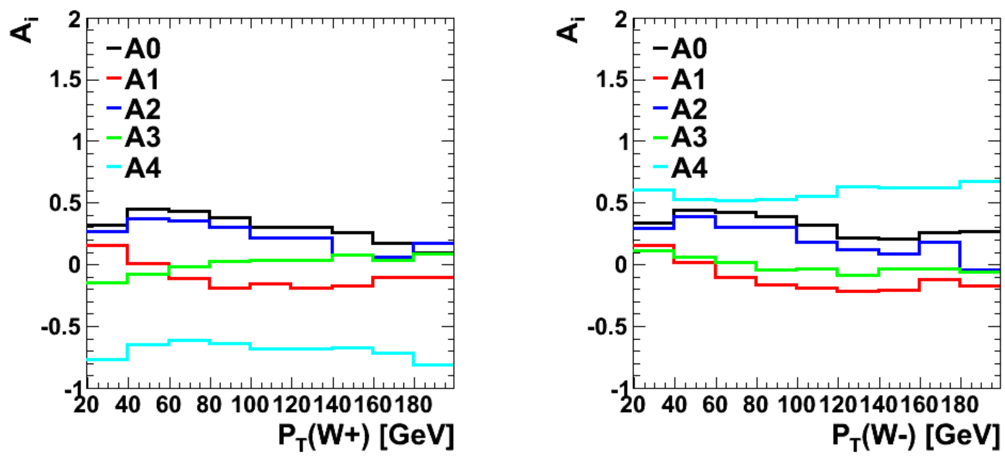

Figure 6.2: The coefficients of Equation (2.9) calculated in the helicity frame for $W^{\pm}$ bosons as a function of $P_T(W)$. The scatter of the points is due to the limited number of events in each bin, which fall with increasing $P_T(W)$. ($\sqrt{s} = 7$ TeV)

of freedom associated with the mass of the boson tends to zero, and hence so does the longitudinal component $f_0 \sim A_0$, whilst the value of $A_4 \sim \pm(f_L - f_R)$ stays approximately constant.

Table 6.1: Helicity parameters of the W and Z bosons for three different P_T(boson) [GeV] bins. ($\sqrt{s} = 7$ TeV)

	boson:lepton charge	$50 < P_T(V) < 75$	$75 < P_T(V) < 100$	$P_T(V) > 100$
$V_L = f_L$	$W : +$	0.544 ± 0.002	0.561 ± 0.004	0.605 ± 0.005
$V_R = f_R$	$W : +$	0.231 ± 0.002	0.245 ± 0.003	0.257 ± 0.004
$V_L = f_L$	$W : -$	0.519 ± 0.003	0.530 ± 0.005	0.582 ± 0.005
$V_R = f_R$	$W : -$	0.263 ± 0.002	0.268 ± 0.004	0.284 ± 0.005
f_L	$Z : +$	0.400 ± 0.005	0.424 ± 0.009	0.445 ± 0.011
f_R	$Z : +$	0.366 ± 0.005	0.363 ± 0.009	0.397 ± 0.010
V_L	$Z : +$	0.496 ± 0.021	0.598 ± 0.037	0.579 ± 0.043
V_R	$Z : +$	0.270 ± 0.021	0.189 ± 0.036	0.263 ± 0.043

A similar generator level study for W bosons only was also performed using ALPGEN interfaced to PYTHIA, with the same parton distribution functions as above. Six million events were generated, in bins of $P_T(W)$ and jet multiplicity, however this time at $\sqrt{s} = 10$ TeV (dictated by the LHC schedule at the time). The high-P_T region $P_T(W) > 100$ GeV is considered exclusively. Figure 6.3 shows the $P_T(W)$

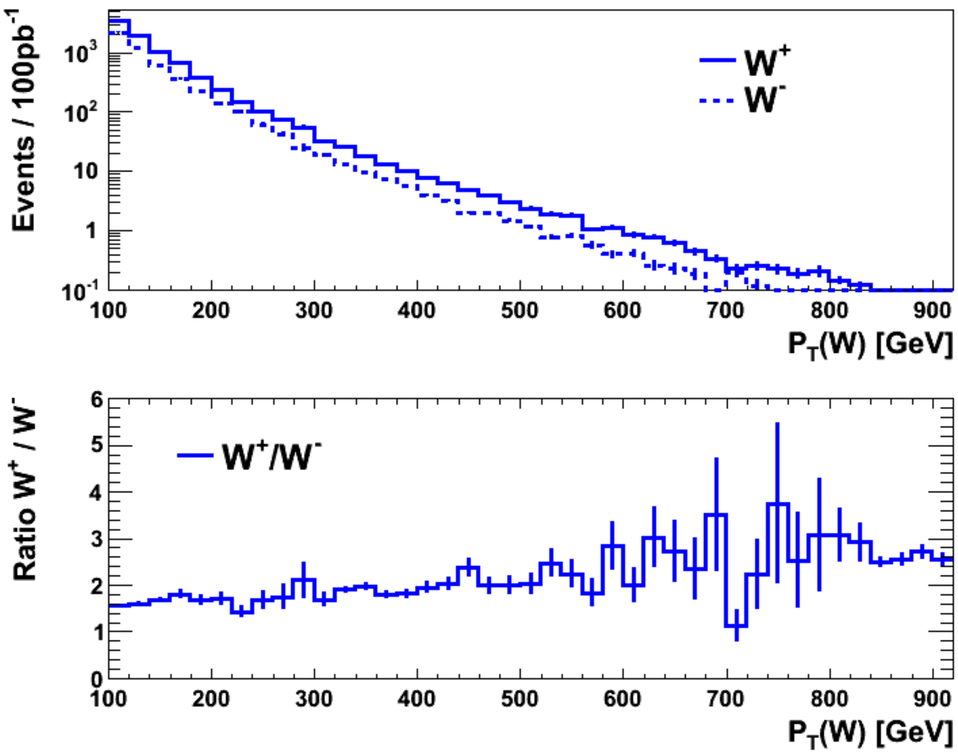

Figure 6.3: The $W^{\pm}$ boson transverse momentum distributions, and their ratio. ($\sqrt{s} = 10$ TeV)

distributions for the different W boson charges and their ratios. The ratio $\frac{W^+}{W^-}$ is slightly below two for W bosons with a transverse momentum of about 100 GeV and increases with increasing $P_T(W)$, to values above two. This relationship is attributed to the dominance of the valence quark participation in the production of W bosons, i.e. the probability of finding a valence u quark with increasingly larger values of x_{bjorken} is progressively larger than for a valence d quark of the same momentum (see Figure 2.2).

The dependence of the $W^{\pm}$ boson helicity on the boson's $P_T(W)$, rapidity ($|Y(W)|$), and jet multiplicity, are shown in Figures 6.4, 6.5 and 6.6 respectively. The behaviour for both W boson charges is the same within the statistical errors of the Monte Carlo sample, as expected from discussions in Chapter 2. The $|Y(W)|$ dependence is the most dominant effect and clearly shows an increase in the left-handed component, and a decrease in the right-handed component, for an increase in $|Y(W)|$ i.e. in the more forward region. The $P_T(W)$ dependence also shows an overall increase in the left-handed component, in agreement with Figure 2.9 of Section 2.4. The dependence

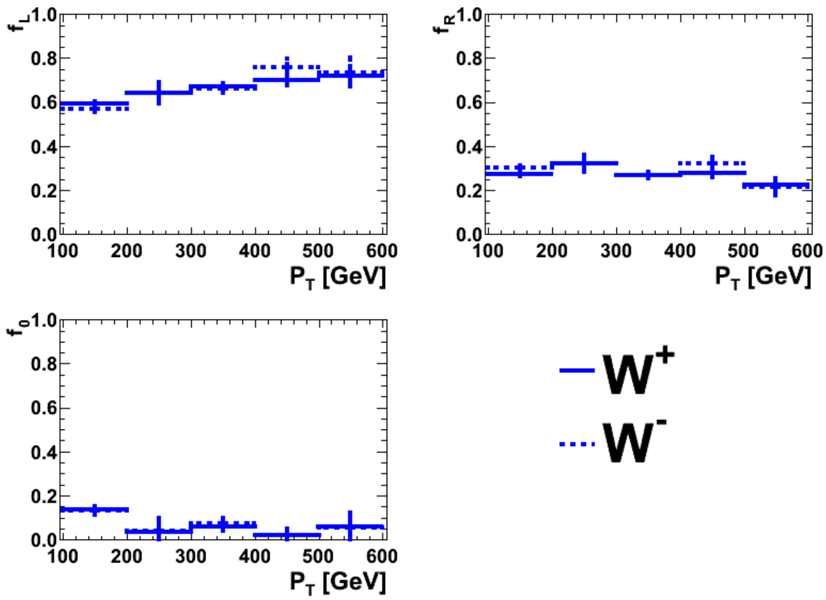

Figure 6.4: The $P_T(W)$ dependence of W boson helicity. ($\sqrt{s} = 10$ TeV)

on the jet multiplicity, defined by the number of partons with more than 30 GeV of transverse momentum, is very small. However there seems to be a trend that for the larger jet multiplicities the right-handed helicity is slightly decreased.

6.2 Event kinematics and lepton acceptance

To gauge how polarisation effects are manifested in detector observables, the charged lepton and neutrino P_T distributions from $W^{\pm}$ decays at the generator level are shown in Figures 6.7 and 6.8 respectively, along with their ratios, in the same $P_T(W) > 100$ GeV region. Equivalent distributions were first shown in [49], where the same effects are observed. Due to the predominant left-handedness of both W^+ and W^- bosons, the 100 GeV cut on $P_T(W)$ leads to a peak at around 100 GeV for the negatively charged leptons, whilst the positively charged leptons peak closer to 0 GeV. Beyond 100 GeV, the distributions are approximately similar. Overall however, this means that negatively charged leptons will have a much higher average P_T than positively charged leptons, and hence are affected differently by e.g. a detector-like requirement of $P_T > 10$ GeV on the corresponding charged lepton.

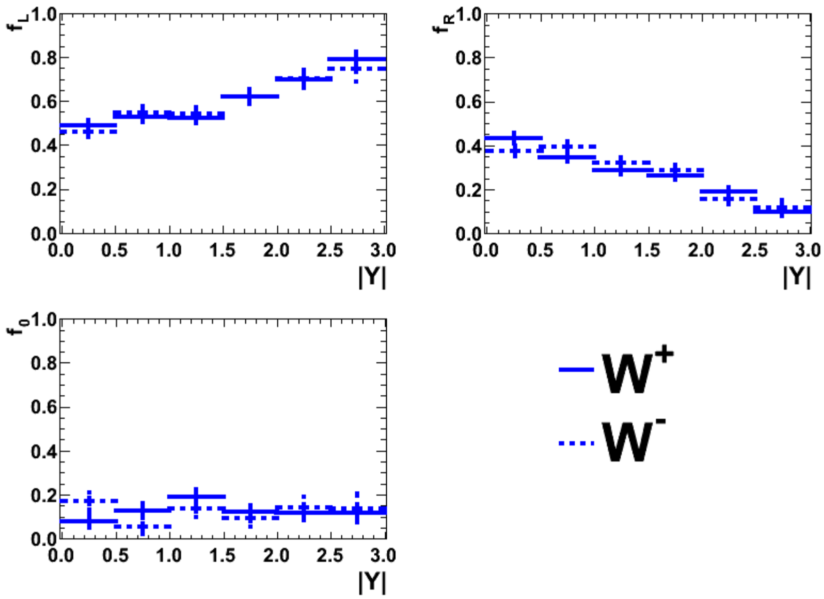

Figure 6.5: The rapidity dependence of W boson helicity. ($\sqrt{s} = 10$ TeV, $P_T(W) > 100$ GeV)

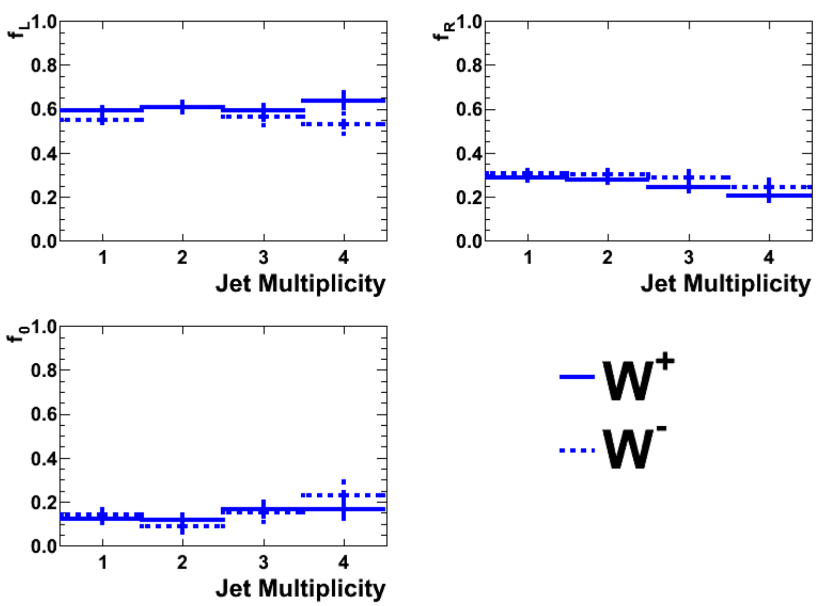

Figure 6.6: The jet multiplicity dependence of W boson helicity. ($\sqrt{s} = 10$ TeV, $P_T(W) > 100$ GeV)

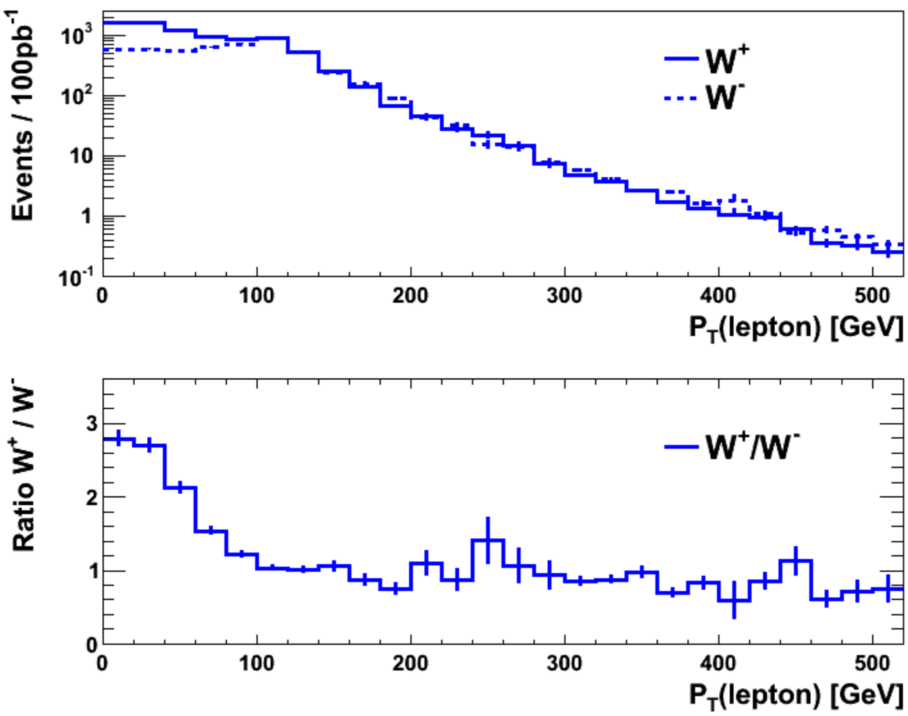

Figure 6.7: The charged lepton P_T distributions from both W^+ and W^- decays, and their ratio. ($\sqrt{s} = 10$ TeV, $P_T(W) > 100$ GeV)

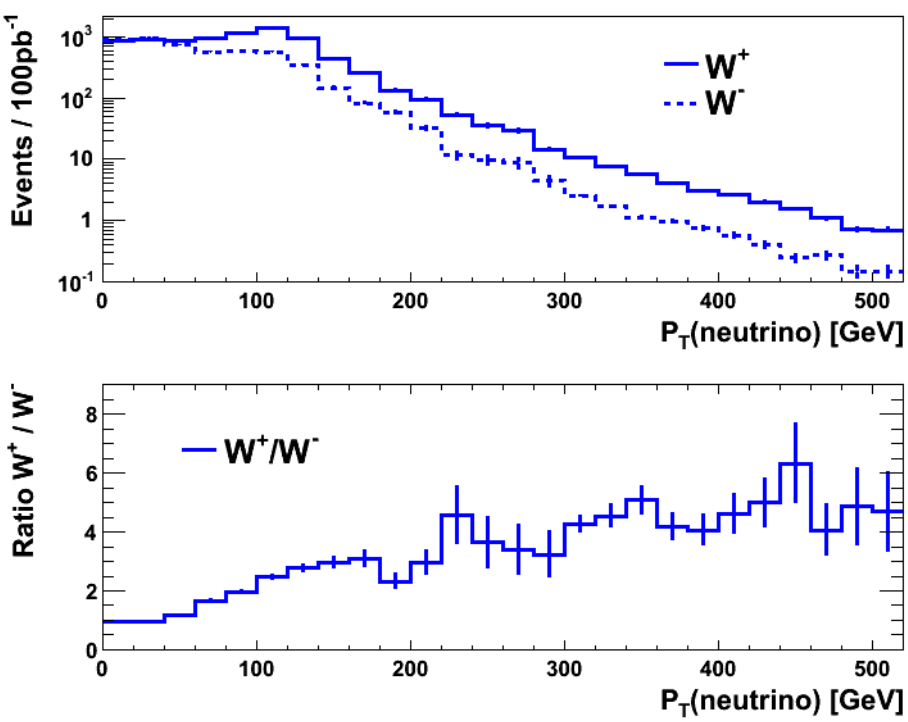

Figure 6.8: The neutrino P_T distributions from both W^+ and W^- decays, and their ratio. ($\sqrt{s} = 10$ TeV, $P_T(W) > 100$ GeV)

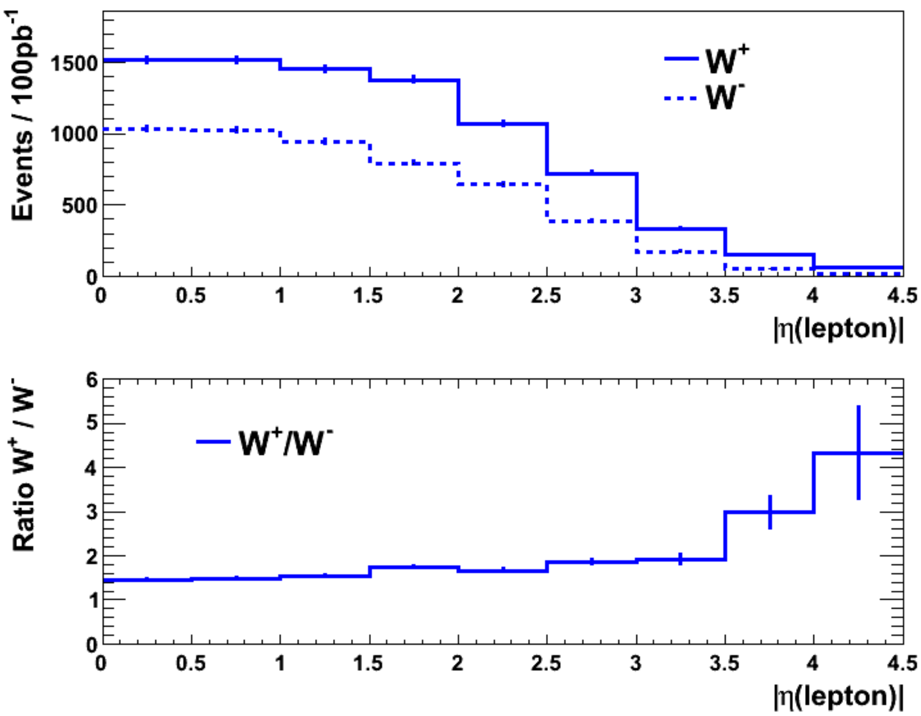

Figure 6.9: The charged lepton $|\eta|$ distributions from both W^+ and W^- decays, and their ratio. ($\sqrt{s} = 10$ TeV, $P_T(W) > 100$ GeV)

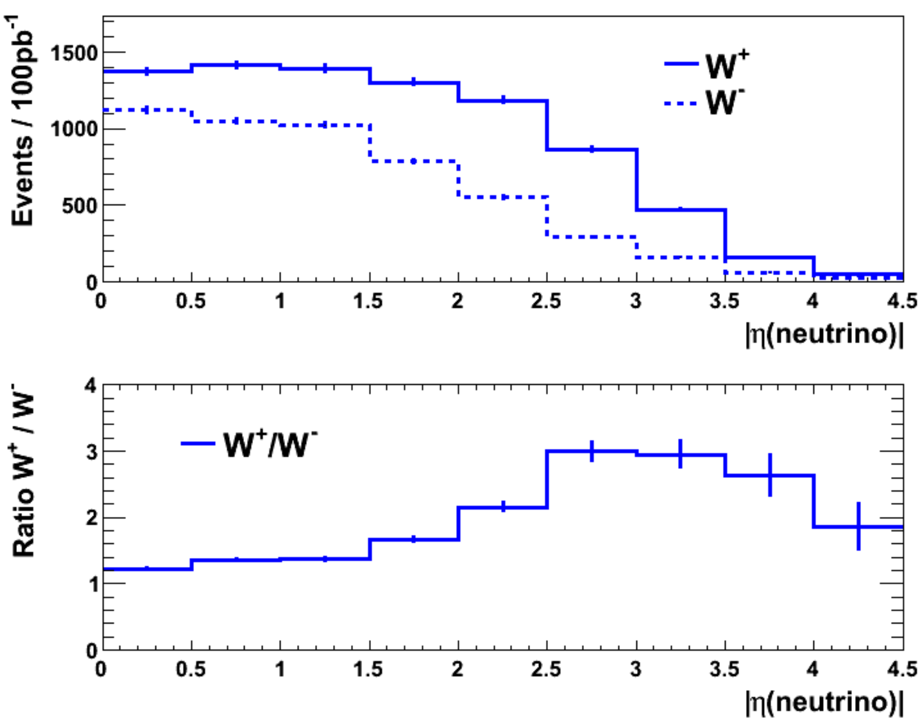

Figure 6.10: The neutrino $|\eta|$ distributions from both W^+ and W^- decays, and their ratio. ($\sqrt{s} = 10$ TeV, $P_T(W) > 100$ GeV)

Given that neutrinos, which represent the missing transverse energy in the detector, arise from the same $W^{\pm}$ decays, the converse is true. If such an $E_T^{\rm miss}$ requirement is utilised in a search for New Physics along with one lepton, the W boson contribution will contain more positively charged leptons than negatively charged ones. This can be seen from Figure 6.8, where the transverse momentum of the neutrinos is shown for both W boson charges. This effect not only stems from the fact that more W^+ than W^- bosons are produced, but also from polarisation i.e. the fact that the neutrinos from W^+ decays carry a larger fraction of the W momentum than neutrinos from W^- decays.

The charged lepton and neutrino pseudo-rapidity (η) distributions for both W boson charges are shown in Figures 6.9 and 6.10 respectively. The charged leptons have a similar η shape at values below the acceptance of the CMS detector ($|\eta| < 2.1$ to 2.4 for muons, see Section 3.2.4), whereas whilst the neutrino η distributions exhibit a larger difference between the charges, they cannot be reconstructed from available detector information.

Figure 6.11 shows the transverse momentum distributions and their ratio for neutrinos from W^+ decays, before and after a detector-like requirement of $P_T > 10$ GeV and $|\eta| < 2.1$ on the corresponding charged lepton. The spectrum after such requirements is largely affected in the region between $100 - 300$ GeV, but becomes increasingly similar in amplitude with increasing P_T(neutrino) with the original. For the anti-neutrinos from W^- decays shown in Figure 6.12, the effect is much less pronounced. This is due to the predominant left-handed helicity of the W boson, which preferentially gives most of its momentum to the negatively charged lepton, hence reducing the impact of such detector-like requirements. In summary, applying such detector-like requirements affects the neutrino P_T distribution from W^+ decays to a greater extent than from W^- decays, which leads to more events from W^+ decays contributing to e.g. an all-hadronic (0-lepton) search for New Physics.

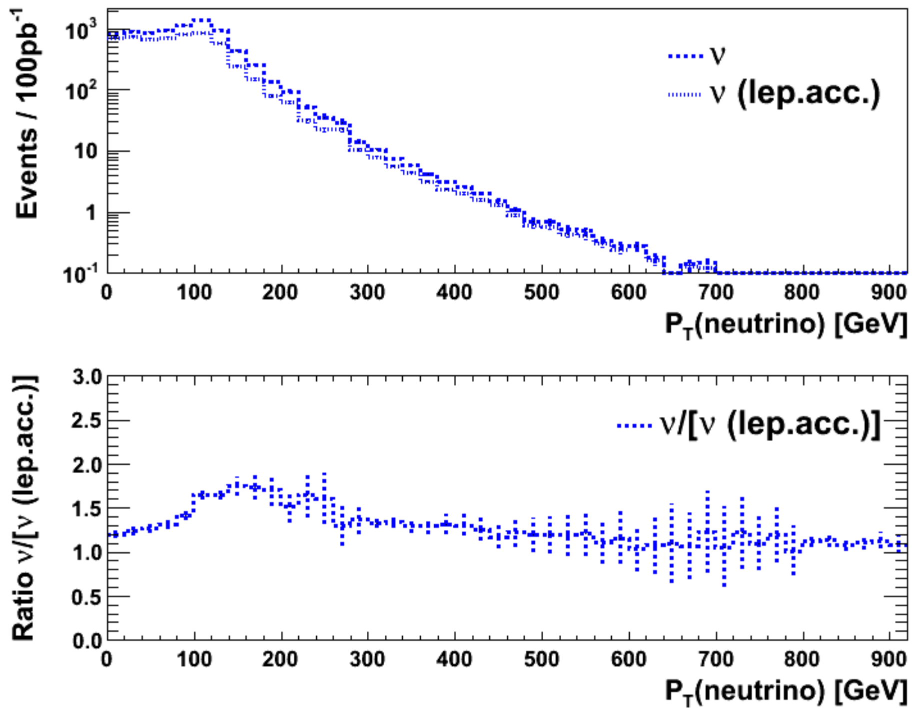

Figure 6.11: The P_T distributions, and their ratio, of neutrinos from W^+ decays before and after a detector-like requirement on the charged lepton, of $P_T > 10$ GeV and $|\eta| < 2.1$. ($\sqrt{s} = 10$ TeV, $P_T(W) > 100$ GeV)

6.3 The Lepton Projection Variable

6.3.1 Introduction

Whilst studies of the W boson probe the differences between left-handed and right-handed production more clearly than the Z boson, it is not possible to unambiguously reconstruct the W boson four-vector from detector-level information. The neutrino from the W decay introduces a two-fold ambiguity on the momentum of the W along the beam axis, $\vec{p}_z(W)$, which in turn affects the boost to the boson rest frame. There are thus three alternatives:

1. Select one of the two solutions in p_z, e.g. the one with the smallest $|\vec{p}_z|$, and then correct for the presence of wrongly-selected solutions,

2. Use both solutions in p_z, weighting each solution with information from the Monte Carlo,

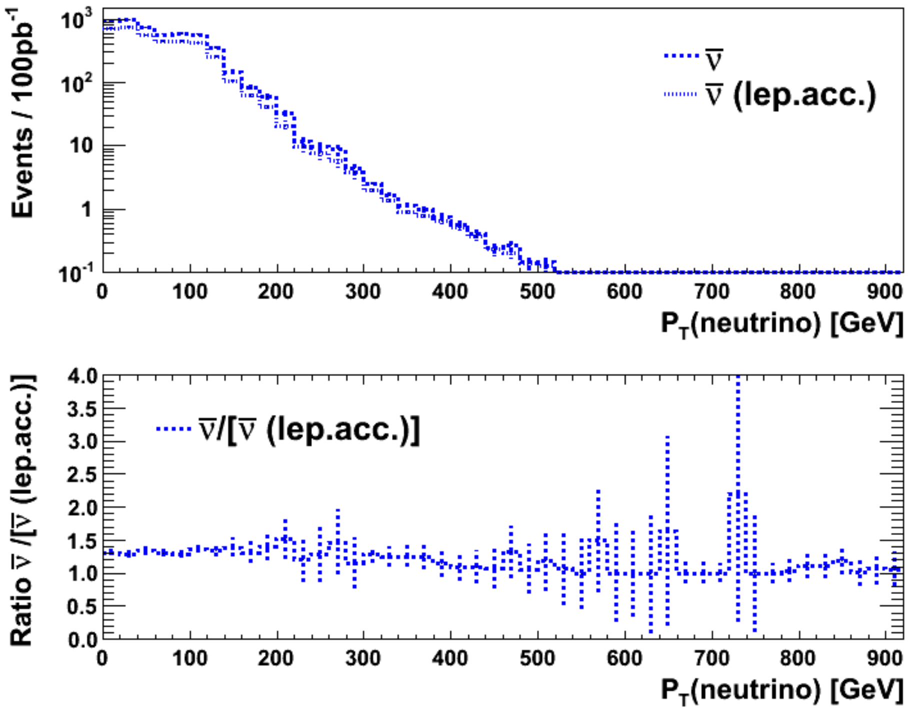

Figure 6.12: The P_T distributions, and their ratio, of anti-neutrinos from W^- decays before and after a detector-like requirement on the charged lepton, of $P_T > 10$ GeV and $|\eta| < 2.1$. ($\sqrt{s} = 10$ TeV, $P_T(W) > 100$ GeV)

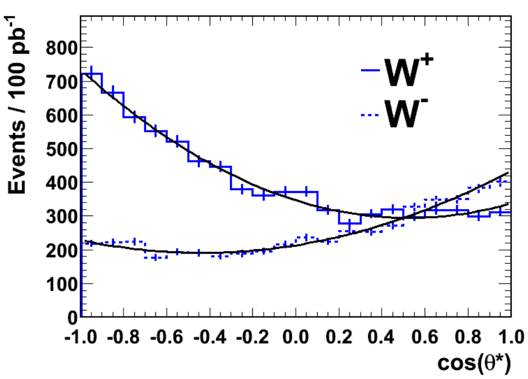

(a) The $\cos(\theta^*)$ distribution

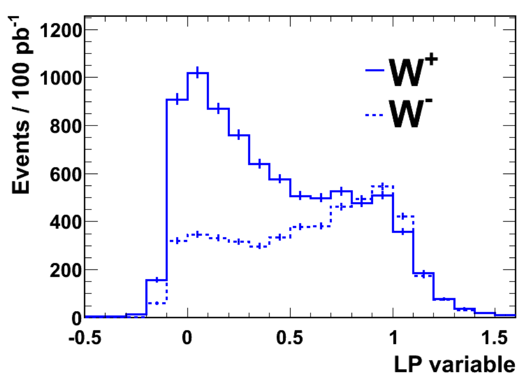

(b) The LP variable distribution.

Figure 6.13: The $\cos(\theta^*)$ (a) and LP variable (b) distributions for charged leptons from $W^\pm$ decays. The fitted functions in (a) are from equations 2.7 and 2.8 ($\sqrt{s} = 10$ TeV, $P_T(W) >$ 100 GeV)

3. Introduce another variable which is calculable using only measured quantities and which exhibits a high degree of correlation with $\cos(\theta^*)$.

Of the above three, the third method is chosen in this thesis, mainly for its simplicity, but also because:

- such a variable can be used in searches for New Physics, as will be illustrated in Section 6.4.2. In this regime, it is best to work with quantities which are fully calculable from observed quantities, without performing a boost to the rest-frame under a specific mass hypothesis,
- templates of such a variable can be generated according to a pure left-handed, right-handed or longitudinal boson, thus allowing a measurement of the W boson polarisation via e.g. a maximum likelihood fit of these templates. This is the main theme of Chapter 7.

A Lepton Projection (LP) variable is thus constructed. It is defined to be the projection of the transverse momentum of the charged lepton ($\vec{P}_T(\ell)$) to the normalized transverse momentum of the W boson $\vec{P}_T(W)$:

$$\mathrm{LP} = \frac{\vec{P}_T(\ell) \cdot \vec{P}_T(W)}{|\vec{P}_T(W)|^2} \tag{6.1}$$

The distribution of the LP variable for $P_T(W) > 100$ GeV is shown for both W boson charges in Figure 6.13(b), with the corresponding $\cos(\theta^*)$ distribution for the same phase-space shown in Figure 6.13(a) for comparison. Similar features are seen, namely the charge asymmetry of W^+ vs W^-, and the effects of the W boson polarisation, with the negatively charged lepton peaking at higher values of LP than the positively charged one. Using detector-level quantities, $\vec{P}_T(W)$ may be estimated using e.g. the missing energy and lepton vectors: $\vec{P}_T(W) = \vec{E}_T^{\mathrm{miss}} + \vec{P}_T(\ell)$. In the regime where the W boson mass cannot be ignored, i.e. at low $P_T(W)$, values of the LP variable can lie outside the range [0,1]. This is discussed in Sections 6.3.2 and 6.3.3.

6.3.2 Correlation with $\cos\theta^*$

The momentum of either W boson decay lepton in the lab frame, relative to the W boson flight direction, may be written as:

$$|\vec{P}(\ell)_{\|}| = \gamma\frac{M_W}{2}(\cos(\theta^*) + \beta) \tag{6.2}$$

$$|\vec{P}(\ell)_{\perp}| = \sin(\theta^*)\frac{M_W}{2} \tag{6.3}$$

where $P(\ell)_{\|}$ is the lepton momentum parallel to, and $P(\ell)_{\perp}$ is the lepton momentum perpendicular to, the W-boson flight direction in the laboratory frame, and hence $|\vec{P}(\ell)| = \frac{M_W}{2}\sqrt{\gamma^2(\cos(\theta^*)+\beta)^2 + \sin^2(\theta^*)}$. Writing $\mathrm{LP}_{3\mathrm{D}} = \frac{|\vec{P}(\ell)|}{|\vec{P}(W)|}$ and noting:

$$\beta = \tfrac{|\vec{P}(W)|}{E(W)}, \quad \gamma = \tfrac{E(W)}{M_W} = \sqrt{1 + \left(\tfrac{|\vec{P}(W)|}{M_W}\right)^2} \tag{6.4}$$

a rearrangement yields:

$$\cos(\theta^*) = \left(2\mathrm{LP}_{3\mathrm{D}} - \tfrac{E(W)}{|\vec{P}(W)|}\right) \tag{6.5}$$

Hence in the high-$P_T(W)$ limit, where $\mathrm{LP}_{3\mathrm{D}} = \mathrm{LP}$, and $\frac{E(W)}{|\vec{P}(W)|} = 1$, the LP variable and $\cos(\theta^*)$ are equivalent. The correlation between $2(\mathrm{LP} - \frac{1}{2})$ and $\cos(\theta^*)$ is shown in Figures 6.14(a) and 6.14(b) for values of $P_T(W) > 200$ GeV and $P_T(W) > 400$ GeV respectively. As can be seen, the larger the momentum of the W boson, the more closely LP tracks the actual value of the $\cos(\theta^*)$ variable. Values at about zero in LP correspond roughly to values of -1 in $\cos(\theta^*)$ due to the boost back to the boson rest frame.

6.3.3 Correlation with ϕ^*

In the massless limit, the LP variable is not correlated with ϕ^*, by virtue of the fact that in the laboratory frame the W boson and decay lepton flight direction are

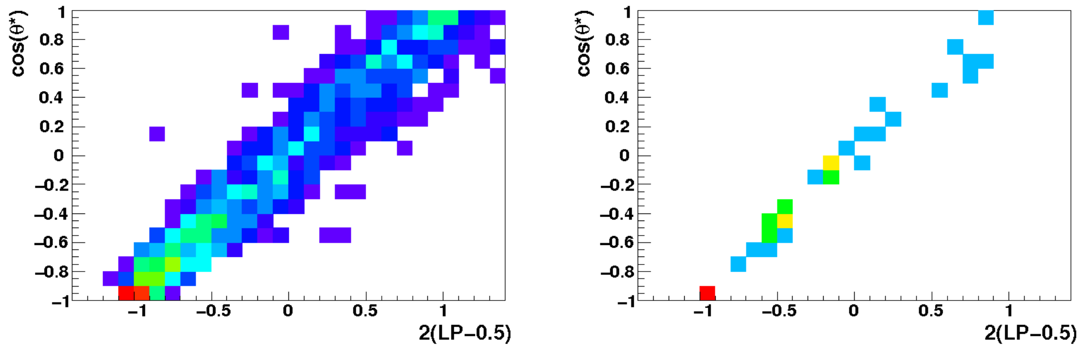

(a) $P_T(W) > 200$ GeV

(b) $P_T(W) > 400$ GeV

Figure 6.14: Correlation plots between $\cos(\theta^*)$ and $2(\mathrm{LP} - \frac{1}{2})$, for W bosons with a transverse momentum above 200 GeV (a) and above 400 GeV (b) ($\sqrt{s} = 10$ TeV)

essentially collinear. This is confirmed by the equivalence of $\cos(\theta^*)$ and LP in this limit, as shown in Section 6.3.2. At low momentum however, where mass effects cannot be neglected, the decay lepton is no longer constrained to travel along the boson flight direction i.e. the mass of the W boson contributes to the decay such that the value of the projected lepton $\vec{P}_T(\ell)$ can both be larger than $|\vec{P}_T(W)|$, as well as in the opposite direction, leading to values of the LP variable outside the range $[0, 1]$. Also, the shape of the LP variable is a function of $P_T(W)$. This ϕ^* dependence of $P_T(\ell)$ at low $P_T(W)$ translates directly to the LP variable, and can be seen by plotting the difference between it and the massless approximation of $\cos\theta^*$, as a function of ϕ^*. This is shown in Figure 6.15(a) for $50 < P_T(W) < 100$ GeV and Figure 6.15(b) for $P_T(W) > 100$ GeV. The ϕ^* dependence is clearly visible, and gets smaller with increasing $P_T(W)$. Values of $\phi^* = \pi/2$ correspond to $x = 0$ in the helicity frame (see Figure 2.7), i.e. the W mass contributes to a change in the lepton flight along the detector ϕ direction in the lab frame, and so the transverse momentum of the lepton is unchanged. This is identical to the scenario in the massless limit, and hence in this case the difference is zero.

In conclusion, the ϕ^* dependence of the LP variable exhibited in Figures 6.15(a) and 6.15(b) implies that the shape of the LP variable is not only dependent on $\cos(\theta^*)$, regardless of lepton acceptance effects.

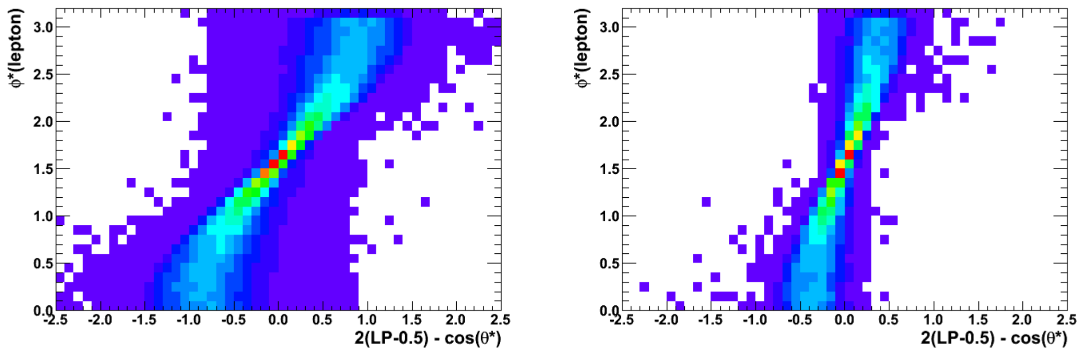

(a) $50 < P_T(W) < 100$ GeV

(b) $P_T(W) > 100$ GeV

Figure 6.15: Correlation plots between $[2(\mathrm{LP} - \frac{1}{2})] - \cos(\theta^*)$ and ϕ^*, for W bosons with a transverse momentum between 50 and 100 GeV (a) and above 100 GeV (b) ($\sqrt{s} = 7$ TeV)

6.3.4 Effects of A_i coefficients

More generally, the correlation with ϕ^* means that the LP variable is dependent on more than just the diagonal elements of the helicity density matrix, namely f_L, f_R and f_0, i.e. the A_0 and A_4 coefficients from Equation 2.9. Given that one of the aims of this analysis is to generate templates of the LP variable to fit to the data in order to extract the corresponding helicity of W bosons, it is necessary to gauge the sensitivity of the LP variable to those coefficients which will not be fitted for i.e. the implicit assumption for the values of A_1, A_2 and A_3.

In order to do this, the difference in the shape of the LP distribution at generator level is determined, according to a relative increase of 10% in each of the A_i coefficients individually i.e. "new" shape $-$ "old" shape. Since the A_i coefficients are a function of the W boson charge, $P_T(W)$ and $|Y(W)|$, their values are determined in such bins via fitting to the analytical form of Equation 2.9. Three bins in $P_T(W)$ are chosen, $(0 - 50$ GeV, $50 - 100$ GeV, > 100 GeV) and seven bins in $|Y(W)|$ (in bins of 0.5 up to 3.0, and one bin for $|Y| > 3.0$). A simple reweighting of each event is then performed based on a relative increase of 10% of each of the A_i coefficients. The results of this procedure for the positive charge for the A_0 to A_4 coefficients are shown in Figures 6.16 to 6.18 respectively, whereby similar results are obtained for

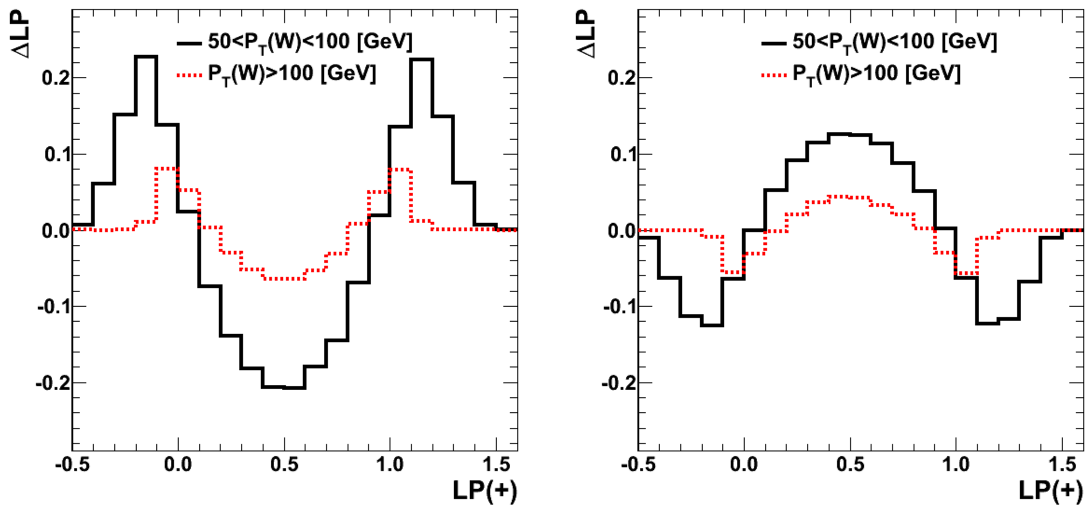

(a) The A_0 component derivative

(b) The A_1 component derivative

Figure 6.16: The LP(+) derivatives for two bins in $P_T(W)$ shown for A_0 (a) and A_1 (b).

the negative charge, and opposite results are obtained for a relative decrease of 10% of each of the A_i coefficients.

The difference in the shape of the LP distribution for the $A_0(\sim f_0)$ parameter is as expected, enhancing the longitudinal mode (increasing LP values around 0.5) and suppressing the left-handed and right-handed modes (reducing LP values around 0.0 and 1.0). The size of such derivatives depends on three parameters, namely the initial value of the A_i parameter in the $P_T(W)$ bin chosen, the correlation of the LP variable with ϕ^*, and the number of events in the bin. The size of the derivative of the A_0 parameter reduces with increasing $P_T(W)$, presumably since the longitudinal mode gets smaller. The derivative of the $A_4(\sim (f_L - f_R))$ distribution also behaves as expected, enhancing the left-handed mode, whilst suppressing the right-handed mode. The size of this derivative is about an order of magnitude larger than the others, which indicates that the LP variable is most sensitive to this parameter. The A_1 and A_2 derivatives are correlated in shape to the A_0 variable, whilst the derivative of A_3 is small by virtue of its initial value being very small, as seen in Figure 6.2. The corresponding derivatives at the reconstruction level, which also fold in the detector acceptance, are discussed in Chapter 7.

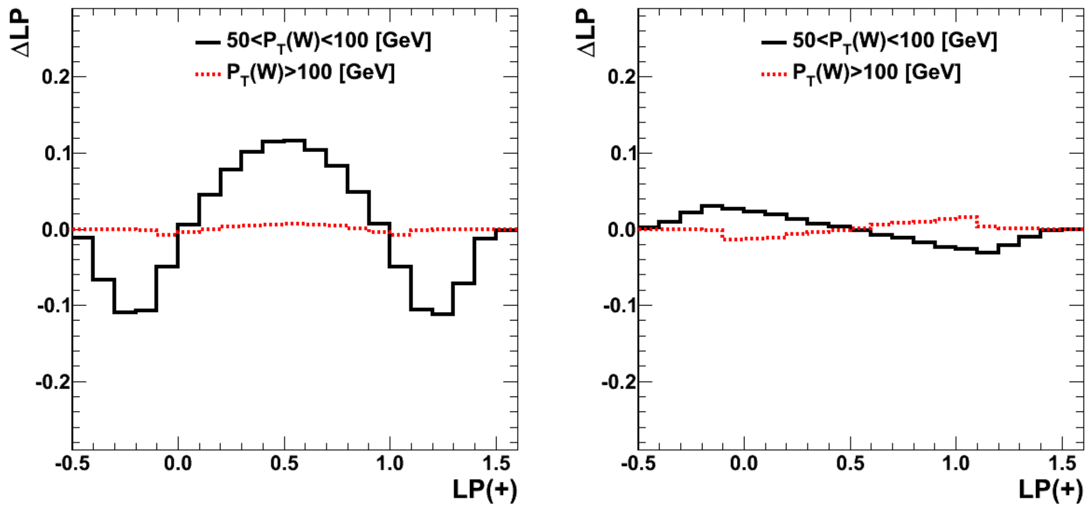

(a) The A_2 component derivative (b) The A_3 component derivative

Figure 6.17: The LP(+) derivatives for two bins in $P_T(W)$ shown for A_2 (a) and A_3 (b).

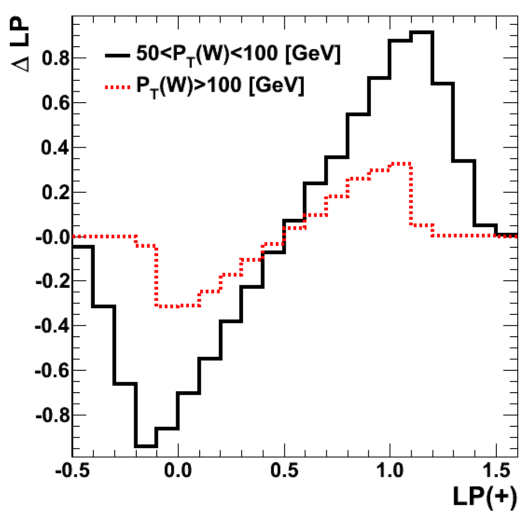

Figure 6.18: LP(+) derivative for two bins in $P_T(W)$ shown for A_4.

6.4 LP variable applications

The studies presented in Sections 6.4.1 and 6.4.2 illustrate two potential applications of the LP variable at the reconstruction level i.e. using detector-level quantities. The first relates to using the different polarisation properties of W bosons with respect to those produced from $t\bar{t}$ events, in order to distinguish between them, whilst the second uses the polarisation properties of both W and $t\bar{t}$ events in the search for New Physics. These studies were performed using Monte Carlo samples generated at $\sqrt{s} = 10$ TeV, and are normalised to 100pb^{-1} of integrated luminosity. The same Monte Carlo samples as those in Sections 5.3 and 6.1 are used.

6.4.1 Distinguishing $t\bar{t}$ and W events

The idea behind using the LP variable to separate $t\bar{t}$ and W boson events stems from the expectation that for $t\bar{t}$ events, a symmetric contribution from both charges will occur, both in the shape of LP distribution, and also with the number of events. This is due to the different production mechanisms for such events (quark-quark and gluon-gluon dominated), where the initial states and their CPT-counterparts are present in equal amounts. In order to test such expectations, a Standard Model enriched phase space ($t\bar{t}$ and W) is chosen. The following object and kinematic definitions are used:

- Jets: $P_T > 30$ GeV and $|\eta| < 3$,
- Muons: $P_T > 15$ GeV and $|\eta| < 2.1$,
- $\vec{H}_T^{\text{miss}} = \sum_{j=0}^{j=N} -\vec{P}_T^j$, where N is the number of jets and $\vec{P}_T^j$ is the transverse momentum of jet j,
- $H_T = \sum_{j=0}^{j=N} P_T^j$.

The following selection criteria are applied:

- $H_T^{\text{miss}}(\sim P_T(W)) > 200$ GeV,
- $N_{\text{muons}} = 1$,
- ΔR (muon, jet) > 0.5 (for QCD rejection),
- $N_{\text{jets}} > 2$.

The LP variable distributions for the sum of, and difference between, both muon charges are shown in Figures 6.19(a) and 6.19(b) respectively. The SUSY LM0 and LM1 benchmark signals are shown for completeness, but do not contribute to the calculations which follow. The $t\bar{t}$ and W+jets distributions of Figure 6.19(a), in the case where both charges are combined, show similar behaviour, whilst the difference between the two charges is clearly dominated by W+jets (as expected), and is relatively flat for values of LP > 0.3.

By counting the resulting numbers of events for both lepton charges and calculating the difference between these numbers $(N_+ - N_-)$, it is possible to estimate both $t\bar{t}$ and W+jets contributions individually using charge asymmetry arguments, namely that this difference is expected to be zero for a $t\bar{t}$ sample. The ratio $r = N_+^{\text{gen}}/N_-^{\text{gen}}$ is found to be $r = 1.93 \pm 0.17$ at the generator level for W bosons. The result of multiplying $(N_+ - N_-)$ with $\frac{r+1}{r-1}$ is shown in Table 6.2 for the W+jets case. The $t\bar{t}$ estimate is simply the difference between this estimate and the measured $(N_+ + N_-)$.

Whilst the calculation of this ratio at generator level includes muon acceptance criteria, the reconstruction efficiency and resolution effects of these muons are ignored, mainly due to the fact that the statistical uncertainty is dominating. The results in Table 6.2 show that the predicted and measured values agree within the statistical uncertainties of the Monte Carlo simulation, which only reflects a closure test of the simulation. For reference, the statistical uncertainty in the estimation of the W boson content for a dataset equivalent to an integrated luminosity of 100 pb^{-1} at 10 TeV, is about 25%, and is inversely proportional to the number of W boson events selected. At 7 TeV, the ratio of W+jets to $t\bar{t}$ events changes in favour of W+jets events, since the $t\bar{t}$ cross-section decreases faster then the W boson cross-section with decreasing centre of mass energy.

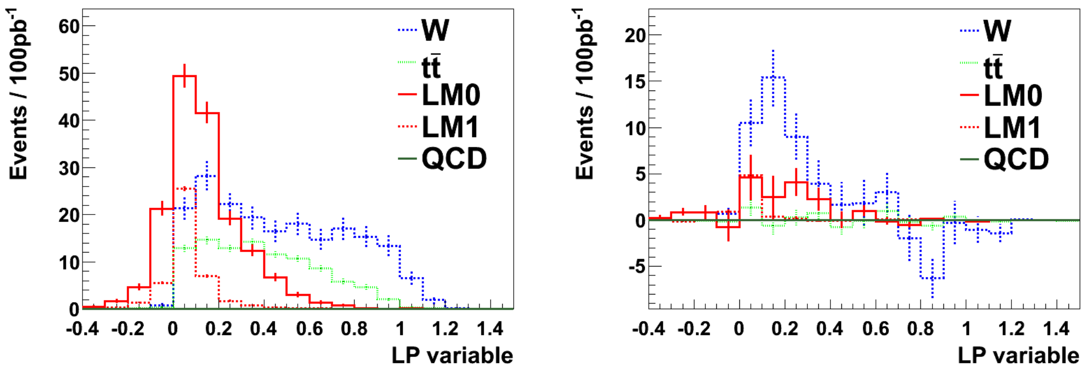

(a) The LP variable for the sum of both muon charges

(b) The LP variable for the difference between both muon charges

Figure 6.19: The LP variable for the sum of (a) and difference between (b) both muon charges in the $N_{\mathrm{jet}} > 2$ phase space.

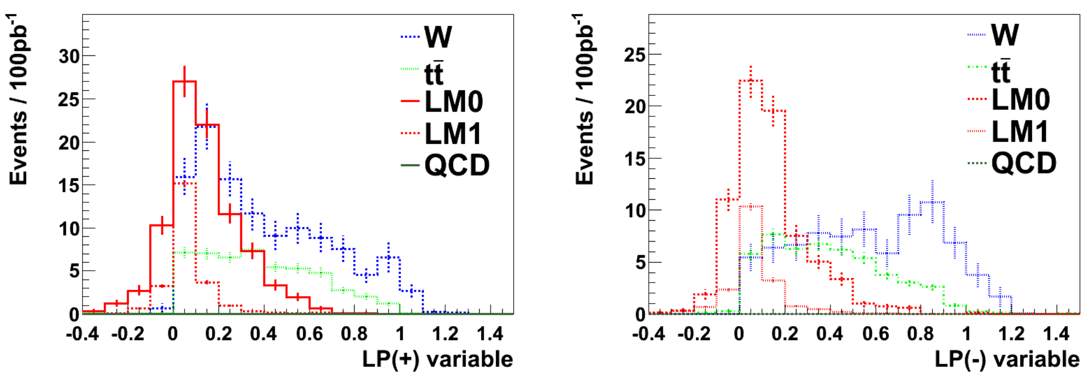

(a) The LP variable for the positively charged muon

(b) The LP variable for the negatively charged muon

Figure 6.20: The LP variable for the positively charged (a) and negatively charged (b) muon in the $N_{\mathrm{jet}} > 2$ phase space.

Table 6.2: Predicted and measured events for 100 pb^{-1} at 10 TeV in the absence of SUSY. The uncertainties reflect the limited number of simulated events.

dataset	predicted number of events	measured number of events
W+jets	130 ± 24	143 ± 7.8
$t\bar{t}$	115 ± 24	99 ± 2.5

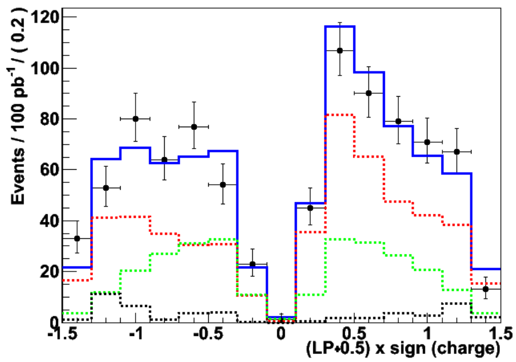

Figure 6.21: The (LP+0.5) distributions (templates) multiplied by the sign of the lepton charge for W+jets (red), $t\bar{t}$ (green) and Z+jets and QCD (black) events passing the selection criteria as defined in the relevant part of Section 6.4.1 are shown. The black dots represent the result of a toy experiment according to the total number of events in each bin for an integrated luminosity of 100pb^{-1}, with the blue line representing the binned maximum likelihood fit result to this toy data using the individual templates. ($\sqrt{s} = 7$ TeV)

Aside from using the difference in the number of events for both lepton charges (i.e. charge asymmetry), the difference in shapes of the $t\bar{t}$ and W+jets LP variable (i.e. polarisation), as shown in Figures 6.20(a) and 6.20(b), can also be used to gain further separation power. This is demonstrated using the $\sqrt{s} = 7$ TeV Monte Carlo samples as defined in Section 6.1, with the selection criteria being modified to:

- $H_T^{\text{miss}} > 100$ GeV,
- $P_T(\mu) > 20$ GeV.

Templates of the LP variable for W+jets, $t\bar{t}$, and Z+jets and QCD events are shown for both charges on the same histogram in Figure 6.21. A binned maximum likelihood fit of these templates to the result of a toy experiment for an integrated luminosity of 100pb^{-1} is also shown across both charges. The results show that the statistical uncertainty at 100pb^{-1} is reduced to 7% when combining both charge asymmetry and polarisation effects.

6.4.2 New Physics searches

In order to demonstrate how the LP variable can be used in the search for New Physics at $\sqrt{s} = 10$ TeV, the $\sqrt{s} = 10$ TeV selection criteria of Section 6.4.1 are modified as follows:

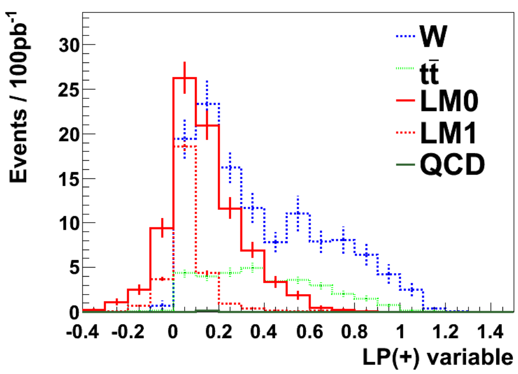

(a) The LP variable for the positively charged muon

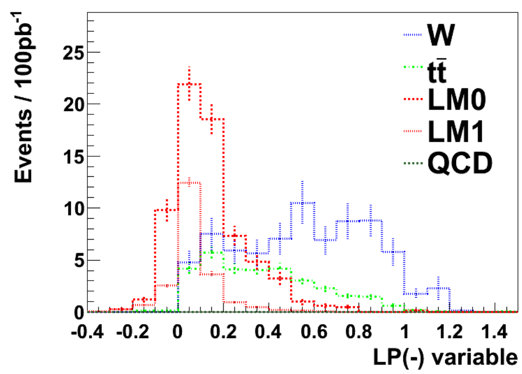

(b) The LP variable for the negatively charged muon

Figure 6.22: The LP variable for the positively charged (a) and negatively charged (b) muon in the SUSY phase space.

- $H_T > 350$ GeV ($\sim 2 \times m_{\text{top}}$),
- $N_{\text{jets}} > 1$.

The LP variable for both the positive and negative muon charges is shown in Figures 6.22(a) and 6.22(b) respectively for the updated selection criteria. Once again, the helicity and charge asymmetries for W+jets and $t\bar{t}$ events are clearly visible. For the R-parity conserving SUSY signal, the charged lepton is typically less aligned with the direction of H_T^{miss}. This is because the H_T^{miss} stems from at least two invisible LSPs and a neutrino, which also typically means that the charged lepton P_T is smaller than H_T^{miss}, and in some cases can point in the opposite direction to it. Consequently, the SUSY benchmark points exhibit significantly different characteristics from W+jets and $t\bar{t}$ events.

The LP variable distribution for the sum of both positive and negative muon charges is shown in Figure 6.23(a). Again, the $t\bar{t}$ and W+jets shapes are similar when the charges are combined. Figure 6.23(b) shows the corresponding plot for the difference between the two charges, and even in this phase-space region W+jets events dominate.

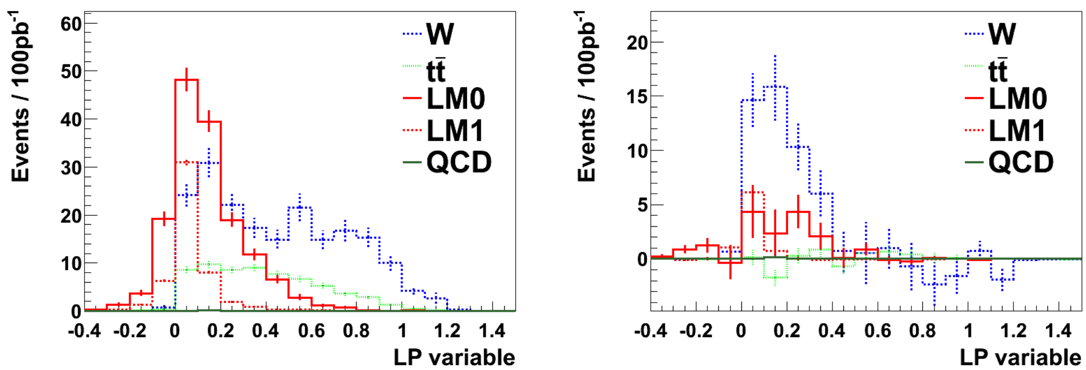

(a) The LP variable for the sum of both muon charges

(b) The LP variable for the difference between both muon charges

Figure 6.23: The LP variable for the sum of (a) and difference between (b) both muon charges in the SUSY phase space.

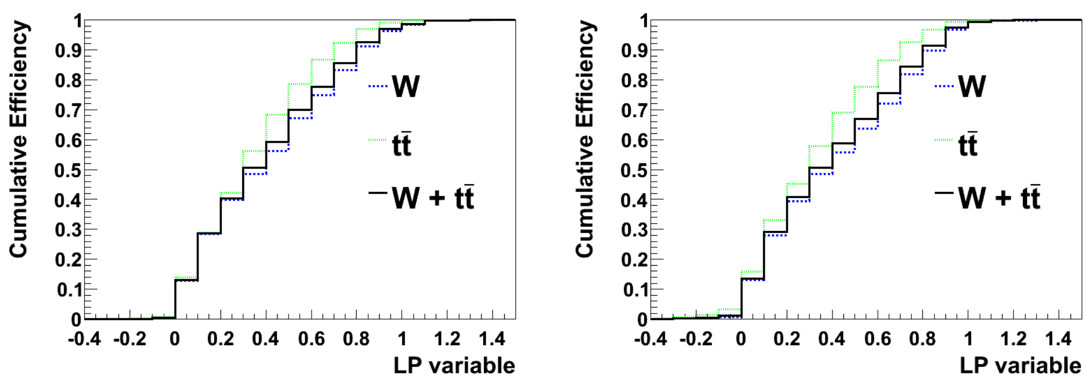

(a) Cut efficiency at reconstruction level

(b) Cut efficiency at generator level

Figure 6.24: The cut efficiencies for the LP variable with both charges summed, constructed using reconstruction-level (a) and generator-level (b) information.

Table 6.3: Predicted and measured events for 100 pb^{-1} at 10 TeV, with the LP variable in the signal region LP < 0.3.

datasets	predicted W+jets and $t\bar{t}$ events	measured events
SM only	85 ± 9	77 ± 9
LM0+SM	105 ± 10	209 ± 14
LM1+SM	86 ± 9	126 ± 11

Figure 6.24(a) shows the efficiency for a cut on the LP variable for combined charges of both W+jets and $t\bar{t}$ events. At a value of LP=0.3, the cut efficiency is about the same for both samples individually, between 0.43 - 0.46. Figure 6.24(b) shows the cut efficiency based on the generator level information, in which muons that do not originate from a W-boson decay are not included. Again, only the acceptance cuts of the generator muon are applied, whilst the reconstruction efficiency and resolution effects are ignored. The H_T^{miss} is calculated on parton level without any acceptance cuts. Comparing Figure 6.24(a) with Figure 6.24(b) implies that resolution effects, instances of muons originating from b-jets and other effects in general are small. This distribution can be assumed to be well predicted by MC simulation, and may be confirmed by validation exercises in the 1-jet bin. At generator level, the cut efficiencies are the same for W+jets and $t\bar{t}$ at a cut value of LP=0.3, where the efficiency is 0.46. This value can then be used to extrapolate from a control region (LP > 0.3) to a signal region (LP < 0.3) at reconstruction level.

Table 6.3 shows the results of such a procedure, where there is a slight over-estimation in the number of SM only events. This is because the cut efficiencies differ slightly between reconstruction and generator level. Also note that the QCD background (2.4 events) is not predicted. The systematic uncertainty of this approach will depend on how well the W boson helicity can be measured and understood at the time such a procedure might be performed. In the case of predictions with signal, the number of SM events are not largely affected, as the control region has a low signal contamination. For the LM1 parameter point, this contamination is almost zero, whilst for the LM0 point, this contamination leads to an increment of about 20-25% in the predicted number of SM events in the signal region. However, in both cases a signal can clearly be observed.

In conclusion, the LP variable can be used to distinguish between events originating from W and $t\bar{t}$ events on a statistical basis, achieving a statistical uncertainty of 7% at 100pb^{-1}. The fact that New Physics is unlikely to exhibit the same helicity effects and asymmetries as $t\bar{t}$ or W+jets means that the LP variable can also be used as as a search parameter. The applications of the LP variable illustrated in this chapter however, are not intended to fully optimise certain parameters (such as signal over background), but to serve as an example of how helicity effects may be used.

Chapter 7

Towards a Measurement of W Boson Polarisation

7.1 Introduction

Recalling Equation (2.9):

$$\frac{\mathrm{d}N}{\mathrm{d}\Omega} \sim (1+\cos^2\theta) + \tfrac{1}{2}A_0(1-3\cos^2\theta) + A_1\sin 2\theta\cos\phi$$
$$+\tfrac{1}{2}A_2\sin^2\theta\cos 2\phi + A_3\sin\theta\cos\phi + A_4\cos\theta$$

it can be seen that when detector effects are considered, most notably from finite resolution, acceptance and reconstruction efficiency, the $\cos(\theta^*)$ and ϕ^* distributions will be distorted such that the form of e.g. the $\cos(\theta^*)$ distribution is no longer solely dependent on the A_0 and A_4 coefficients of the helicity density matrix (i.e. f_L, f_R and f_0), but also on the other A_i coefficients. This is due to the fact that $\int_0^{2\pi}\alpha(\phi^*)\cos\phi^*\mathrm{d}\phi^* \neq 0$, where $\alpha(\phi^*)$ models the detector acceptance as a function of ϕ^*, and so the A_1, A_2, and A_3 coefficients no longer vanish when integrating over ϕ^*.

Figure 7.1 shows the ϕ^* distribution at generator level for leptons with and without a $P_T(\ell) > 10$GeV and $|\eta(\ell)| < 2.1$ acceptance cut. The distribution around $\phi^* = 0$, i.e. low $P_T(\ell)$, is affected the most as expected from Section 2.4.2. The dependencies

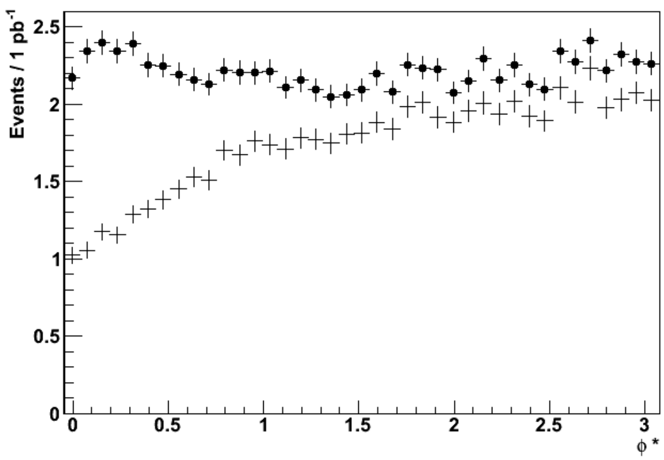

Figure 7.1: The lepton ϕ^* distribution at generator level before (solid dots), and after an acceptance cut of $P_T(\ell) > 10$GeV and $|\eta(\ell)| < 2.1$ for $P_T(W) > 100$GeV. ($\sqrt{s} = 7$ TeV)

on the A_1, A_2 and A_3 coefficients are taken from the Monte Carlo simulation, whose values are as shown in Figure 6.2.

In order to extract the values of f_L, f_R, and f_0, there are two approaches that may be taken to quantify such detector effects:

1. Define a functional form modelling the effects of the CMS detector and use this to perform an analytical fit on the resulting detector distribution.

2. Produce detector-level templates for the scenarios where the W boson helicity is fixed to be 100% left-handed, 100% right-handed and 100% longitudinal, and perform a maximum likelihood fit of these templates on the resulting detector distribution.

As described in Chapter 6, and given the complexity of the first method, the template method is chosen in this analysis, specifically with the LP variable. The studies presented in this chapter are thus aimed at a first measurement of the helicity of W bosons at the LHC using the first data acquired from the $\sqrt{s} = 7$ TeV collision dataset. All Monte Carlo generated samples used in this chapter are generated at $\sqrt{s} = 7$ TeV.

7.2 Event Selection Criteria

Before any studies of the template method are carried out, it is helpful to define a set of detector-level selection criteria which will be used to extract the W boson helicity. Given that one of the aims of this analysis is an early measurement of this helicity, the $P_T(W)$ region probed can be extended to $P_T(W) > 50$ GeV, i.e. in a regime where mass effects cannot be ignored, as supported by the LP derivatives of the A_i coefficients from Figures 6.16 to 6.18.

In this thesis, the muon channel is considered exclusively, primarily because it is the easiest of the three lepton flavours to reconstruct offline from detector-level quantities. This is done using the CMS muon stations, as described in Section 3.2.4, using two different methods:

1. Global muons are reconstructed using information from the muon stations, which is then matched with a track reconstructed in the silicon tracker. Global muons are the only type of reconstructed muon which are triggered on. The pseudo-rapidity coverage of such muons is $|\eta(\mu)| < 2.4$, whilst the range of the trigger is limited to $|\eta(\mu)| < 2.1$.

2. Tracker muons are reconstructed using tracks from the silicon tracker, which are then matched to tracklets in the muon stations. The pseudo-rapidity coverage of such muons is $|\eta(\mu)| < 2.4$.

In addition to prompt muons from the decay of W and Z bosons, muons reconstructed in the CMS detector originate primarily from two "background" sources [50]:

1. Heavy Flavour: muons from semi-leptonic (weak) decays of c and b-flavoured hadrons,

2. Light Flavour: decays-in-flight of pions and kaons produced inside hadronic jets.

Muons may also be reconstructed from hits left in the muon chambers originating from hadrons which "punch-through" the HCAL, as well as other reconstruction and instrumental effects. Muons from all these sources which pass the event selection criteria are classed as fake muons. In order to suppress such background muons, a simple and robust muon identification is applied to aid the selection criteria.

7.2.1 Muon ID variables

The muon identification used is cut based, with the aim of simplifying efficiency calculations and selecting prompt muons. The following ID variables, derived from [50] [51], are used:

- A reconstructed muon must be identified as both a global and tracker muon. This is to protect against accidental wrong matchings with the tracker (in the case of global muons), or with noisy muon chamber segments (in the case of tracker muons). This cut is also effective against muons reconstructed from decays-in-flight and punch-through.
- The number of valid tracker hits associated with the reconstruction of the muon must exceed 10. This is to ensure a good transverse momentum estimate, and to veto against decays-in-flight which give rise to a lower track occupancy.
- The normalized χ^2 of the global muon fit (using silicon tracker and muon chamber information) must be smaller than 10, to reject bad fits.
- The transverse impact parameter of the muon with respect to the beamspot must be less than 2mm. This is a loose cut which rejects the majority of reconstructed cosmic muons. (This could potentially be replaced with a cut of the transverse impact parameter of the muon with respect to the primary vertex in a tighter selection.)
- The number of pixel hits must be at least one, to suppress muons from decays-in-flight.

- There must be at least two muon stations involved in the reconstruction of the tracker muon. This cut suppresses punch-through and accidental matchings, and is used to comply with the same logic used at the trigger.

- There must be at least one valid hit in the muon chambers associated with the reconstructed global muon, in order to prevent decays-in-flight and punch-through.

- The pseudo-rapidity range of the reconstructed muons must be within the range $|\eta(\mu)| < 2.1$ in order to match the muon trigger requirements.

The reconstructed muons must also be isolated, according to the isolation variable $I^{\mathrm{rel}}_{\mathrm{comb}} < 0.10$, which is defined as:

$$I^{\mathrm{rel}}_{\mathrm{comb}} = \frac{\sum \left(P_T(\mathrm{tracks}) + E_T^{\mathrm{EM}} + E_T^{\mathrm{HAD}}\right)}{P_T(\mu)}$$

where $\sum P_T(\mathrm{tracks})$, $\sum E_T^{\mathrm{EM}}$ and $\sum E_T^{\mathrm{HAD}}$ are the sums of all the transverse momenta from the tracks, electromagnetic deposits and hadronic deposits respectively, within a cone of $\Delta R = \sqrt{(\Delta\phi)^2 + (\Delta\eta)^2} < 0.3$.

7.2.2 $W \rightarrow \mu\nu$ Muon Event Selection

The selection requirements in the muon channel are as follows:

1. Trigger: the existence of at least one muon above 9 GeV at the HLT,
2. Exactly one tight muon,
3. Exactly zero electrons,
4. Less than four jets,
5. A ΔR_{min}(muon, jet) > 0.5 cut,
6. A transverse mass of at least 30 GeV,
7. A Z-boson mass window veto of ± 25.0 GeV,

8. A $P_T(W) > 50$ GeV cut.

The following definitions are used:

- A tight muon is defined using the muon ID as in section 7.2.1, but with $P_T(\mu) >$ 10 GeV.
- An electron is defined as having $P_T(e) > 20$ GeV and $|\eta(e)| < 2.5$.
- A jet is defined using the anti-k_T algorithm with a cone-radius of 0.5, and $P_T > 20$ GeV, $|\eta(\text{jet})| < 5.0$ and electromagnetic fraction < 0.9.
- The Z mass window veto is applied on the value of the invariant mass between the tight muon and all other reconstructed muons individually, lying in the range 91.2±25.0 GeV. If no other reconstructed muons exist, the event survives this cut.
- The transverse mass is defined as $M_T = \sqrt{2P_T(\mu)P_T(\nu)(1 - cos(\Delta\phi(\mu,\nu)))}$, where the neutrino transverse momentum is estimated using E_T^{miss}.
- The value of $P_T(W)$ is estimated from $|\vec{E}_T^{\text{miss}} + \vec{P}_T(\mu)|$, hereafter referred to as the reconstruction level $P_T(W)$.

7.2.3 Event yields

The number of W boson events surviving the selection requirements as defined in Section 7.2.2, are shown in Table 7.1 for an integrated luminosity of 1pb^{-1}. Also shown are the contributions from the major SM backgrounds to this analysis, namely from QCD, Z+jets and $t\bar{t}$ events, along with the cross-sections used.

7.3 A_i derivatives at reconstruction level

Given the impact on the $\cos(\theta^*)$ and ϕ^* distributions from detector effects, the inherent LP variable dependence on both $\cos(\theta^*)$ and ϕ^*, as described in Sections 6.3.2

Table 7.1: Muon channel event-yields for signal (W) and SM backgrounds, expected for an integrated luminosity of 1pb^{-1} following the selection requirements as defined in Section 7.2.2. The QCD sample used is for $\hat{p}_T > 15$ GeV.

	W+Jets	QCD	Z+Jets	$t\bar{t}$	S/B
Cross-section (pb)	31314 NNLO	8.76×10^8	3100 NNLO	157.5 NLO	-
Trigger	6313	493887	908	46.6	0.01
$N_\mu = 1$, $N_e = 0$	5041	30571	473	21.2	0.16
< 4 jets	5654	30515	469	7.29	0.18
$\Delta R_{\mathrm{min}}(\mu, \mathrm{jet}) < 0.5$	5487	29439	455	6.94	0.18
Z Window Mass Cut	5479	29439	327	6.47	0.18
$P_T(W) > 50$GeV	261	23.4	15.6	4.47	6.00
$M_T > 30$GeV	212	0.01	6.24	3.65	21.4

and 6.3.3 respectively, changes. In order to see the effects that this has on the correlations of the LP variable, the exercise of Section 6.3.4 is repeated at the reconstruction level, using the event selection criteria of Section 7.2.2. The A_i derivatives at the reconstruction level are shown in Figures 7.2 to 7.4. The overall features are the same, namely the dominance of the A_0 and A_4 coefficient derivatives.

7.4 Template Generation

There are two approaches that may be taken in order to generate templates of the LP variable for the 100% left-handed, 100% right-handed and 100% longitudinal helicity states. One can either regenerate the Monte Carlo samples and detector reconstruction three times, one each for polarisation state, or reweight the existing Monte Carlo sample for different polarisation fractions. Given the computational overhead associated with event simulation, the second method is chosen.

7.4.1 Reweighting Method

The reweighting procedure is based on changing the shape of the $\cos(\theta^*)$ distribution at generator level without any acceptance cuts, such that $f_L = 1.0$, $f_R = 1.0$ and $f_0 = 1.0$ independently. Since the values of the f_i parameters are a function of the

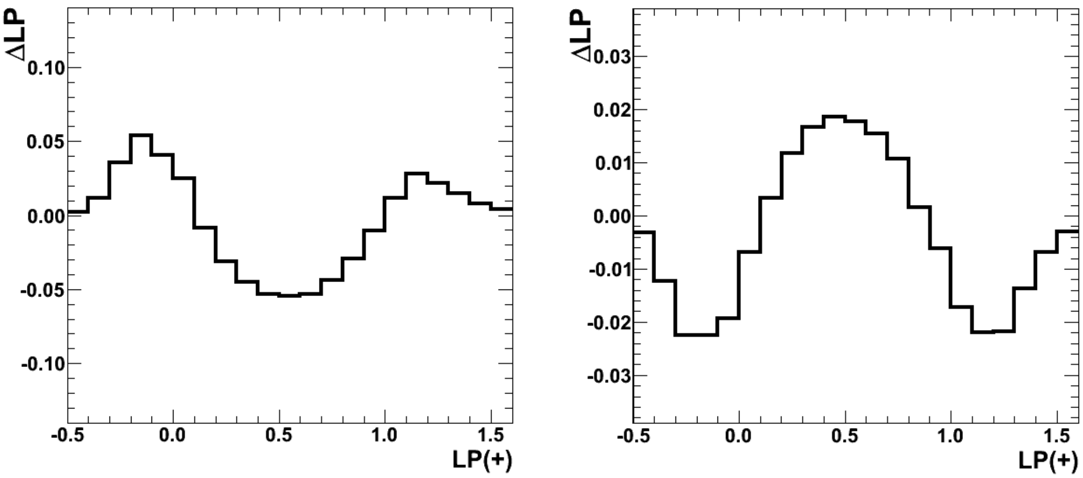

(a) The A_0 component derivative

(b) The A_1 component derivative

Figure 7.2: The LP(+) derivatives at the reconstruction level for $P_T(W) > 50$ GeV shown for the A_0 (a) and A_1 (b) coefficients.

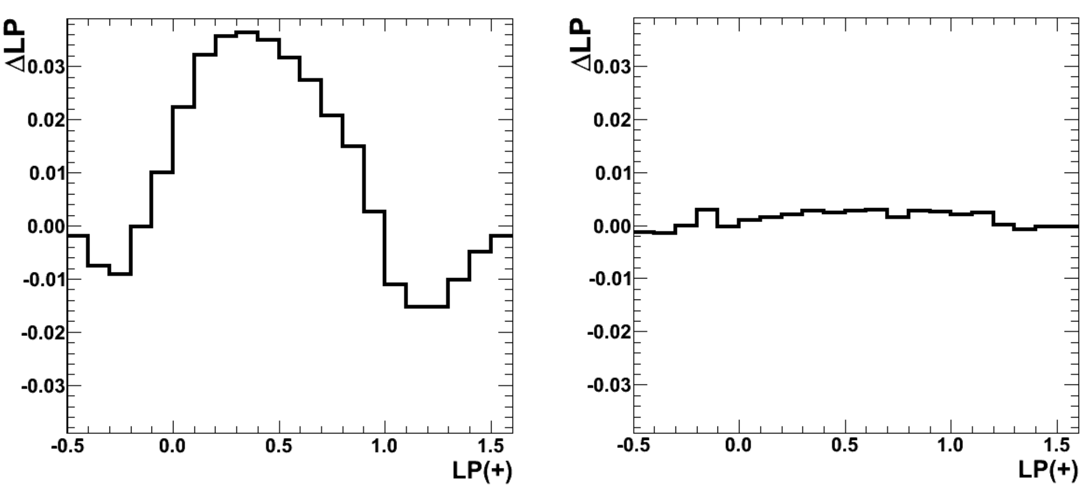

(a) The A_2 component derivative

(b) The A_3 component derivative

Figure 7.3: The LP(+) derivatives at the reconstruction level for $P_T(W) > 50$ GeV shown for the A_2 (a) and A_3 (b) coefficients.

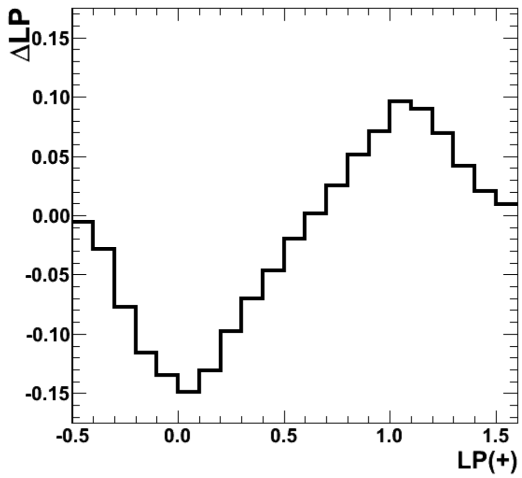

Figure 7.4: The LP(+) derivative at the reconstruction level for $P_T(W) > 50$ GeV shown for the A_4 coefficient.

charge, $P_T(W)$ and $|Y(W)|$, the reweighting factors must model this dependence. The W boson production phase-space $((P_T(W), |Y(W)|))$ is binned independently for each charge. As in Section 6.3.4, three bins in $P_T(W)$ (0-50 GeV, 50-100 GeV, >100 GeV), and seven bins in $|Y(W)|$ (in bins of 0.5 up to 3.0, and one bin for $|Y| > 3.0$) are chosen. In each bin of this two-dimensional grid, the $\cos(\theta^*)$ distribution is fitted according to Equations (2.7) and (2.8), in order to extract the set (f_L, f_R, f_0) which correspond to the generated Monte Carlo sample. These values define the amount of reweighting necessary in each such bin, which is applied on an event-by-event basis to any distribution of choice, e.g. the LP variable. This can be done either at the generator level, or at reconstruction level using the corresponding generator level information of the same event e.g. for those events which pass the selection requirements of the analysis. The final piece of information required is therefore the generator level value of $\cos(\theta^*)$ for a particular event. Given the limited number of events generated in the MC sample, the $\cos(\theta^*)$ distribution itself is segmented into 200 bins of equal size (0.01) spanning the range [-1.0, 1.0] inclusive.

The reweighting factor applied to the distributions of choice in a typical event, for some such $\cos(\theta^*)$ bin b, in some $(P_T(W), |Y(W)|)$ bin, for a particular charge $\pm$, is then defined as:

$$k^{\pm}_{\text{pol}}(P_T(W), |Y(W)|) = \frac{\int_b^{b+0.01} F^{\text{new}}(\cos\theta^*)\ \mathrm{d}\cos\theta^*}{\int_{-1.0}^{1.0} F^{\text{new}}(\cos\theta^*)\ \mathrm{d}\cos\theta^*} \div \frac{\int_b^{b+0.01} F^{\text{old}}(\cos\theta^*)\ \mathrm{d}\cos\theta^*}{\int_{-1.0}^{1.0} F^{\text{old}}(\cos\theta^*)\ \mathrm{d}\cos\theta^*} \tag{7.1}$$

where:

- $F^{\text{new,old}}(\cos\theta^*) = f_L^{\text{new,old}} \frac{(1\mp\cos\theta^*)^2}{4} + f_0^{\text{new,old}} \frac{1-\cos^2\theta^*}{2} + f_R^{\text{new,old}} \frac{(1\pm\cos\theta^*)^2}{4}$,
- $f^{\text{old}}_{L,R,0} = f^{\pm}_{L,R,0}\,(P_T(W), |Y(W)|)$ as measured from the original MC sample. This value is a constant for a particular charge and $(P_T(W), |Y(W)|)$ bin,
- $f^{\text{new}}_{L,R,0} = f_{L,R,0}$ (template flavour) i.e. for a 100% left-handed template, the set $(f_L,\ f_R,\ f_0) = (1.0,\ 0.0,\ 0.0)$ etc.

This procedure was carried out at the generator level, for a generator level $P_T(W) >$ 50 GeV cut, and the shapes of the corresponding 100% left-handed, right-handed and longitudinal templates for both lepton charges are shown in Figure 7.5. Since the input values of the f_i parameters depend on both $P_T(W)$ and $|Y(W)|$, the reweighting factor, $k^{\pm}_{\text{pol}}$, is also dependent on both the $P_T(W)$ and $|Y(W)|$. This introduces a subtle issue that is addressed in the following section.

7.4.2 Dependence of the $f^{\text{new}}_{L,R,0}$ on $P_T(W)$ and $|Y(W)|$

To generate the LP templates at the reconstruction level, the association between the generator level and reconstruction level information is used to calculate the appropriate reweighting factors. The shapes of these templates is very important. In the case of the $\cos(\theta^*)$ distribution at the generator level, the shapes of the 100% left-handed, 100% right-handed and 100% longitudinal templates are by definition, all independent of both $P_T(W)$ and $|Y(W)|$ and so no further corrections to the method described in Section 7.4.1 are required. However, the maximum likelihood fit will use the LP variable, and as shown in Figure 7.6, the shapes of the LP variable are not the same with varying $P_T(W)$.

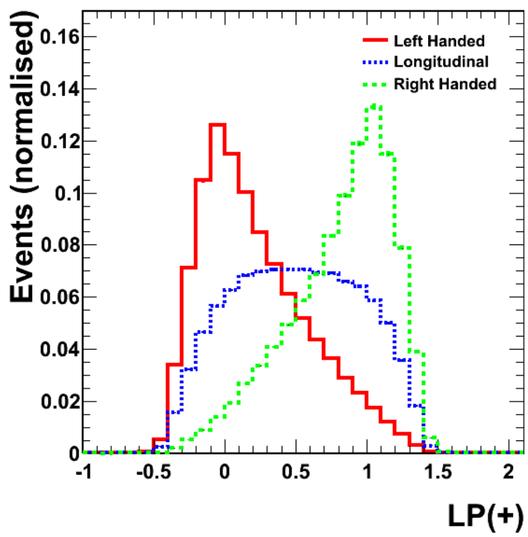

(a) The LP(+) templates at generator level

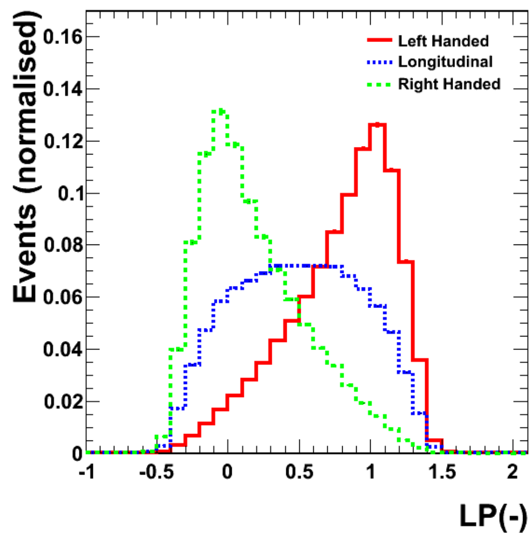

(b) The LP(−) templates at generator level

Figure 7.5: The LP template shapes at the generator level, for a generator level $P_T(W) > 50$ GeV cut, shown for both the positive (a), and negative (b) lepton charges.

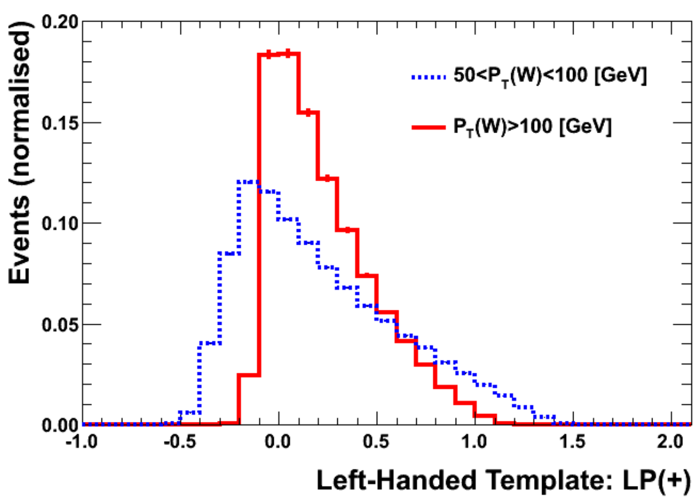

Figure 7.6: The 100% left-handed template of the LP(+) variable, shown for two bins of $P_T(W)$ at the generator level.

Since the aim of the final fit is to extract the average $f_{L,R,0}$ from a particular $(P_T(W), |Y(W)|)$ phase space that corresponds to the reconstruction level selection, an additional correction factor is applied to each of the 100% left-handed, right-handed and longitudinal templates. This extra correction factor favours the regions where, on average, the most left-handed, right-handed and longitudinal W bosons lie respectively. It is also applied on an event-by-event basis, and for a given $P_T(W)$ and $|Y(W)|$ bin, can be written as:

$$K^{\pm}_{L,R,0}(P_T(W), |Y(W)|) = \frac{N^{\pm}_{L,R,0}}{N^{\pm}_L + N^{\pm}_R + N^{\pm}_0} \div \frac{\sum N^{\pm}_{L,R,0}}{\sum N^{\pm}_L + N^{\pm}_R + N^{\pm}_0} \tag{7.2}$$

where:

- $N^{\pm}_{L,R,0} = \int_{P_T^{\mathrm{bin}}(W)} \int_{|Y^{\mathrm{bin}}(W)|} W'(P_T, |Y|, \pm) f'_{L,R,0}(P_T, |Y|, \pm)\, \mathrm{d}P_T\, \mathrm{d}|Y|$. The P_T and $|Y|$ refer to the W boson distributions,
- The summation runs over all 21 bins of the $(P_T(W), |Y(W)|)$ phase-space.

The prime in the notation above indicates that the phase space used in the above correction factors is the one that is selected by our reconstruction-level cuts, with no acceptance effects applied, and is not the same as in Section 7.4.1. This can be seen more clearly from Figure 7.7, which shows the $(P_T, |Y|)$ phase-space of the W bosons at the generator level which survive a reconstruction level $P_T(W) > 50$ GeV cut. Whilst the same $P_T(W)$ and $|Y(W)|$ binning is used as in Section 7.4.1, the number of W bosons and the $f_{L,R,0}$ values in each bin are recalculated, and are in general different.

The results of carrying out this procedure at the reconstruction level using the selection criteria as defined in Section 7.2.2 are shown in Figure 7.8, where the corresponding templates for both muon charges are shown. The templates also include the contributions from $\tau \to \mu$ decays. Events stemming from such decays are predominantly valued at LP$= 0$, since the extra decay means that in general, the lepton is no longer well aligned with the W boson.

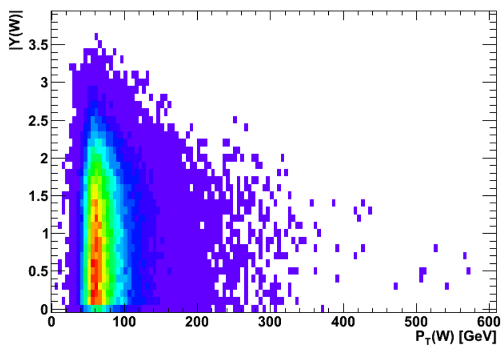

(a) Generator level $|Y(W)|$ versus $P_T(W)$ distribution.

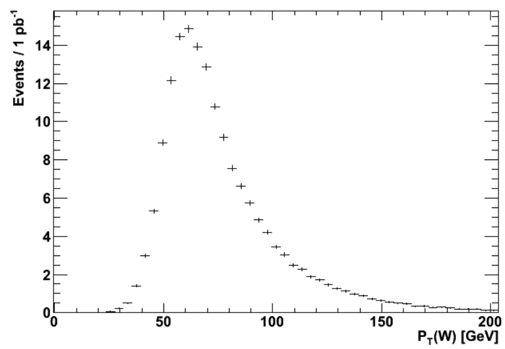

(b) Generator level $P_T(W)$ distribution.

Figure 7.7: The generator level $|Y(W)|$ vs. $P_T(W)$ (a) and $P_T(W)$ (b) distributions for those events surviving a reconstruction level $P_T(W) > 50$ GeV cut.

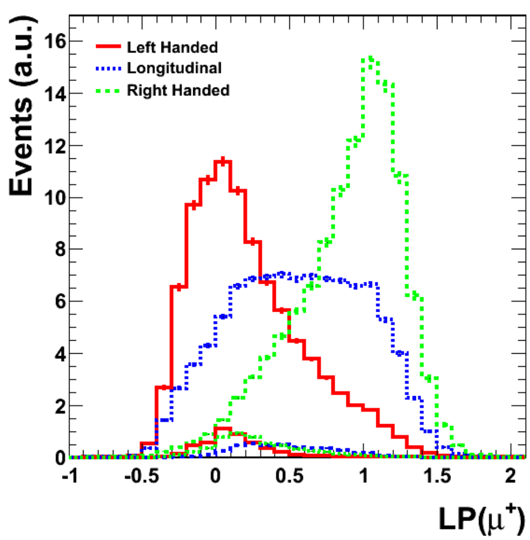

(a) The LP(μ^+) templates at the reconstruction level

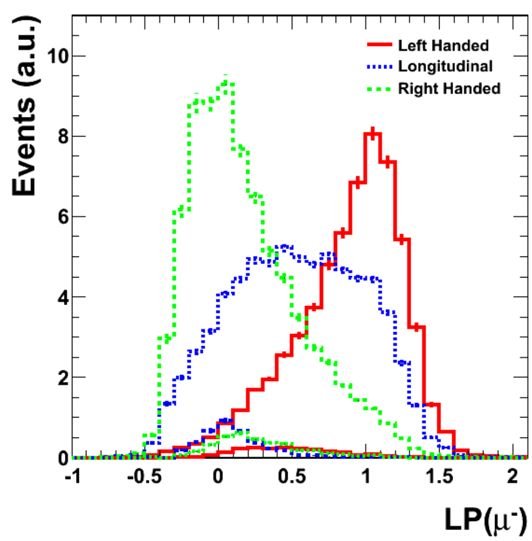

(b) The LP(μ^-) templates at the reconstruction level

Figure 7.8: The LP template shapes at the reconstruction level, with the selection criteria of Section 7.2.2, shown for both the positive (a), and negative (b) muon charges. Also shown are the contribution from $\tau \to \mu$ decays.

7.5 Fitting procedure

7.5.1 Description

The measurement of the f_i parameters is performed using a maximum likelihood fit to the LP variable, separately for both muon charges. The RooFit [52] package is used, which is a dedicated tool used for modelling the expected distribution of events in a physics analysis, and is specialized to perform likelihood fits to data. The probability density function (PDF), $S(x)$, is constructed as a composite function involving three terms which are used to describe the three event hypotheses of the $W^{\pm}$ helicity (left-handed, right-handed and longitudinal):

$$S(x) = f_L \cdot h_L(x) + f_R \cdot h_R(x) + (1 - f_L - f_R) \cdot h_0(x) \tag{7.3}$$

where the coefficients f_L and f_R represent the corresponding fraction of left-handed and right-handed helicity states. Using the natural constraint that the helicity fractions must sum up to one, the longitudinal coefficient is expressed as $f_0 = 1.0 - f_L - f_R$, reducing the number of degrees of freedom of the fit to two. The helicity state functions $h_L(x)$, $h_R(x)$ and $h_0(x)$ are the three template histograms as shown in Figure 7.8.

The range of allowed values for the fractional parameters (f_L, f_R) is by definition the range [0, 1]. However, without an additional constraint, the possibility for scenarios where the sum of the coefficients exceeds one is not excluded, e.g. when $f_L = f_R = 0.6$. In such cases f_0 will be negative, and as this is an unphysical solution, the likelihood function is further constrained by the inequality $(f_L + f_R) \leq 1$.

The template fit to data is performed via a log-likelihood fit. The values of f_L and f_R are found via minimising:

$$-\log(L(\vec{f})) = -\sum_{D} \log(S(\vec{x}_i; \vec{f})) \tag{7.4}$$

where the likelihood function $L(\vec{f}) = \prod_{D} S(\vec{x}_i; \vec{f})$ i.e. is the product of probabilities given by $S(x)$ for all data points in the dataset $D(x)$ where $x =$ the LP variable.

7.5.2 Acceptance Correction Factor

By definition, the number of events contributing to the three generator-level templates of Figure 7.5 are equivalent for each charge individually, by virtue of the reweighting applied. As discussed in Chapter 6, the charged lepton P_T spectra are markedly different between the charges, representing the predominant left-handed polarisation of the W bosons ($f_L \approx 60\%$), and hence are affected differently by the detector acceptance and selection criteria (essentially $P_T(\mu) > 10$ GeV and $|\eta(\mu)| < 2.1$). These effects are exaggerated when considering 100% left-handed, right-handed and longitudinal polarisations of the W bosons individually for each charge. At the reconstruction level therefore, the number of events contributing to the three templates for a particular charge are not the same. If the h_L, h_R and h_0 functions as defined in Equation 7.3 are individually normalised to one, the information on the relative normalisations of these templates must therefore be taken into account separately in the final fit result, by way of an acceptance correction factor. This correction factor is therefore applied after the fitting procedure, and has no effect on either the shape of the templates or the quality of the fit. It takes the form:

$$C^{\pm}_{L,R,0} = \frac{\int\int W'^{\pm}(P_T,|Y|) f'^{\pm}_{L,R,0}(P_T,|Y|)\ \mathrm{CMS}^{\pm}(P_T,|Y|)\ \mathrm{d}P_T\ \mathrm{d}|Y|}{\int\int W'^{\pm}(P_T,|Y|) f'^{\pm}_{L,R,0}(P_T,|Y|)\ \mathrm{d}P_T\ \mathrm{d}|Y|} \tag{7.5}$$

where:

- The P_T and $|Y|$ refer to the W boson distributions,
- The function $\mathrm{CMS}^{\pm}(P_T(W), |Y(W)|)$ represents the behaviour of the CMS detector. This is currently taken from simulation, and encodes the expected detector response, as well as the trigger and reconstruction algorithms.

This means that the numerator in Equation 7.5 is the integral of the respective template at the reconstruction level with the full selection criteria applied (see Section 7.2.2), and the denominator is the integral of the same template at the generator level, with only the reconstruction level $P_T(W)$ cut applied. Both integrals are over the LP range used in the maximum likelihood fit.

In this analysis, both the shapes and relative normalisations of the respective templates for both charges are taken from the MC. As is shown in Section 7.5.3, the effect of such an acceptance correction is around 10%. The error on the CMS function is also estimated to be about 10%, and so overall the uncertainty on this correction is $\mathcal{O}(1\%)$.

7.5.3 Closure Test

In order to validate the procedure presented so far, in the absence of a background hypothesis, a closure test is performed individually for both charges. The first test is at the generator-level, and involves the reconstruction-level $P_T(W) > 50$ GeV cut. This results in the $(P_T(W), |Y(W)|)$ phase space as shown in Figure 7.7(a). The $\cos(\theta^*)$ distribution for all events which survive this cut is plotted, and the resulting distributions for both charges independently are fitted according to Equations 2.7 and 2.8. These fit results are summarised in Table 7.2 below and are used as the baseline values.

Generator level templates of the LP variable for both charges in this same phase space are generated according to the factors in Section 7.4 and fitted to the corresponding LP distribution using a maximum likelihood fit. For the purpose of the closure test, the central value of the fit is extracted using all the events in the W+Jets MC sample, corresponding to an integrated luminosity of approximately 400pb^{-1}. The results of this procedure are also shown in Table 7.2 and can be compared directly to the analytical fit results where there is very good agreement, as expected. This demonstrates that the reweighting procedure generates the correct templates of the LP variable.

Going to the reconstruction-level and applying the full selection requirements of Section 7.2.2, the templates of Figure 7.8 are similarly fitted. The fit to this pseudo-data is shown in Figure 7.9 for both muon charges, where again, the error bars correspond to the total number of events in the W+Jets MC sample. The fit results are shown both before and after the acceptance correction of Equation 7.5, in columns (c) and (d) of Table 7.2 respectively. The original values are recovered to within the statistical uncertainty of the Monte Carlo sample.

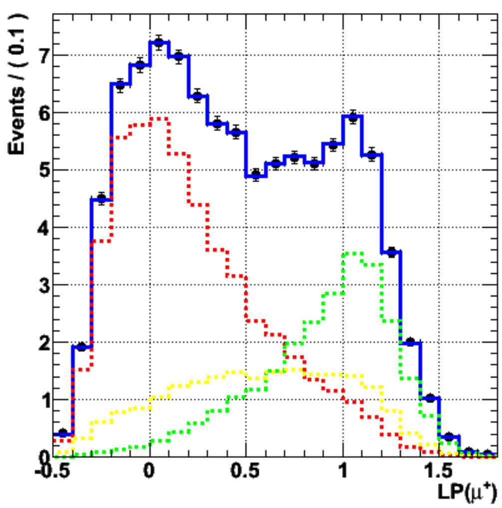

(a) The LP(μ^+) fit at reconstruction-level

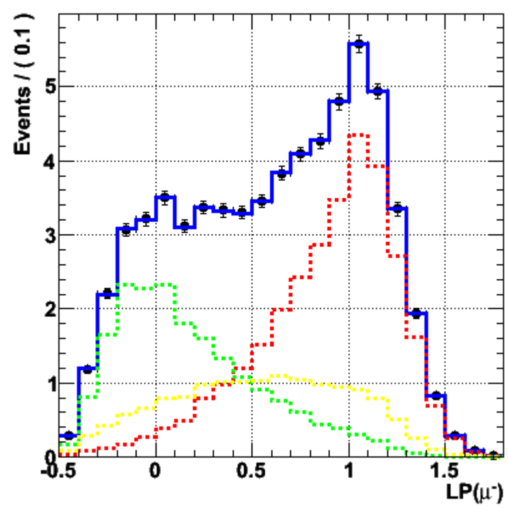

(b) The LP(μ^-) fit at reconstruction-level

Figure 7.9: The LP fit result (blue line) at the reconstruction level, with the selection criteria of Section 7.2.2 and the templates of Figure 7.8, shown for both the positive (a), and negative (b) muon charges. The pseudo-data (black points) error bars correspond to an integrated luminosity of 400pb^{-1}, whilst the histograms are scaled to arbitrary units. The left-handed (red), right-handed (green) and longitudinal (yellow) templates are also shown.

Table 7.2: A closure test of the methods described in Section 7.4. The errors on the analytical fit results (a) stem from the number of events in the Monte Carlo sample, which is equivalent to 400pb^{-1} of integrated luminosity. Step 1 (b) shows the central value for the template fit at generator level. Step 2 (c) shows the central value for the template fit at reconstruction level without acceptance corrections applied. Step 3 (d) shows the same value as (c), but with acceptance corrections applied.

	(a) Baseline	(b) Step 1	(c) Step 2	(d) Step 3
f_L^-	0.5214 ± 0.0040	0.5212	0.4747	0.5206
f_R^-	0.2707 ± 0.0034	0.2647	0.3010	0.2676
f_L^+	0.5543 ± 0.0032	0.5506	0.5239	0.5607
f_R^+	0.2270 ± 0.0026	0.2239	0.2640	0.2314

7.5.4 Background Templates

When considering the detector level information from those events which survive the selection criteria, the templates defined thus far are not the whole story. As can be seen from Table 7.1, a non-zero contribution from several other SM processes i.e. backgrounds, exist. In order to incorporate the effects of such background events, an additional component is added to the PDF, i.e. a background template. The generation of such background templates is less involved than the procedure as defined in Section 7.4. The background template shapes are simply those from the resulting LP distribution at the reconstruction-level for the relevant SM processes, and are shown both before and after the $M_T > 30$ GeV cut in Figures 7.10(a) and 7.10(b) respectively for the positive muon charge. The contribution from QCD events is greatly reduced following the M_T cut, which also changes the shape of the Z+Jets contribution, cutting out most events where LP = 0.

Correspondingly, the fit function is rewritten as a composite model, to include a signal ($S(x)$) and a background ($B(x)$) component:

$$g(x) = f_{sig} \cdot S(x) + (1 - f_{sig}) \cdot B(x) \tag{7.6}$$

The likelihood function is then written as the product of probabilities given by $g(x)$ for all data points in the dataset D, i.e. $L(\vec{f}) = \prod_D g(\vec{x}_i; \vec{f})$.

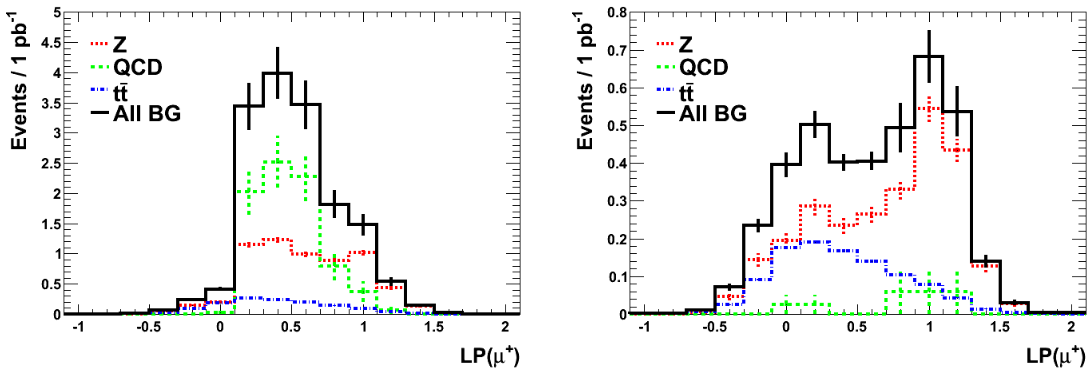

(a) The LP(μ^+) background shapes before the $M_T > 30$ GeV cut at reconstruction-level

(b) The LP(μ^+) background shapes after the $M_T > 30$ GeV at reconstruction-level

Figure 7.10: The LP(μ^+) background shapes shown before (a) and after (b) the application of the $M_T > 30$ GeV cut. The yield is normalised to an integrated luminosity of 1pb^{-1}.

Figures 7.11(a) and 7.11(b) show an example of the likelihood fits to the LP(μ^+) and LP(μ^-) distributions respectively, with the presence of a background component. The error bars on the pseudo-data have been scaled to an integrated luminosity of 10pb^{-1}. The fit result is represented by the blue curve, and the individual templates are shown superimposed in red (left-handed), green (right-handed) and black (longitudinal), along with the background template, shown as the yellow shaded area. The central values of the fit for $(f_L, f_R)^{\pm}$ are $(0.561, 0.232)^+$ and $(0.521, 0.268)^-$, and are consistent with the values from Table 7.2.

7.5.5 Fit Performance

In order to investigate the fitting performance, the one and two sigma contours of the likelihood fit for the parameters f_L and f_R are plotted in Figure 7.12 for both muon charges, where the error bars on the pseudo-data are still scaled to an integrated luminosity of 10pb^{-1}. The solid blue line represents the contour which connects all points where the function $g(x)$ of Equation 7.6 takes on its minimum value plus one standard deviation. The dashed blue line represents the same quantity, except for two standard deviations. By virtue of the elliptical contour shapes, the results

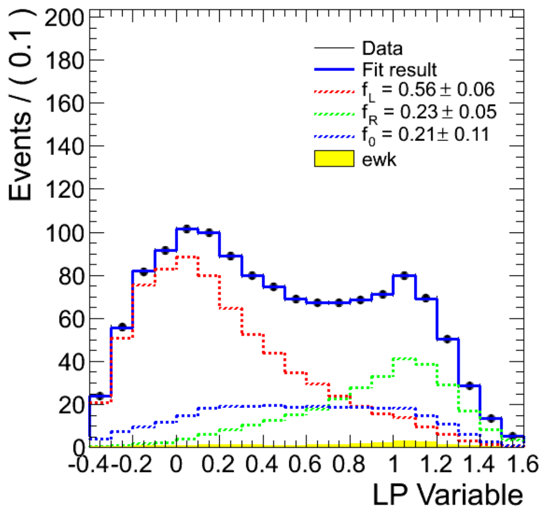

(a) The LP(μ^+) template fit at reconstruction-level

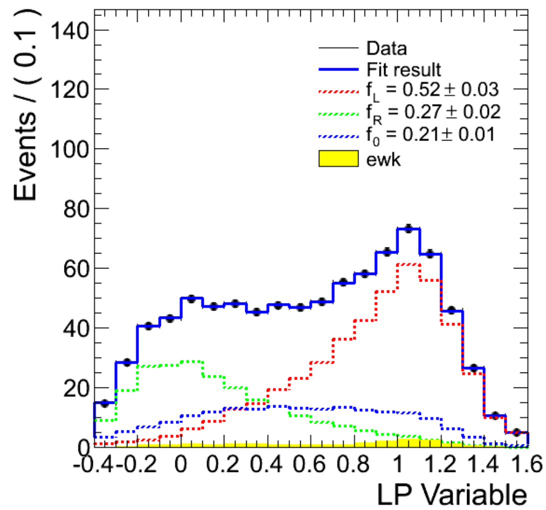

(b) The LP(μ^-) template fit at reconstruction-level

Figure 7.11: The LP distribution template fit at reconstruction level shown for positively charged (a) and negatively charged (b) muons. The error bars on the pseudo-data are rescaled to an integrated luminosity of 10pb^{-1}.

are quite linear in (f_L, f_R) space, at least for the positively charged muon. Given the relatively fewer negatively charged muons, the corresponding contours exhibit a slight asymmetric behaviour, which is remedied when considering a larger dataset, e.g. 100pb^{-1} (not shown).

An alternative combination of the helicity parameters can be constructed, namely to be directly correlated to the A_0 and A_4 coefficients. Figures 7.13(a) (μ^+) and 7.13(b) (μ^-), show the corresponding one and two sigma contours in the $((f_L+f_R),(f_L-f_R))$ space, i.e. (A_0, A_4) space. The fit is also symmetric in this case, however the correlations are greatly reduced between these two measurements.

In order to test the fit stability, toy datasets of the LP distribution are generated n times, and sampled according to the model PDF of Equation 7.6. The pull distributions for f_L and f_R (and f_0) are then calculated, according to the quantity:

$$\frac{(f^{\mathrm{nom}} - f^{\mathrm{meas}})}{\delta f^{\mathrm{meas}}} \tag{7.7}$$

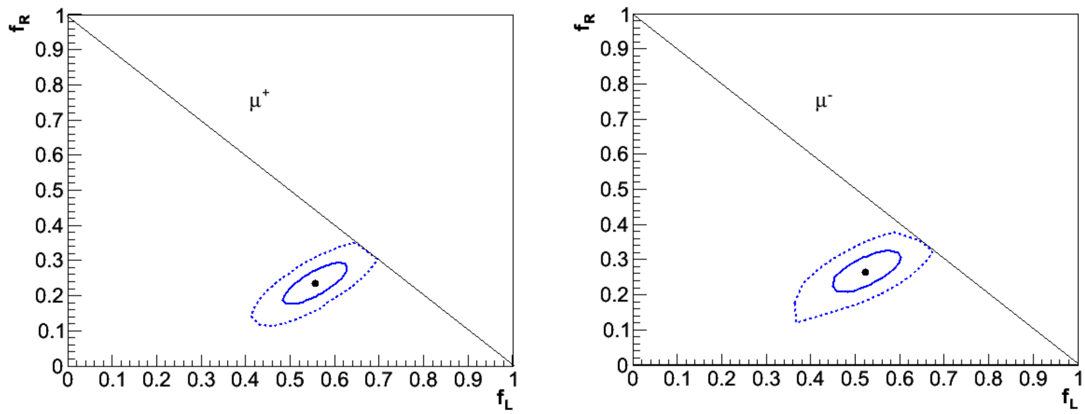

(a) The one and two sigma contours for the LP(μ^+) template fit at reconstruction-level

(b) The one and two sigma contours for the LP(μ^-) template fit at reconstruction-level

Figure 7.12: The one and two sigma contours for the LP distribution template fit at reconstruction level shown for positively charged (a) and negatively charged (b) muons in (f_L, f_R) space. The error bars on the pseudo-data are rescaled to an integrated luminosity of 10pb^{-1}, and the diagonal line represents the limit of the constraint $(f_L + f_R) \leq 1.0$.

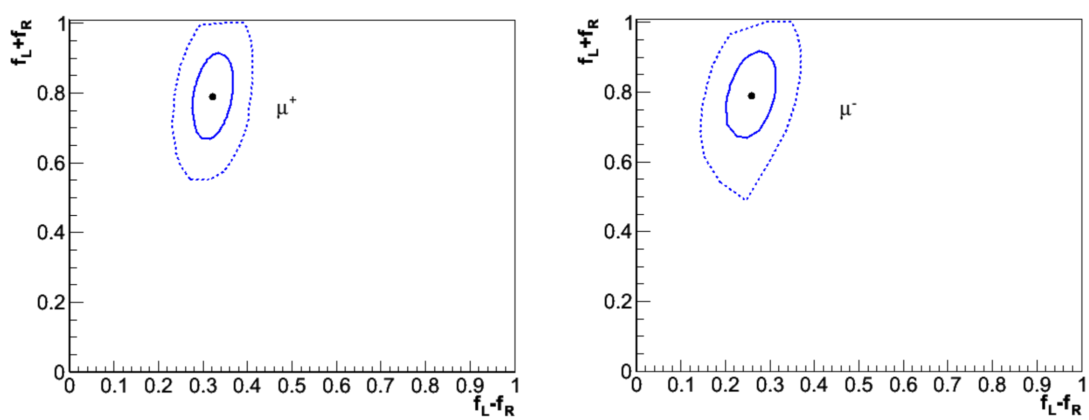

(a) The one and two sigma contours for the LP(μ^+) template fit at reconstruction-level

(b) The one and two sigma contours for the LP(μ^-) template fit at reconstruction-level

Figure 7.13: The one and two sigma contours for the LP distribution template fit at reconstruction level shown for positively charged (a) and negatively charged (b) muons in $((f_L + f_R), (f_L - f_R))$ space. The error bars on the pseudo-data are rescaled to an integrated luminosity of 10pb^{-1}.

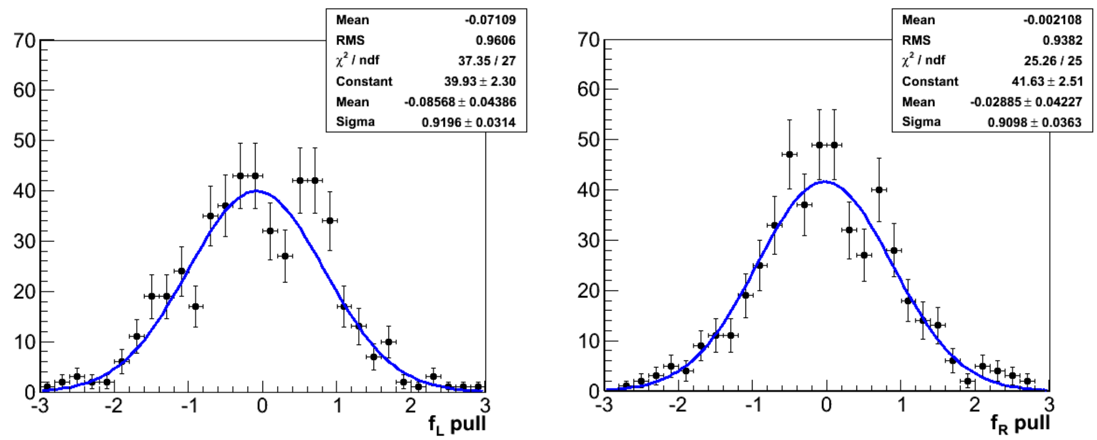

(a) The f_L pull distribution

(b) The f_R pull distribution

Figure 7.14: The pull distributions of the f_L (a) and f_R (b) parameters for positively charged muons, generated with a toy MC of 500 pseudo-experiments and at an integrated luminosity of 100pb^{-1}.

where f^{nom} is the nominal value of the fit parameter as shown in column (a) of Table 7.2, f^{meas} is the measured value from the fit and δf^{meas} is the error returned by each pseudo-experiment of the toy MC. This procedure was performed for 500 toy-experiments each and at an integrated luminosity of 100pb^{-1}, the results of which are shown for positively charged muons in Figures 7.14 and 7.15. For a properly functioning fit, the pull distribution of all the fit parameters must be consistent with a Gaussian of mean zero and sigma one. A possible bias on the fractional helicity parameters due to the fit model is found to be compatible with zero, establishing the reliability of the fitting procedure.

7.6 Systematic Uncertainties

The following systematic uncertainties have been considered:

- Background estimate. This includes both the shape of the background included in the fit as well as the uncertainty on the estimate of the expected number of events from background processes. To estimate this systematic

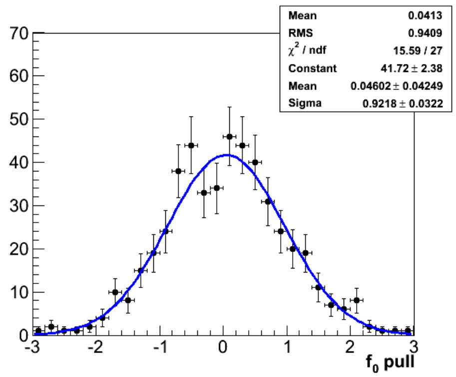

Figure 7.15: The pull distribution of the f_0 parameter for positively charged muons, generated with a toy MC of 500 pseudo-experiments and at an integrated luminosity of 100pb^{-1}.

uncertainty, the fit is repeated with the background estimate increased (decreased) by three times the uncertainty on the central estimate. This yields an uncertainty on $(f_L - f_R)^{\pm} < 4.1\%$ and $f_0^{\pm} < 4.6\%$. The uncertainty in the shape of the shape is estimated repeating the fit 100 times using a template which is generated from the input background template, with each bin fluctuating freely within Poisson statistics. In the muon channel, this yields an overall uncertainty on $(f_L - f_R)^{\pm} < 8.0\%$ and $f_0 < 6\%$.

- Charge misidentification. Any mismeasurement of the muon charge results in a cross-contamination of the W^+ and W^- samples. To gauge the rate at which such misidentifications occur, a MC study was performed using the generator level information. For the $P_T(\mu)$ spectra considered, this rate was determined to be $\mathcal{O}(10^{-5})$, and hence for muons is a negligible effect.

- A_i dependencies. As discussed in Sections 7.3 and 6.3.4, a measurement of the A_0 and A_4 parameters using the LP variable will depend on the other A_i coefficients. The effects of increasing each A_i coefficient individually by 10% (of its value) on the fit values of f_0 and $(f_L - f_R)$ are shown in Table 7.3. As expected, the effect of increasing A_0 and A_4 is most prominent in the values of f_0 and $(f_L - f_R)$ respectively. For a measurement of $(f_L - f_R)$, the response to A_4 is about an order of magnitude larger than the other A_i parameters. For a measurement of f_0, the response to A_1 and A_2 is of a similar magnitude but in the opposite direction to the response from the A_0 parameter, as discussed in

Section 6.3.4. The correlation between the A_0 and A_4 measurements i.e. the fluctuation in $(f_L - f_R)$ given a change in A_0 and vice-versa, is small, as also indicated from Figure 7.13.

- Energy Scale uncertainty. Since the transverse momentum of the W boson is deduced from the E_T^{miss} of the event, any uncertainty on the resolution of this E_T^{miss} corresponds to different values for the W helicity components. In the muon channel, the uncertainty is dominated by the hadronic activity in the event, and so the resolution of $\vec{P}_T(W) = \vec{E}_T^{\text{miss}} + \vec{P}_T(\mu)$ is smeared on an event-by-event basis with a Gaussian ($\sigma = 5\% \times$ value). The results are shown in Table 7.3, where the effect is $< 2.5\%$ for a measurement of $(f_L - f_R)^{\pm}$, and $< 4\%$ for a measurement of $f_0^{\pm}$.

- Contamination from Z boson decays. Partially reconstructed Z boson decays (when one of the leptons is either outside the detector acceptance or is not reconstructed) along with mismeasured Z boson decays (where one of the leptons is not measured properly) result in events mimicking the W boson decay signature. It is estimated that 5.0 events pass the selection criteria for this analysis per inverse picobarn of integrated luminosity. To estimate the systematic uncertainty, an additional component for this Z boson contamination is included in the fit. The uncertainties on both the measurements of f_0 and $(f_L - f_R)$ from excluding the Z boson contribution from the background fit are shown in Table 7.3.

- $t - \bar{t}$ contamination. Using Monte Carlo simulation and a Next-to-Leading Order cross section for the production of $t\bar{t}$ pairs of 157.5 pb, it is estimated that 3.6 events pass the selection criteria for this analysis per inverse picobarn of integrated luminosity. The effects of including this background into the templated fit without a corresponding background template are shown in Table 7.3.

Table 7.3: The relative effects on the values of f_0 and $(f_L - f_R)$ by varying the quantity indicated by the amount indicated. The selection requirements as defined in Section 7.2.2 are used.

	$(f_L - f_R)^-$	f_0^-	$(f_L - f_R)^+$	f_0^+
Baseline Value	0.253	0.212	0.329	0.208
$A_0 + (A_0 \times 10\%)$	-0.4%	+9.9%	-0.9%	+11.5%
$A_1 + (A_1 \times 10\%)$	+0.4%	-5.2%	+0.3%	-5.8%
$A_2 + (A_2 \times 10\%)$	+0.8%	-3.8%	-0.3%	-4.3%
$A_3 + (A_3 \times 10\%)$	-0.4%	0.0%	0.0%	0.0%
$A_4 + (A_4 \times 10\%)$	+7.1%	-1.9%	+6.7%	-2.4%
Exclude Z	+4.0%	-4.7%	-4.9%	-1.4%
Exclude $t\bar{t}$	$<$0.5%	$<$0.5%	$<$0.5%	$<$0.5%
Exclude QCD	$<$0.1%	$<$0.1%	$<$0.1%	$<$0.1%
Smear $P_T^{\mathrm{RECO}}(W)$ by 5%	-2.4%	+3.3%	+1.2%	+3.8%

Chapter 8

First Look at LHC Data

8.1 Introduction

The data presented in this chapter were collected between March and September 2010, and correspond to approximately 3.2 pb^{-1} of collision data at a proton-proton centre of mass energy of $\sqrt{s} = 7$ TeV. The criteria used for event selection are as described in Section 7.2.2. In total 731 events pass such a selection, in very good agreement with the yields presented in Table 7.1. Of these, 299 events contain a negatively charged muon, whilst 432 are with a positively charged muon. This leads to a charge ratio of 0.692, slightly larger than the expectations from Figure 2.3(b), as expected given the $P_T(W) > 50$ GeV range considered (see Section 6.1).

Overlaid data and MC distributions for the LP variable and underlying quantities are shown in Section 8.2, separately for events from both positively and negatively charged muons, and the respective template fit results are shown in Section 8.3.

8.2 Data vs MC

For the following data and MC distributions, the MC is normalised to the integrated luminosity using the cross sections from Table 7.1, as opposed to the number of data events. The uncertainty on the value of the integrated luminosity (11%) is

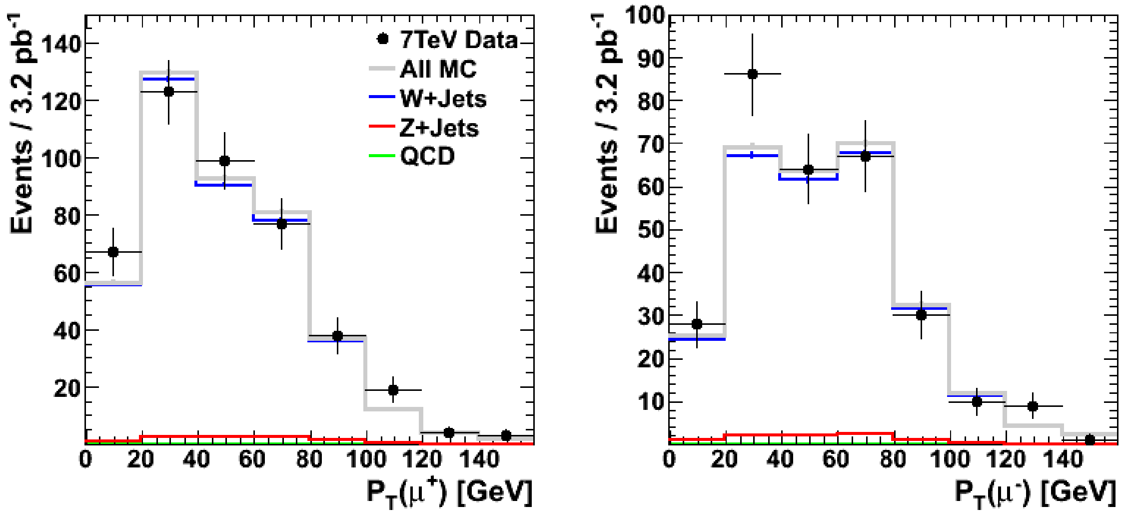

Figure 8.1: Overlaid data and MC distributions for the $P_T(\mu^+)$ distribution.

not taken into consideration. Overlaid data and MC distributions for the $P_T(\mu)$, $P_T(W)$ and M_T distributions are shown in Figures 8.1 to 8.3 respectively, whilst the LP distribution is shown in Figure 8.4. The individual contributions from each of the different MC samples are also shown. Overall, the data are described well by the MC for the $P_T(\mu)$, $P_T(W)$ and M_T distributions, and there is no significant difference in the comparisons for the different charges. The data-MC comparison for the LP distributions, which also encode the angular separation between the muon and W boson, are also described well, namely the features around LP values of 0 and 1.

8.3 Template Fit Results

An initial indication of polarisation effects may be seen from the average value of the LP(μ^+) distribution with respect to the LP(μ^-) distribution. From discussions in Chapters 6 and 7, it is expected that the average of the negatively charged distribution is larger, and it is found that the LP(μ^-) average is 0.56 (RMS = 0.49), whilst the LP(μ^+) average is 0.46 (RMS = 0.48), which is within expectations.

Using the templates and fitting procedure as described in Chapter 7, polarisation information from the 3.2 pb^{-1} of data as collected by the CMS experiment can be

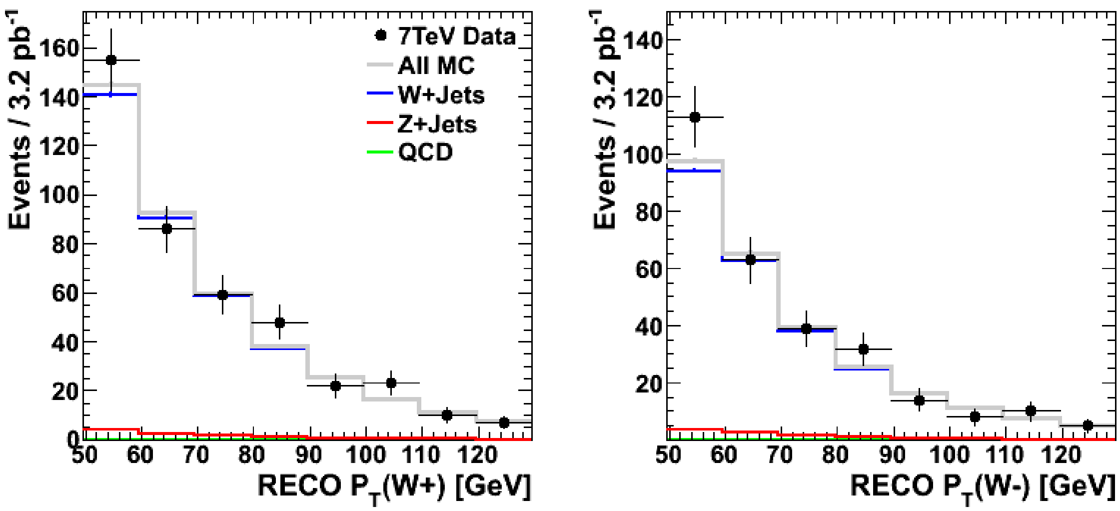

Figure 8.2: Overlaid data and MC distributions for the $P_T(W^+)$ distribution.

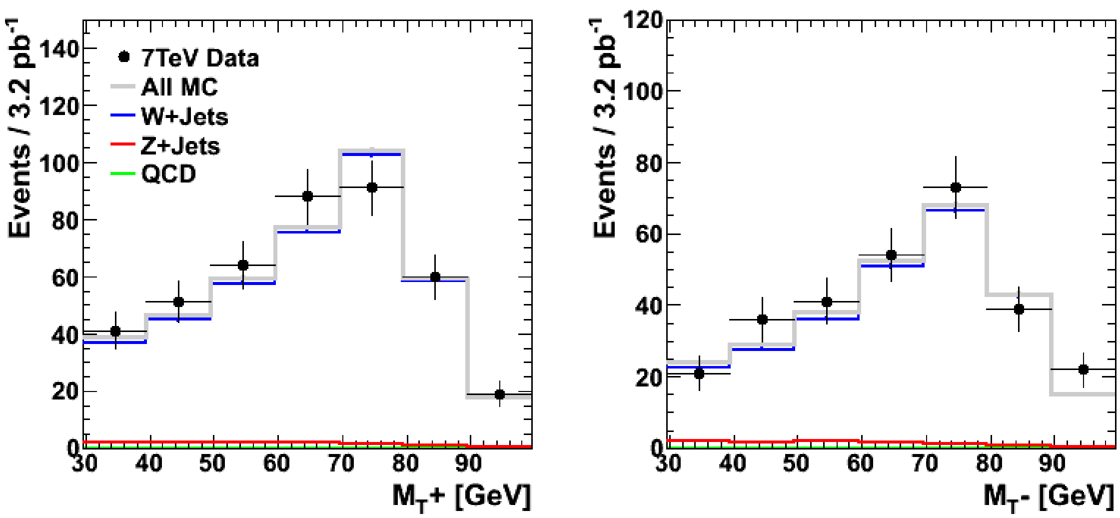

Figure 8.3: Overlaid data and MC distributions for the $M_T(\mu^+)$ distribution.

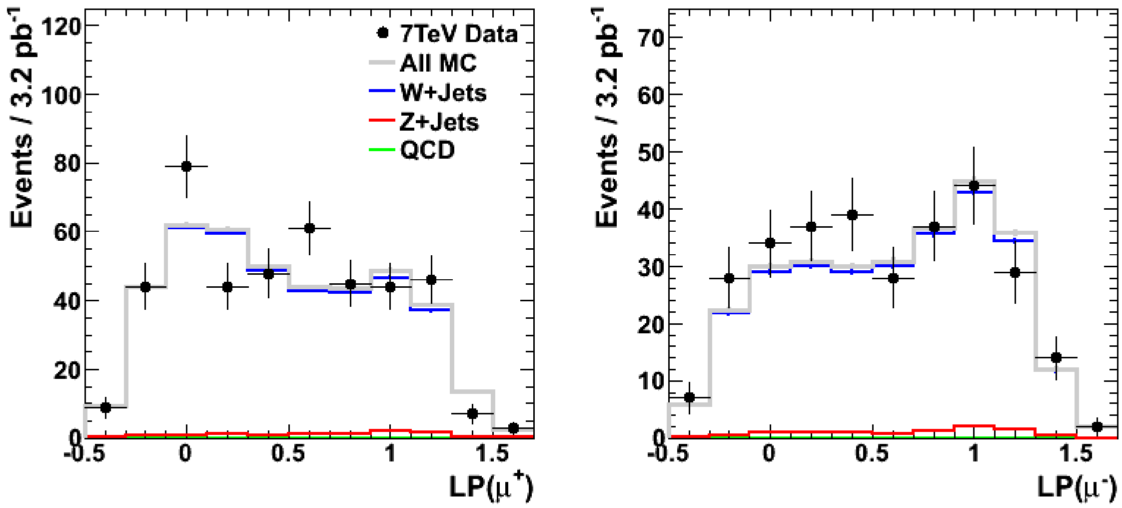

Figure 8.4: Overlaid data and MC distributions for the LP(μ^+) distribution.

extracted. The fit results are shown for positively and negatively charged muons in Figures 8.5(a) and 8.5(b) respectively. The results are summarised in Table 8.1. When compared to the results expected from Table 7.2, there is a good agreement within the statistical errors for the positive charge case, whilst the result for the negative charge case is within two standard-deviations of expectation. The respective contours from the fit to the data are shown in Figures 8.6(a) and 8.6(b) for positively and negatively charged muons respectively. The relative size of the contours is consistent with a scaling of $\frac{1}{\sqrt{N}}$ (with integrated luminosity), when compared to the 10 pb^{-1} contours from the MC study shown in Figure 7.13.

In conclusion, a look at the first data from the LHC with respect to a measurement of the W boson polarisation looks promising. The data agree well with expectations from MC, as well as the fit results corresponding to an integrated luminosity of 3.2 pb^{-1} with the MC templates. However, the errors quoted on measurements of the f_i components are purely statistical, and a more detailed systematic study will need to be carried out as part of a publication effort.

Table 8.1: A summary of the fit results as shown in Figures 8.5(a) and 8.5(b) for positively charged and negatively charged muons respectively. Also shown are the respective closure test values from Table 7.2 for reference.

	f_L	f_R	$(f_L - f_R)$	f_0
Data: LP(μ^+)	0.554 ± 0.106	0.206 ± 0.081	0.347 ± 0.070	0.240 ± 0.176
MC: ℓ^+ baseline	0.554	0.227	0.327	0.219
Data: LP(μ^-)	0.418 ± 0.121	0.321 ± 0.092	0.097 ± 0.088	0.262 ± 0.196
MC: ℓ^- baseline	0.521	0.271	0.251	0.208

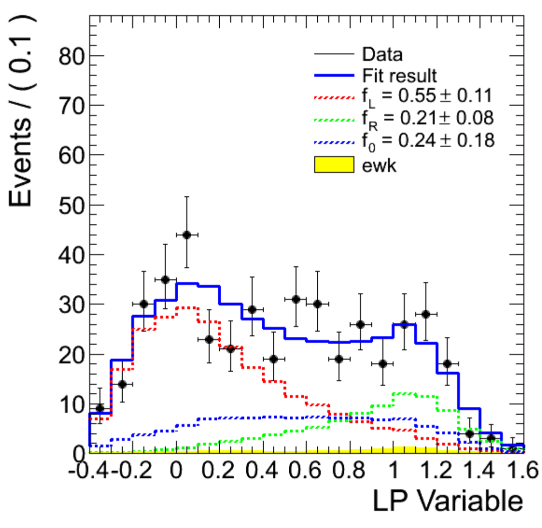

(a) Template fit results for the LP(μ^+) distribution

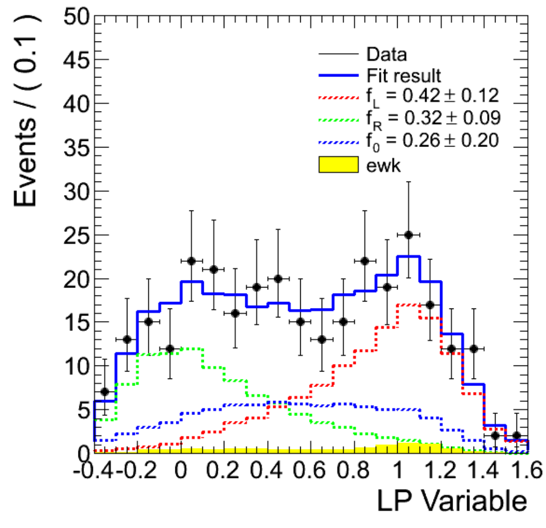

(b) Template fit results for the LP(μ^-) distribution

Figure 8.5: Template fit results for the LP(μ^+) (a) and LP(μ^-) (b) distributions using 3.2 pb^{-1} of collision data.

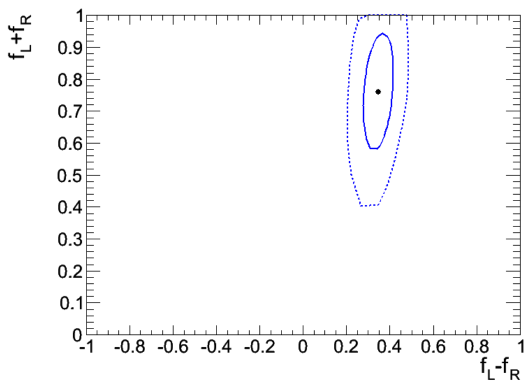

(a) The one-sigma (solid) and two-sigma (dashed) contours for the LP(μ^+) distribution template fit

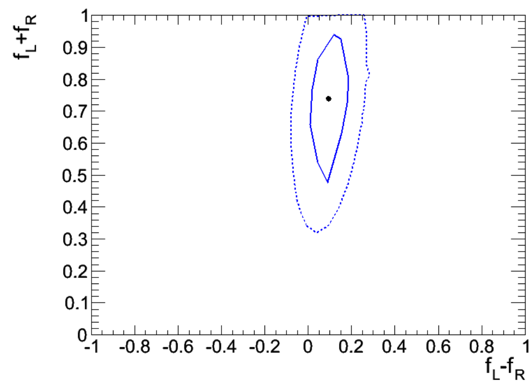

(b) The one-sigma (solid) and two-sigma (dashed) contours for the LP(μ^-) distribution template fit

Figure 8.6: Contours for the LP(μ^+) (a) and LP(μ^-) (b) template fits using 3.2 pb^{-1} of collision data.

Chapter 9

Summary and Conclusions

Global Calorimeter Trigger

The GCT commissioning strategy was discussed in detail in Chapter 4 of this thesis. A software suite was developed to allow the event-by-event comparison of the hardware with a bit-level software emulation. This was used in commissioning to achieve 100% agreement for all trigger quantities, and also culminated in a defined workflow for data quality monitoring of the GCT.

Missing Energy Triggers

Studies of the Level-1 energy sum triggers in Chapter 5 were performed using Monte Carlo generated samples of Standard Model and super-symmetric physics processes. The performance of jet-based (H_T and H_T^{miss}) and calorimeter-based (E_T and E_T^{miss}) total and missing energy sum quantities were compared, and the effects of jet energy corrections and jet threshold cuts were also studied. It was found that with no thresholds applied, both E_T and H_T, and E_T^{miss} and H_T^{miss} perform similarly. The application of a jet threshold was found to reduce the performance of the jet-based triggers, but strongly suppress detector noise. Jet energy corrections were found to improve the performance of the jet-based triggers for certain topologies. This led to the implementation and commissioning of the H_T^{miss} trigger in the GCT.

W boson polarisation

The production of W bosons in proton-proton collisions (e.g. at the LHC) displays new characteristics which are not present in proton-antiproton collisions (e.g. at the SPS and Tevatron colliders). Not only is there an asymmetry in the production rate of positive versus negative W bosons, but in addition, at high transverse momenta, the bosons are expected to display large transverse polarisation (predominantly left-handed). These effects were theoretically motivated in Chapter 2, and a leading order Monte Carlo generator was used to observe these effects in simulation in the helicity frame in Chapter 6, where two potential applications of these properties were also shown.

The final two chapters summarised the effort towards measuring the W boson polarisation in the muon channel, using templates of the Lepton Projection variable defined in Chapter 6. The template generation method and fitting procedure were discussed in detail, and tested in simulation, in Chapter 7. An analysis of the first 3.2 pb^{-1} of LHC data from the $\sqrt{s} = 7$ TeV dataset was then presented in Chapter 8, which showed very good agreement with expectations from Monte Carlo simulation studies. The results of the template fit to these data were $(f_L - f_R)^+ = 0.347 \pm 0.070$, $f_0^+ = 0.240 \pm 0.176$, and $(f_L - f_R)^- = 0.097 \pm 0.088$, $f_0^- = 0.262 \pm 0.196$ for positive and negative charges respectively. The errors quoted are statistical.

References

[1] "Nobel prize in physics 2004." http://nobelprize.org/nobel_prizes/physics/laureates/2004/public.html.

[2] L. J. Dixon *et al.*, "Next-to-Leading Order Jet Physics with BLACKHAT," *arXiv:0912.4927v1* (2009).

[3] "CMS Outreach Pages." http://cms.web.cern.ch/cms/Media/Images/Detector/DetectorDrawings/index.html.

[4] M. D. Negra, A. Herve, L. Foa, and D. Acosta, "CMS Physics TDR, Volume1: Detector Performance and Software, Technical Report v8.1," tech. rep., CERN, 2006. CERN-LHCC-2006-001.

[5] CMS Collaboration, "CMS TriDAS Project, Technical Design Report Volume I: The Trigger Systems," tech. rep., CERN, 2000.

[6] Alwall *et al.*, "MadGraph/MadEvent v4: The New Web Generation," *JHEP* **28** (2007).

[7] "Pythia 8.1." http://home.thep.lu.se/~torbjorn/Pythia.html.

[8] F. J. Hasert *et al.*, "Discovery of weak neutral currents," *Phys. Lett. B* **46** (1973).

[9] UA1 Collaboration, "Discovery of the W-Boson," *Phys. Lett. B* **122** (1983).

[10] UA1 Collaboration, "Discovery of the Z-Boson," *Phys. Lett. B* **126** (1983).

[11] P. Higgs, "Broken symmetries and the masses of gauge bosons," *Phys. Rev. Lett.* **13** (1964).

[12] G. S. Guralnik, C. R. Hagen, and T. Kibble, "Global conservations laws and massless particles," *Phys. Rev. Lett.* **13** (1964).

[13] "The LEP electroweak working group." `http://lepewwg.web.cern.ch/LEPEWWG/`.

[14] S. L. Glashow, J. Iliopoulos, and L. Maiani, "Weak interactions with lepton-hadron symmetry," *Phys. Rev. D* **2** (1970).

[15] J. E. Augustin *et al.*, "Discovery of a narrow resonance in e^+e^- annihilation," *Phys. Rev. Lett.* **33** (1974).

[16] J. J. Aubert *et al.*, "Experimental observation of a heavy particle J," *Phys. Rev. Lett.* **33** (1974).

[17] M. Kobayashi and T. Maskawa, "CP-Violation in the renormalizable theory of weak interaction," *Prog. Theory. Phys.* **49** (1973).

[18] M. L. Perl *et al.*, "Evidence for anomalous lepton production in e^+e^- annihilation," *Phys. Rev. Lett.* **35** (1975).

[19] L. M. Lederman *et al.*, "Observation of a di-muon resonance at 9.5 GeV in 400 GeV proton-nucleus collisions," *Phys. Rev. Lett.* **39** (1977).

[20] CDF Collaboration, "Observation of top quark production in $\bar{p}p$ collisions with the collider detector at fermilab," *Phys. Rev. Lett.* **74** (1995).

[21] ALEPH Collaboration, "A direct measurement of the invisible width of the z from single photon counting," *Phys. Lett. B* **313** (1993).

[22] LEP, SLC, and Tevatron experiments, "Precision electroweak measurements and constraints on the standard model," *CERN-PH-EP/2008-020* (2008).

[23] J. Goldstone, A. Salam, and S. Weinberg, "Broken symmetries," *Phys. Rev.* **127** (1962).

[24] F. Zwicky, "Die rotverschiebung von extragalaktischen nebeln," *Hel. Phys. Acta* **6** (1933).

[25] WMAP Collaboration, "Five-year Wilkinson Microwave Anisotropy Probe observations: Data processing, sky maps, and basic results," *The Astrophysical Journal Supplement* **180** (2009).

[26] Super Kamiokande Collaboration, "Evidence for oscillation of atmospheric neutrinos," *Phys. Rev. Lett.* **81** (1998).

[27] P. Adamson *et al.*, "Measurement of neutrino oscillations with the MINOS detectors in the NuMI beam," *Phys. Rev. Lett* **101** (2008).

[28] G. R. Farrar and P. Fayet, "Phenomenology of the production, decay, and detection of new hadronic states associated with supersymmetry," *Phys. Lett. B* **76** (1978).

[29] T. S. F. Halzen and M. Kamionkowski, "Signatures of dark matter in underground detectors," *Phys. Rev. D* **45** (1992).

[30] G. Altarelli and G. Parisi, "Asymptotic freedom in parton language," *Nuclear Physics B* **126** (1977).

[31] "Martin-Stirling-Thorne-Watt parton distribution functions." `http://projects.hepforge.org/mstwpdf/`.

[32] A. D. Martin, R. G. Roberts, W. J. Stirling, and R. S. Thorne, "Parton distributions and the LHC: W and Z production," *Eur. Phys. J. C* **14** (2000).

[33] C. Albajar *et al.*, "Studies of intermediate vector boson production and decay in UA1 at the CERN proton-antiproton collider," *Z. Phys. C* **44** (1989).

[34] L. J. Dixon, "Private communication," 2009.

[35] J. Collins and D. Soper, "Angular distribution of di-leptons in high-energy hadron collisions," *Phys. Rev. D* **16** (1977).

[36] E. Mirkes and J. Ohnemus, "W and Z polarization effects in hadronic collisions," *Phys. Rev. D* **50** (1994).

[37] K. Hagiwara, K. Hikasa, and N. Kai, "Parity-odd asymmetries in $W+$ jet events at hadron colliders," *Phys. Rev. Lett* **52** (1984).

[38] L. Evans and P. Bryant, "LHC machine," *JINST 3, S08001* (2008).

[39] G. Iles *et al.*, "Revised CMS global calorimeter trigger functionality and algorithms," in *12*$^{\text{th}}$ *Workshop on Electronics for LHC and Future Experiments, Valencia*. 2006.

[40] G. Iles *et al.*, "Performance and lessons of the CMS global calorimeter trigger," 2008.

[41] K. Gray and J. Marrouche, "Higgs boson production via the $qq \rightarrow qqH \rightarrow \tau\tau$ channel at the CMS," 2007.

[42] G. Landsberg, "Extension of GCT capabilities to include MHT," 23 November, 2007.

[43] CMS collaboration, "CMS Physics TDR, Volume2: Physics performance," tech. rep., CERN, 2006. CERN-LHCC-2006-021.

[44] J. E. Volder, "The cordic trigonometric computing technique," *IRE Trans. Electronic Computing* **EC-8** (1959).

[45] J. S. Walther, "A unified algorithm for elementary functions," in *Spring Joint computer conf.* 1971.

[46] F. Oljemark *et al.*, "Transverse energy calibration for L1 jets," tech. rep., CMS, 2006. CMS-IN 2006/040.

[47] J. Pumplin *et al.*, "New generation of parton distributions with uncertainties from global QCD analysis," *JHEP 0207:012* (2002).

[48] M. R. Whalley *et al.*, "The Les Houches Accord PDFs (LHAPDF) and LHAGLUE," *arXiv:hep-ph/0508110* (2007).

[49] L. J. Dixon *et al.*, "NLO QCD predictions for $W + 3$ -Jet distributions at hadron colliders," *arXiv:0907.1984v1* (2009).

[50] CMS Collaboration, "Performance of muon identification in pp collisions at $\sqrt{s} = 7$ TeV," tech. rep., CERN, 2010. CMS-PAS-MUO-10-002.

[51] CMS Collaboration, "Measurement of inclusive W and Z cross sections in pp collisions at $\sqrt{s} = 7$ TeV," tech. rep., CERN, 2010. CMS-PAS-EWK-10-002.

[52] "The RooFit toolkit for data modelling." `http://roofit.sourceforge.net`.